

University of Stuttgart
Germany

Photon correlations and collective phenomena with Rydberg superatoms

Von der Fakultät Mathematik und Physik der Universität Stuttgart
zur Erlangung der Würde eines Doktors der Naturwissenschaften
(Dr. rer. nat.) genehmigte Abhandlung.

Vorgelegt von

Kevin Kleinbeck
aus Stuttgart.

Hauptberichter

Prof. Dr. Hans Peter Büchler

Mitberichter

Prof. Dr. Jörg Main

Prüfungsvorsitz

Prof. Dr. Tilman Pfau

Tag der mündlichen Prüfung 10.10.2022

Institut für Theoretische Physik III
Universität Stuttgart

2022

Abstract

This thesis studies the interaction of light with atom-like emitters. A common problem lies within the weak interaction of single atoms with the light field, resulting in barely measurable effects. A well-established method to circumvent this is by confining light and emitters in an optical cavity or a waveguide. However, the confinement leads to additional effects that are not present in the free space setting. Here we follow a different route and study the interaction of light with Rydberg superatoms, which possess a strong coupling to the photons without the need for confinement.

A Rydberg superatom is a dense ensemble of ultra-cold atoms, excited to high principal quantum numbers. The atoms collectively interact with the light field, resulting in a strong coupling of the superatom to photons. These enhanced interactions further lead to a highly directed emission of the photons. At the same time, the Rydberg blockade prevents the ensemble from absorbing more than one photon, such that the mesoscopic superatom possesses an atom-like absorption behaviour.

The enhanced coupling of the superatom to the light field results in strong correlations between the emitted photons, and the formation of non-classical states of light. More specifically, we show in chapter 3 that the interaction of light with a single superatom creates well-located many-photon states, which we denote as bound states of light. These, in turn, result in a bunched photon

Abstract

signal, with measurable effects in the two- and three-photon correlation functions. Furthermore, the non-trivial photon correlations reveal that the interaction with the superatom scatters the light into multiple orthogonal modes. Therefore, in chapter 4, we study the occupation of different modes of light. Our analysis shows that scattering coherent, i.e., classical light on a superatom, subsequently yields light with non-classical number statistics for some of the temporal modes. Turning this effect into a practical application, we discuss that a single superatom can prepare non-classical states of light as resources for quantum metrological experiments.

In realistic systems, dephasing processes occur in the superatom and counteract the creation of correlated and non-classical states, as mentioned above. More precisely, superatoms are never just perfect two-level emitters. The intrinsic dipole-dipole interactions of the individual atoms and their respective thermal motion lead to additional coherent and incoherent processes that drive the superatom into non-radiating states. These dynamics have the potential to dephase the superatom into non-radiating states irreversibly. The superatoms remain excited under the dephasing but can no longer interact with the light due to the Rydberg Blockade. Therefore the superatom absorbed exactly one photon from the incoming light field before becoming irrelevant for the dynamics of the remaining photons. These intrinsic and collective dissipative effects of the superatom directly lead to an application as a photon subtractor, as we show in chapter 5. There we analyse the optimal parameters for photon subtraction and show that near perfect and deterministic subtraction is possible in specific regimes.

The coupling of the light field to the superatoms not only influences the photons but also results in interesting effects on the superatoms. The directed emission of the photons leads to an emergent infinite-range exchange interaction between the superatoms. This coupling modifies the collective response of a superatom chain to the light field. In particular, we show in chapter 6 that

the exchange interactions quickly compensate for any superradiant decay of the superatom chain and lead to an algebraic decay of the superatom chain for intermediate times, which eventually terminates in the uncorrelated decay of single superatoms.

While the focus of chapter 6 lies on the interactions between multiple superatoms, the dipole-dipole interactions of individual atoms **within** one superatom similarly influence the superatom-light coupling, as we discuss in chapter 7. Specifically, we investigate an experimental setting in which a coherent light pulse drives a single superatom into an excited state. The superatom's subsequent decay depends on the duration and strength of the coherent pulse, which indicates additional coherent processes within the superatom. We find that for an accurate description, it is sufficient to model the superatom with just four states: The first two states represent the superatom's ground state and the optically excited state, respectively, while the other two states capture coherent and incoherent processes, respectively. Additionally, we find similarities between the experimental results and the superatom chain (discussed in chapter 6), which we use to motivate the four-level model further.

Zusammenfassung

Diese Dissertation handelt von der Wechselwirkung zwischen Licht mit atomartigen Systemen. Einzelne Atome wechselwirken lediglich schwach mit Licht und haben entsprechend einen kaum messbaren Einfluss auf die Photonen. Dieses Problem kann mit räumlich begrenzten Systemen, wie optische Kavitäten oder Wellenleitern, umgangen werden. Allerdings führt die räumliche Begrenzung zu neuen Effekten, die bei freien Systemen nicht auftreten. Deshalb untersuchen wir hier die Wechselwirkung von Licht mit Rydberg-Superatomen, die eine starke Kopplung an das Lichtfeld haben, ohne dass eine räumliche Begrenzung nötig ist.

Rydberg-Superatome sind dichte Gase ultrakalter Atome, die zu Zuständen mit hoher Hauptquantenzahl angeregt werden. Die kollektive Wechselwirkung aller Atome mit den Photonen resultiert in einer starken Kopplung an das Lichtfeld. Als Konsequenz dieser verstärkten Wechselwirkung tritt auch eine gerichtete Emission der Photonen auf. Desweiteren kann jedes Superatom, aufgrund der Rydberg-Blockade, immer nur eine einzelne Anregung tragen, weswegen das Superatom in seinem Absorptionsverhalten einem einzelnen Atom ähnelt.

Aufgrund der verstärkten Wechselwirkung zeigen die an einem Superatom gestreuten Photonen starke Korrelationen und bilden Zustände mit einer nicht klassischen Teilchenzahl-Besetzung. Wir untersuchen die Korrelationen in

Zusammenfassung

Kapitel 3, in welchem wir zeigen, dass die Wechselwirkung von Licht mit dem Superatom stark lokalisierte Licht-Zustände erzeugt. Diese resultieren in messbare zwei- und drei-Photonen-Korrelationen, die die Anhäufung der Photonen zeigen. Solche Korrelationen sind nur möglich, wenn das Licht nach der Streuung mehrere unterschiedliche Photonenzustände besetzt. Deshalb untersuchen wir in Kapitel 4 die Teilchenzahl-Besetzung unterschiedlicher Lichtmoden nach der Streuung eines Lasers an einem Superatom. Wir zeigen dort, dass manche Zustände eine nicht klassische Besetzung aufweisen. Diese nicht klassischen Zustände eignen sich unter anderem als Ressource für weitere Experimente. Wir zeigen als Beispiel eine mögliche Anwendung in der Quanten-Metrologie.

Superatome unterliegen jedoch Prozessen, die der Licht-Superatom-Wechselwirkung entgegenstehen und die oben genannten Korrelationen oder die nicht klassischen Eigenschaften des Lichtes dämpfen. Genau genommen, können wir Superatome nicht nur als ein Zwei-Niveau-System beschreiben, da die intrinsische Dipol-Dipol-Wechselwirkung der Atome und deren thermischen Bewegung das Superatom in Zustände bringen, die nur noch schwach an das Lichtfeld koppeln. Gerade die inkohärenten Prozesse können das Superatom irreversibel in solche schwach gekoppelten Zustände bringen. Da das Superatom dabei angeregt bleibt, werden weiterhin neue Anregungen durch die Rydberg-Blockade unterdrückt. Das Superatom speichert somit genau eine Anregung, beziehungsweise entfernt ein Photon aus dem einlaufenden Lichtfeld. Superatome verhalten sich also wie Photonen-Subtrahierer, wie wir in Kapitel 5 zeigen. In diesem Kapitel bestimmen wir die optimalen Parameter für Photonen-Subtraktion und zeigen, dass nahezu deterministische Subtraktion mit Superatomen möglich ist.

Die gerichtete Wechselwirkung der Photonen mit Superatomen führt dazu, dass in einer eindimensionalen Superatom-Kette unendlich weit reichende Austauschwechselwirkungen zwischen den Superatomen auftreten. Die Austauschwechselwirkung modifiziert die kollektive Kopplung der Superatome an das

Lichtfeld und wir zeigen in Kapitel 6, dass die Superatom-Kette dadurch keinen reinen superradianten Zerfall aufweist. Stattdessen wird nur der initiale Zerfall von Superradianz dominiert, danach geht die Superatom-Kette in einen algebraischen Zerfall über, der schließlich mit dem unkorrelierten Zerfall der einzelnen Superatome endet. In diesem Kapitel zeigen wir, wie die Austauschwechselwirkung super- und subradiante Zustände koppelt, was genau zu dem beobachteten algebraischen Zerfallsverhalten führt.

Das Augenmerk von Kapitel 6 liegt auf der Austausch- beziehungsweise Dipol-Dipol-Wechselwirkung zwischen den Superatomen. Solche Wechselwirkungen treten in schwächerer Form auch im Inneren eines einzelnen Superatoms zwischen seinen jeweiligen Atomen auf. Diese Wechselwirkungen haben Einfluss auf die Kopplung des Superatoms an das Lichtfeld, welche wir in Kapitel 7 genauer untersuchen. Dazu betrachten wir ein einzelnes Superatom, welches durch Stimulation mit einem Laser in einem angeregten Zustand präpariert wurde. Der anschließende Zerfall des Superatoms hängt von der Dauer und der Intensität des Laserlichts ab, was wir auf kohärente Prozesse im Superatom zurückführen können. Wir zeigen, dass für eine genaue Beschreibung des Superatoms vier Zustände nötig sind: einen Grundzustand und einen Anregungszustand, der durch Wechselwirkung mit dem Licht erreicht werden kann, sowie zwei, nicht direkt an das Lichtfeld gekoppelte, Zustände, die respektive kohärent und inkohärent an den ersten Anregungszustand koppeln. Dieses einfache Modell können wir direkt mit der Dynamik der Superatom-Kette aus Kapitel 6 erklären, da diese viele strukturelle Ähnlichkeiten mit der intrinsischen Dynamik eines einzelnen Superatoms aufweist.

Publications

This thesis is based on the following publications:

- *Observation of Three-Body Correlations for Photons Coupled to a Rydberg Superatom*
Nina Stiesdal, Jan Kumlin, **Kevin Kleinbeck**, Philipp Lunt, Christoph Braun, Asaf Paris-Mandoki, Christoph Tresp, Hans Peter Büchler, and Sebastian Hofferberth
Physical Review Letters **121**, 103601 (2018)
DOI: 10.1103/PhysRevLett.121.103601, arXiv: 1806.00062
- *Nonexponential decay of a collective excitation in an atomic ensemble coupled to a one-dimensional waveguide*
Jan Kumlin, **Kevin Kleinbeck**, Nina Stiesdal, Hannes Busche, Sebastian Hofferberth, and Hans Peter Büchler
Physical Review A **102**, 063703 (2020)
DOI: 10.1103/PhysRevA.102.063703, arXiv: 2006.14977v2
- *Observation of collective decay dynamics of a single Rydberg superatom*
Nina Stiesdal, Hannes Busche, Jan Kumlin, **Kevin Kleinbeck**, Hans Peter Büchler, and Sebastian Hofferberth
Physical Review Research **2**, 043339 (2020)
DOI: 10.1103/PhysRevResearch.2.043339, arXiv: 2005.05089

Publications

- *Controlled multi-photon subtraction with cascaded Rydberg superatoms as single-photon absorbers*

Nina Stiesdal, Hannes Busche, **Kevin Kleinbeck**, Jan Kumlin, Mikkel G. Hansen, Hans Peter Büchler, and Sebastian Hofferberth

Nature Communications **12**, 4328 (2021)

DOI: 10.1038/s41467-021-24522-w, arXiv: 2103.15738

Additionally, chapter 4 consists of yet unpublished work.

Contents

Abstract

i

Zusammenfassung

v

Publications

ix

1 Rydberg superatoms

1

- 1.1 *Rydberg Blockade* / 2
- 1.2 *Two-photon transitions* / 4
- 1.3 *Interaction of light with a Rydberg gas* / 6
 - 1.3.1 *Theoretical description* / 7
 - 1.3.2 *Internal dynamics of the superatom* / 13
 - 1.3.3 *Emission from an excited superatom* / 17
 - 1.3.4 *Comparison to the literature* / 18
 - 1.3.5 *Effective superatom model* / 21
- 1.4 *Experimental Realisation* / 23
 - 1.A *Exact treatment of the energy phase* / 25

2 Theoretical description of superatom scattering

29

- 2.1 *Bethe Ansatz solutions* / 31
 - 2.1.1 *Chiral quantum optical Hamiltonian* / 31
 - 2.1.2 *Bethe state solutions* / 33
 - 2.1.3 *Eigenmode decomposition and Green's function* / 35
- 2.2 *Quantum optical master equation* / 37
 - 2.2.1 *Derivation* / 37
 - 2.2.2 *Input-Output relations and photonic correlation functions* / 42
- 2.3 *Mode population in the SLH formalism* / 43

3 Photon correlations by superatom interaction

47

- 3.1 *Predictions from the Bethe states* / 48
 - 3.1.1 *Few Photon scattering solutions* / 48
 - 3.1.2 *Two- and three-photon correlations* / 50
- 3.2 *Master equation solutions and experimental results* / 54

4 Photon number statistics in binned modes

57

- 4.1 *Photon number statistics and phase space distributions* / 58
- 4.2 *Single superatom* / 61
 - 4.2.1 *Setup and Wigner functions* / 61
 - 4.2.2 *Comparing metrics of non-classicality* / 65
 - 4.2.3 *Sensitivity on dephasing and dissipation* / 67
- 4.3 *Multiple Superatoms* / 68
- 4.4 *Observation and application of the non-classical state* / 73
 - 4.4.1 *Homodyne Detection* / 73
 - 4.4.2 *Application in quantum metrology* / 76
- 4.A *Exact density matrix for short bins* / 83

5 Photon subtraction with cascaded superatoms

87

- 5.1 *Optimal parameters for a single-photon subtractor* / 88
 - 5.1.1 *Perfect absorption of a single-photon Fock state* / 88
 - 5.1.2 *Optimal absorption with resonant, coherent light* / 90
 - 5.1.3 *Influence of Raman decay* / 92
- 5.2 *Experimental results and scaling to multiple superatoms* / 95
 - 5.2.1 *Discussion of the experiment* / 95
 - 5.2.2 *Scaling to multi-photon subtractors* / 99
- 5.A *Bright and dark state population for a single input photon* / 100
- 5.B *Monte-Carlo Model* / 102

6 Nonexponential decay in multiple-emitter chains

105

- 6.1 *The bidirectional waveguide* / 107
- 6.2 *Decay of two emitters* / 108
 - 6.2.1 *Bidirectional waveguide* / 109
 - 6.2.2 *Chiral waveguide* / 112
- 6.3 *Decay of multiple atoms* / 114
 - 6.3.1 *Chiral waveguide* / 114
 - 6.3.2 *Bidirectional waveguide* / 117
- 6.A *Exact results for the chiral waveguide* / 120
- 6.B *Exact results for the bidirectional waveguide* / 122

7 Collective decay of a single superatom

125

- 7.1 *Superatom decay dynamics* / 126
 - 7.1.1 *Experimental Setup* / 126
 - 7.1.2 *Superatom decay* / 128
 - 7.1.3 *Four-level model* / 130

Contents

- 7.2 *Microscopic motivation for the four-level model* / 132
 - 7.2.1 *Chiral exchange-interaction in the subradiant basis* / 133
 - 7.2.2 *Comparison with the four-level model* / 135
- 7.A *Exchange Hamiltonian in the subradiant basis* / 137

Ausführliche Zusammenfassung in deutscher Sprache

141

Acknowledgements

155

Bibliography

159

1

Rydberg superatoms

This thesis examines the interactions between light and collections of Rydberg atoms. Rydberg atoms are hydrogen-like emitters, excited to states of large principle quantum numbers n [1–3]. These large excitations result in strong dipole-dipole interactions [4–7] between Rydberg atoms, giving rise to effects like the *Rydberg blockade* [8–14], where a single excited Rydberg atom prohibits secondary excitations in its vicinity. These dipole-dipole interactions make Rydberg atoms promising candidates for numerous applications [15, 16], for example, quantum information processing with neutral atoms [17]. After it was demonstrated that Rydberg atoms are suitable to build individual quantum gates [8, 18–21], they are now actively used as quantum simulators based on Rydberg atoms in optical lattices [22–32], while more generic “quantum computers” based on Rydberg atoms are current lines of research [33–39].

Beyond quantum information technologies, Rydberg atoms possess further applications in quantum optics. For example, ensembles of Rydberg atoms in an *electromagnetically induced transparency* setup [40] show substantial optical non-linearities [41–43] due to the Rydberg blockade mentioned above, resulting in Rydberg atom-mediated photon-photon interactions [13, 44–46]. Furthermore, the large dipole-dipole interaction can be used to activate mesoscopic structures [47], like atomic monolayer mirrors [48, 49], or to mediate interactions

between trapped ions [50, 51].

One extreme case of the non-linear response occurs when the Rydberg atom ensemble is concentrated in a dense cloud with an extent smaller than the *blockade radius*, i.e., the virtual sphere in which a single Rydberg excitation leads to the blockade of all other atoms. We call these ensembles *Rydberg superatoms* [14, 52] due to their inability to absorb more than a single-photon. The multiple emitters in the superatom collectively contribute to the light-matter interaction, which results in a superradiant response to the light field [53–56], leading to an enhanced light-superatom coupling [57–60].

In this thesis, we study the interaction of light with Rydberg superatoms and analyse the distribution of the emitted light field as well as the dynamics of the superatoms. This chapter focuses on the Rydberg superatoms in isolation. We will first describe the central mechanisms in forming a Rydberg superatom, which are the Rydberg blockade, the excitation of the high-lying Rydberg states, and the superradiant atom-light interactions, and then explain one experimental realisation in detail.

Rydberg Blockade

1.1

Before going into a full quantum mechanical calculation, let us first explain the Rydberg blockade in a semi-classical analogy. First, we imagine an ensemble of atoms in their respective ground states. If the atom separation is sufficiently large, each atom looks like a chargeless particle from the perspective of all other atoms. Next, we excite the system and drive one of the atoms into a Rydberg state. Since the radial distance $\langle r \rangle$ of an electron in a hydrogen-like atom scales as n^2 , we may consider the excited electron and the positively charged remainder of the excited atom as two well-separated objects in a classical picture. The

other, still un-excited, atoms feel the presence of the newly created dipole in the system and their level structure will be subsequently shifted. For atoms in the vicinity of the excited one, this level shift will bring these atoms out of resonance with the wavelength used to excite the first atom. Thus we created a virtual sphere around the excited atom, in which no second excitation is possible.

This simple, heuristic description of the Rydberg blockade qualitatively captures the relevant mechanisms at play. We will now turn to a more technical discussion, which formalises the above argument and allows us, for example, to calculate the blockade radius for a given Rydberg state. Our argument follows the discussion in the review of Sibalic and Adams [3].

To begin, consider two atoms in a specific Rydberg state $|nS\rangle$ with energy E_n . One atom may decay to a lower lying state $|n'P\rangle$ at energy $E_{n'}$, while the other absorbs the available energy to reach $|n''P\rangle$ at energy $E_{n''}$, as indicated by the level diagram to the right. Typically, there are no states such that the energy condition $E_{n'} + E_{n''} = 2E_n$ is met while not violating any other selection rules. Hence this process is not a dominant decay channel. Nevertheless, it may still give rise to an energy correction of E_r in a second-order *Van der Waals* process. In second-order perturbation theory, the energy scales as $V(R)^2/\Delta_E$, where V is the dipole-dipole interaction between the atoms, scaling as n^4/R^3 for Hydrogen like atoms, and $\Delta_E = E_{n'} + E_{n''} - 2E_n$.

Overall, the energy correction for the Rydberg-Atoms becomes $\propto n^8/\Delta_E R^6$. For neighbouring states, we have $\Delta_E \propto 1/n^3$, such that the Van der Waals interaction potential scales like $V_{\text{vdW}}(R) \propto n^{11}/R^6$.

If the atoms are excited into the Rydberg state $|nS\rangle$ by a laser with linewidth ν , then a distance R_B exists for which $V_{\text{vdW}}(R_B) = \hbar\nu$. This brings us to our previous explanation: After exciting a single atom, all atoms within a sphere of

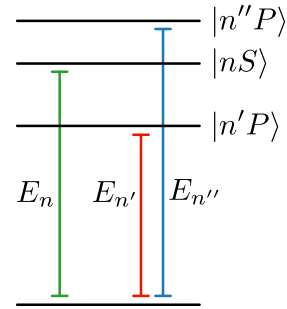


Figure 1.1
Level diagram of the virtual energy exchange.

radius R_B will have too large of a detuning for any second excitations. If every atom lies within this sphere, we call the atom cloud blockaded. If, on the other hand, the extent of the atom ensemble surpasses the Rydberg blockade radius, then the ensemble can host multiple excitations. These excitations, quasiparticles denoted as Rydberg-polaritons [61–64], are subject to the aforementioned strong Van der Waals interactions [65, 66] that can be used to mediate effective photon-photon interactions [67].

Two-photon transitions

1.2

Let us specify a common method for exciting atoms into the Rydberg manifold. Typically, single-photon transitions are impractical, as we can see from a simple energy argument. For this, we discuss Rubidium, which we will consider our primary Rydberg atom for the rest of this thesis. It has an ionisation energy of about 4.2 eV [68], corresponding to wavelengths of < 300 nm. Since the Rydberg states lie close to the ionisation threshold, single-photon-photon transitions to the Rydberg manifold require ultraviolet light.

We can, however, stay in the optical wavelengths if we instead use a two-photon process. Here, we first populate a short-lived intermediate state $|e\rangle$ from which we then drive a second excitation into the Rydberg state $|r\rangle$, as sketched in the figure to the right. For the derivation here, let us consider a classical picture for the light, i.e., the light is described by its coherent amplitudes, resulting in Rabi oscillations of Rabi frequency Ω_e between the ground state $|g\rangle$ and $|e\rangle$ and of frequency Ω_r for the $|e\rangle$ to $|r\rangle$ transition. Assuming a possible detuning Δ and decay Γ on the $|e\rangle$ level, together with a

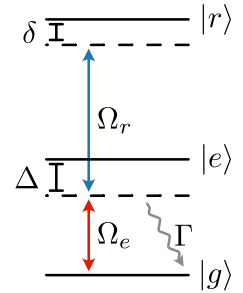


Figure 1.2
Level diagram of the two-photon process.

δ -detuning on two-photon resonance, this brings us to the Hamiltonian in the rotating frame

$$H = \frac{1}{2} \begin{pmatrix} 0 & \Omega_e & 0 \\ \Omega_e & 2\Delta + i\Gamma & \Omega_r \\ 0 & \Omega_r & 2\delta \end{pmatrix} \quad (1.1)$$

for the evolution of a single atom.

The Hamiltonian (1.1) gives rise to an interesting effect. On the one hand, it is clear that if the detuning Δ or Γ is large, then $|e\rangle$ will have a negligible population. Since we can reach $|r\rangle$ only through $|e\rangle$, this should imply that we will also not be able to populate the Rydberg state. On the other hand, at two-photon resonance $\delta = 0$, the state $\Omega_r|g\rangle - \Omega_e|r\rangle$ is an eigenstate of H , and thus the time evolution of $|g\rangle$ will always populate $|r\rangle$, independent of the value of Δ . This shows us that in the $\Delta \rightarrow \infty$ limit, the intermediate state $|e\rangle$ becomes irrelevant and $|g\rangle$ couples directly to $|r\rangle$.

We will now remove the intermediate state $|e\rangle$ by *adiabatic elimination*. Let us denote the solution of the Schrödinger equation as $|\psi\rangle = c_g|g\rangle + c_e|e\rangle + c_r|r\rangle$. The $|e\rangle$ -population will quickly settle into a steady state, where the decay Γ out of $|e\rangle$ is balanced against the incoming probability from the $|g\rangle$ and $|r\rangle$ states. This means that we are justified to approximate $\dot{c}_e = 0$, which is the adiabatic elimination. In practice, this means we solve $\dot{c}_e = (\Omega_e c_g + (2\Delta + i\Gamma)c_e + \Omega_r c_r)/2 = 0$ for c_e and use the result to eliminate c_e from the equations of motion of c_g and c_r .

The assumption of the adiabatic elimination, $\dot{c}_e \approx 0$, is well-met for $\Delta \gg \Omega_e$. With this, the reduced Hamiltonian for the $\{|g\rangle, |r\rangle\}$ system becomes

$$\tilde{H} \approx \frac{1}{2} \begin{pmatrix} 0 & \frac{\Omega_e \Omega_r}{2\Delta} \\ \frac{\Omega_e \Omega_r}{2\Delta} & 2\delta + \frac{\Omega_r^2}{2\Delta} + i\Gamma \frac{\Omega_r^2}{(2\Delta)^2} \end{pmatrix} \equiv \frac{1}{2} \begin{pmatrix} 0 & \tilde{\Omega} \\ \tilde{\Omega} & 2\tilde{\delta} + i\tilde{\Gamma} \end{pmatrix}, \quad (1.2)$$

where we additionally assumed $\Delta \gg \Gamma$. Thus the ground state and Rydberg state are coupled via an effective Rabi frequency $\tilde{\Omega} = \Omega_e \Omega_r / 2\Delta$ and the Rydberg

state now obtains an effective decay rate of $\tilde{\Gamma} = \Gamma\Omega_r^2/(2\Delta)^2$.

From a practical perspective, this result tells us that a two-photon transition barely differs from a single-photon transition, as long as we have strong detuning Δ on the intermediate state. Our approach for the adiabatic elimination remains valid when we replace the classical light fields with their quantised counterparts, as long as the photon intensity in the light field of the $|g\rangle \leftrightarrow |e\rangle$ transition is weak compared to Δ . In the following, we will always consider classical light for the $|e\rangle \leftrightarrow |r\rangle$ transition, while we sometimes treat the frequencies for the $|g\rangle \leftrightarrow |e\rangle$ transition in a fully quantised way.

Interaction of light with a Rydberg gas

1.3

The last section showed that a spatially localised ensemble of atoms exhibits Rydberg blockade, by which the ensemble can absorb only one quanta of light at any given time. This should, however, not be taken as an indication that the dynamics of the atoms are trivial — at least not without further investigation — as each of the atoms may store the excitation, and the single-excitation sector of the atomic Hilbert space is thus as large as the numbers of atoms. Furthermore, excited-unexcited atom pairs interact via photon exchange [69, 70]. Hence an arbitrary excited state will not be stationary, and instead, we should expect that most excited states quickly dephase under the eigenstate dynamics of the exchange interaction.

We dedicate this section to the study of the photon-mediated exchange interaction and the interaction of the atoms with the external light field. In particular, we will put most of our attention on the scattering of a plane-wave photon on the atomic cloud, as this approximates exciting the atoms by an external laser. For this setup, we will find that a single state dominates the evolution of the atoms,

which we call the bright state, reminiscent of the single-photon superradiant state of general N emitter systems [55, 71, 72]. We define the bright state as the state of the atoms immediately after absorbing the single-photon plane wave.

First, we will build up the theoretical framework for the scattering problem. We then solve the equations of motions of the atoms for the evolution of the most relevant excited states of the atom ensemble. Next, we determine the emission from the cloud with the solution for the time evolution of the atoms. Finally, we will summarise our results in a simple yet powerful model for the light-atom interaction. This superatom model will be our description of the light-superatom system for the rest of this thesis, except for the last chapter 7, where we study the limitations of this model.

1.3.1 Theoretical description

Similar to the discussion of the Rydberg blockade, we describe the Rydberg atoms as quantum-mechanical dipoles. This is, we treat the atoms as two-level systems, with the ground state $|g_j\rangle$ and the Rydberg state $|r_j\rangle$ of the j -th atom. This means that the free Hamiltonian of the atoms reads as

$$H_{\text{atoms}} = \hbar \sum_{j=1}^N \omega_0 \sigma_j^+ \sigma_j^-, \quad (1.3)$$

with σ_j^\pm the spin-lowering / -raising operator for the j -th atom and ω_0 denotes the energy of the adiabatically eliminated intermediate state.

For the photons, we ignore the polarisation and describe photons by a scalar field, for simplicity. Thus the free Hamiltonian of the light field becomes

$$H_{\text{photons}} = \hbar \int d^3k \omega_k b^\dagger(\mathbf{k}) b(\mathbf{k}). \quad (1.4)$$

Here, $b^{(\dagger)}(\mathbf{k})$ are the bosonic annihilation (creation) operators for photons in the

mode \mathbf{k} .

The atoms and light modes are coupled within the dipole approximation. Furthermore, we will work within the rotating wave approximation (RWA). At the end of this section we will briefly discuss beyond-RWA-corrections. However, we should already emphasise that the full scattering theory, which we will derive in the next chapter 2, is based on the RWA and agrees excellently with the experimental observations. The interaction Hamiltonian in the rotating frame (i.e., the interaction picture) thus reads as

$$H_{\text{int}}(t) = \sum_{j=1}^N \sum_{\mathbf{k}} \sqrt{\frac{J(\omega_{\mathbf{k}})}{\tilde{V}}} \sigma_j^+ b(\mathbf{k}) e^{i\mathbf{k}\mathbf{r}_j - i(\omega_{\mathbf{k}} - \omega_0)t} + \text{h.c.}, \quad (1.5)$$

where $J(\omega)$ denotes the spectral density of the atoms for the given transition and \tilde{V} is the quantisation volume of the photons.

In the following sections we will study the dynamics of the atoms and the light field under the influence of H_{int} . Additionally, we will assume that each atom is within one blockade radius of each other and we are therefore justified to limit the discussion to the single-excitation sector. As a particularly important example we consider that the cloud is excited by a resonant plane-wave $|\mathbf{k}_0, G\rangle = b^\dagger(\mathbf{k}_0)|0, G\rangle$, with $ck_0 = \omega_0$. Here, $|0\rangle$ denotes the photonic vacuum and $|G\rangle = |g_1, \dots, g_N\rangle$ the collective ground state of all N atoms. In a first order process $|\mathbf{k}_0, G\rangle$ excites the atoms into the equal superposition state

$$|0, W\rangle \equiv \frac{1}{\sqrt{N}} \sum_{j=1}^N e^{i\mathbf{k}_0\mathbf{r}_j} \sigma_j^+ |0, G\rangle \equiv \sigma_W^+ |0, G\rangle \propto H_{\text{int}}(0) |\mathbf{k}_0, G\rangle, \quad (1.6)$$

which defines the bright state $|W\rangle$ of the mode \mathbf{k}_0 .

The bright state will turn out to be the most important state in the evolution of the superatom for three reasons. Firstly, as we just discussed, it describes the state of a superatom directly after absorbing a plane-wave photon. Additionally, $|W\rangle$

dominates the evolution of the superatom after this initial condition, especially in the absence of additional incoherent processes. Lastly, we will also see, that the decay of the bright state predominantly creates photons with the wave vector \mathbf{k}_0 , i.e., the scattering approximatively conserves the photons momentum and direction. This is due to the phase information, that is stored within (1.6), which will result in destructive interference in every direction but \mathbf{k}_0 .

Due to the singular importance of $|W\rangle$ we should formulate our theory in a basis, that emphasises its central role. For this we will perform a Krylov expansion about $|W\rangle$, which identifies the atomic states with the most dominant coupling to $|W\rangle$. For this, we start with the bright state and generate the next basis state by a Gram-Schmidt ortho-normalisation¹ of $H_{\text{int}}^2(0)|W\rangle$. This results in the state $|C\rangle$ with the strongest coupling to $|W\rangle$ at time $t = 0$. We can iteratively continue to generate new basis states from $H_{\text{int}}^{2n}(0)$ until we arrive at a full basis, or halt when the truncated basis yields a sufficiently accurate description. We will see that under suitable conditions on the spatial distribution of the atoms it is generally justified to only take one additional state into account. This implies that the superatom is generally well-described as a 3-level system which will be the general assumption in most parts of this thesis.

The following pages contain the technical derivation of the effective equations of motion for the Krylov states. Readers, who are mainly interested in the physical discussion may skip to the end of this section, where we list the relevant equations of motions, or directly to one of the following sections, where we discuss the internal dynamics of the superatom, calculate the emission statistics and compare our theory to alternative derivations.

Before we involve ourself in the technical details let us further motivate our strategy. On the first glance the obvious choice is to work in the natural basis $|0, j\rangle = \sigma_j^+ |0, G\rangle$. However, vacuum fluctuation of the light field leads to a Lamb shift of the atoms [71, 73]. The Lamb shift depends on the exact form of the

¹We need to square H_{int} here, to obtain a state in the excited atom manifold.

spectral density $J(\omega)$, which is typically not known exactly. However, an accurate description of the atom system by a Lindblad master equation only requires that J is flat at the relevant frequencies and drops of sufficiently fast at $\omega \rightarrow \infty$ [74]. Within our Krylov expansion, we will only make use of these two conditions without ever requiring precise knowledge of $J(\omega)$. Beyond this, we already established that $|W\rangle$ will always be the starting point of the atom's evolution, as long as we consider incoming plane-waves. Hence, unless we are not interested in more general initial conditions, this approach is the most practical approach for an accurate descriptions with just a handful of states.

To start the derivation of the effective equation of motions for the atomic states, we first remember that the bright state (1.6) stores the phase information of the previously absorbed photon. These phases naturally occur due to our choice of the initial plane-wave $|\mathbf{k}_0\rangle$ and we should include them directly in the atomic operators $\sigma_j^+ e^{i\mathbf{k}_0 \mathbf{r}_j} \mapsto \sigma_j^+$, in order to simplify the notation. The bright state now simply reads as $|W\rangle = 1/\sqrt{N} \sum_j \sigma_j^+ |G\rangle$ and we obtain a phase factor $e^{-i\mathbf{k}_0 \mathbf{r}_j}$ in the interaction Hamiltonian 1.5.

Let us now perform the Krylov expansion around $|W\rangle$. The next relevant atomic state occurs by a second-order process after the exchange of a virtual photon between the atoms

$$H_{\text{int}}^2(0)|0, W\rangle = \frac{1}{\sqrt{N}} \sum_{j,l} \int_{\mathbb{R}^3} d^3k J(\omega) e^{i(\mathbf{k}-\mathbf{k}_0)\mathbf{r}_{j,l}} |0, j\rangle, \quad (1.7)$$

where $\mathbf{r}_{j,l} = \mathbf{r}_j - \mathbf{r}_l$.

In the large N limit we realise that

$$\frac{1}{N} \sum_{i=1}^N e^{-i\mathbf{k}\mathbf{r}_i} \rightarrow \langle e^{-i\mathbf{k}\mathbf{r}} \rangle = \varphi^*(\mathbf{k}) \quad (N \rightarrow \infty), \quad (1.8)$$

where $\langle \dots \rangle$ denotes the expectation value with respect to the atoms' spatial

distribution $p(\mathbf{r})$ and φ its respective characteristic function. By the central limit theorem we realise that we may approximate $\sum_j e^{-i(\mathbf{k}-\mathbf{k}_0)\mathbf{r}_j}/N \approx \varphi^*(\mathbf{k}-\mathbf{k}_0)$ for finite but large N at $\mathbf{k} \approx \mathbf{k}_0$. This is a fairly good approximation for about $N = 10^4$ atoms, which is typically achieved in experiments. However, for any finite N we expect that the sum in (1.8) will have periodic revivals as the condition $\mathbf{k}\mathbf{r}_j \approx 2\pi m_j$, $m_j \in \mathbb{Z}$ can be met arbitrarily well for all j simultaneously. Yet, the frequency $\omega = ck$ at which this occurs grows fast with N and these revivals are thus suppressed by $J(\omega)$, since we expect the spectral density to decay exponentially fast at large ω . Hence, we may use (1.8) as an approximation for experimentally relevant systems.

Therefore, expression (1.7) simplifies to

$$\begin{aligned} H_{\text{int}}^2(0)|0, W\rangle &\approx \sqrt{N} \sum_{j=1}^N \int_{\mathbb{R}^3} d^3k J(\omega) \varphi^*(\mathbf{k}-\mathbf{k}_0) e^{i(\mathbf{k}-\mathbf{k}_0)\mathbf{r}_j} |0, j\rangle \\ &\approx (2\pi)^3 \sqrt{N} J(\omega_0) \sum_{j=1}^N p(\mathbf{r}_j) |0, j\rangle. \end{aligned} \quad (1.9)$$

In the second step we used that $J(\omega)$ is approximatively flat around $\omega_0 = ck_0$. More precisely, if σ is a characteristic length scale of $p(\mathbf{r})$ then J does not change significantly on scales c/σ . As $p(\mathbf{r}) \geq 0$ it is clear that this state still possess an overlap $|W\rangle$, which we need to remove. After applying the Gram-Schmidt ortho-normalisation we find

$$|C\rangle = \frac{\mathcal{N}}{\sqrt{N}} \sum_{j=1}^N \left[p(\mathbf{r}_j) - \frac{1}{V} \right] |j\rangle \equiv \sigma_C^\dagger |G\rangle \quad (1.10)$$

as the state that is most strongly coupled to $|W\rangle$. Here \mathcal{N} is a normalisation factor depending on the distribution of the atoms, and V denotes the Süssmann volume

$$\frac{1}{V} \equiv \int_{\mathbb{R}^3} d^3r p(\mathbf{r})^2, \quad (1.11)$$

which should not be confused with the quantisation volume \tilde{V} .

In principle we can now iterate this procedure, i.e., apply $H_{\text{int}}^2(0)$ on $|0, C\rangle$, to find the next most relevant atomic state. In the next sections we will find however, that $|W\rangle$ and $|C\rangle$ are weakly coupled and since we are primarily interested in $|W\rangle$'s evolution we may neglect other states that only influence $|C\rangle$ directly and work in the truncated $\{|W\rangle, |C\rangle\}$ basis. In this basis we have

$$\sigma_j^\pm \approx \frac{1}{\sqrt{N}}\sigma_W^\pm + \frac{\mathcal{N}}{\sqrt{N}}\left[p(\mathbf{r}_j) - \frac{1}{V}\right]\sigma_C^\pm, \quad (1.12)$$

which we obtain by projecting on $|W\rangle$ and $|C\rangle$ respectively. This yields the interaction Hamiltonian

$$\begin{aligned} H_{\text{int}}(t) \approx & \sqrt{N} \sum_{\mathbf{k}} \frac{\sqrt{J(\omega_{\mathbf{k}})}}{\sqrt{\tilde{V}}} \varphi(\mathbf{k} - \mathbf{k}_0) \sigma_W^+ b(\mathbf{k}) e^{-i(\omega_{\mathbf{k}} - \omega_0)t} \\ & + \sqrt{N} \mathcal{N} \sum_{\mathbf{k}} \frac{\sqrt{J(\omega_{\mathbf{k}})}}{\sqrt{\tilde{V}}} \left[\varphi^{(2)}(\mathbf{k} - \mathbf{k}_0) - \frac{\varphi(\mathbf{k} - \mathbf{k}_0)}{V} \right] \sigma_C^+ b(\mathbf{k}) e^{-i(\omega_{\mathbf{k}} - \omega_0)t} \\ & + \text{h.c.}, \end{aligned} \quad (1.13)$$

in this truncated basis, with $\varphi^{(2)} = \mathcal{F}[p^2]$ the Fourier transformation of $p^2(\mathbf{r})$.

We now consider the single-excitation state

$$|\psi(t)\rangle = \sum_{\mathbf{k}} \psi_{\mathbf{k}}(t) |\mathbf{k}, G\rangle + \alpha_W(t) |0, W\rangle + \alpha_C(t) |0, C\rangle \quad (1.14)$$

and we find the equations of motions for the coefficients

$$\begin{aligned} \dot{\psi}_{\mathbf{k}}(t) &= \frac{1}{i\hbar} \sqrt{N} \frac{\sqrt{J(\omega_{\mathbf{k}})}}{\sqrt{\tilde{V}}} \varphi_W^*(\mathbf{k} - \mathbf{k}_0) e^{i(\omega_{\mathbf{k}} - \omega_0)t} \alpha_W(t) \\ &\quad + \frac{1}{i\hbar} \sqrt{N} \frac{\sqrt{J(\omega_{\mathbf{k}})}}{\sqrt{\tilde{V}}} \varphi_C^*(\mathbf{k} - \mathbf{k}_0) e^{i(\omega_{\mathbf{k}} - \omega_0)t} \alpha_C(t), \end{aligned} \quad (1.15a)$$

$$\dot{\alpha}_W(t) = \frac{1}{i\hbar} \sqrt{N} \sum_{\mathbf{k}} \frac{\sqrt{J(\omega_{\mathbf{k}})}}{\sqrt{\tilde{V}}} \varphi_W(\mathbf{k} - \mathbf{k}_0) e^{-i(\omega_{\mathbf{k}} - \omega_0)t} \psi_{\mathbf{k}}(t), \quad (1.15b)$$

$$\dot{\alpha}_C(t) = \frac{1}{i\hbar} \sqrt{N} \sum_{\mathbf{k}} \frac{\sqrt{J(\omega_{\mathbf{k}})}}{\sqrt{\tilde{V}}} \varphi_C(\mathbf{k} - \mathbf{k}_0) e^{-i(\omega_{\mathbf{k}} - \omega_0)t} \psi_{\mathbf{k}}(t). \quad (1.15c)$$

with $\varphi_W(\mathbf{k}) = \varphi(\mathbf{k})$ and $\varphi_C(\mathbf{k}) = \mathcal{N}[\varphi^{(2)}(\mathbf{k}) - \varphi(\mathbf{k})/V]$.

1.3.2 Internal dynamics of the superatom

We now determine the evolution of a superatom starting from the bright state $|W\rangle$. For this we will first eliminate the photon amplitudes $\psi_{\mathbf{k}}$ from the equations of motions of α_W and α_C . We will arrive at a simple coupled system of equations for these two superatom states, which we explicitly solve for a Gaussian atom distribution. For this distribution in particular we find that the extend of the trapped atoms (here the variances of the Gaussians) only alter the overall time scale, but not the quantitative evolution of α_W and α_C and we find that the $|C\rangle$ state never carries more than $\approx 5\%$ of the total probability, thus justifying our truncated basis-approach.

To eliminate $\psi_{\mathbf{k}}$ from (1.15b) and (1.15c) we formally integrate the equation for $\dot{\psi}_{\mathbf{k}}$ and insert the solutions into the equations of motion of α_W and α_C . This

results in

$$\begin{aligned} \dot{\alpha}_a(t) = & -\frac{N}{\hbar^2} \sum_{b \in \{C, W\}} \int_0^t ds \alpha_b(s) \int_{\mathbb{R}^3} d^3k J(\omega_k) \\ & \times \varphi_a(\mathbf{k} - \mathbf{k}_0) \varphi_b^*(\mathbf{k} - \mathbf{k}_0) e^{-i(\omega_k - \omega_0)(t-s)}, \quad a \in \{W, C\} \end{aligned} \quad (1.16)$$

For a broad atom distribution² the characteristic functions φ_a are sharply peaked around $\mathbf{k} \approx \mathbf{k}_0$. Since we assumed J to be quite flat we simply replace it by $J(\omega_0)$. Similarly, we perform a first order Taylor expansion of the exponential $\omega_k \approx \omega_0 + c(\mathbf{k} - \mathbf{k}_0) \cdot \hat{\mathbf{k}}_0$. Notice, that we find a characteristic frequency of $\omega_0 = ck_0 \sim 300$ THz, which is much faster than the intrinsic dynamic of the superatom which is in the MHz regime. Nevertheless, the Taylor-approximation is well-justified, which we show in the appendix 1.A of this chapter, where we perform the derivation without the approximation and obtain quantitatively the same result. Thus, we focus here on the much simpler approach.

We now turn our attention to the time dependence in the equations of motion (1.16). For this, we may realise that the k -integral effectively gives the L^2 inner product between the two functions $\varphi_a(\mathbf{k})e^{-ick \cdot \hat{\mathbf{k}}_0(t-s)}$ and $\varphi_b(\mathbf{k})$. We use that the Fourier transformation is unitary so we may equivalently perform this inner product in real space. Then we change the order of the integrations and find for the time integral in equation (1.16)

$$\begin{aligned} & \int_0^t ds \alpha_b(s) \mathcal{F}^{-1} \left[\varphi_a(\mathbf{k}) e^{-ick \cdot \hat{\mathbf{k}}_0(t-s)} \right] (\mathbf{r}) \\ & = \int_0^t ds \alpha_b(s) \begin{cases} p(\mathbf{r} - c\hat{\mathbf{k}}_0(t-s)) & a = W \\ \mathcal{N} \left[p^2(\mathbf{r} - c\hat{\mathbf{k}}_0(t-s)) - \frac{p(\mathbf{r} - c\hat{\mathbf{k}}_0(t-s))}{V} \right] & a = C \end{cases} \end{aligned} \quad (1.17)$$

For the experiment we outline in section 1.4 we have a trap size of $10 \mu\text{m}$. Thus,

²For the previously discussed experimental parameters we have a characteristic size of $\sigma \sim 10 \mu\text{m}$, so that $\sigma k_0 \sim 10$.

the significant timescale in $p_z(z - ct)$ is limited to a few femtoseconds, much faster than any other timescale in our system. We may thus replace $\alpha_b(s)$ with $\alpha_b(t)$ in (1.17) and therefore also in the equations of motion (1.16). Since the atomic distribution quickly decays, there should be no relevant difference whether we integrate s on $(0, t)$ or extend the domain to $(-\infty, t)$. With the extended domain we may substitute $u = c(t - s)$ and find that the remaining integrals are independent of t and the equations of motion are Markovian to a good approximation.

In summary we end up with the equations of motion

$$\dot{\alpha}_a(t) = -\frac{(2\pi)^3}{c\hbar^2} N J(\omega_0) \sum_{b \in \{C, W\}} \gamma_{ab} \alpha_b(t), \quad (1.18)$$

where the coupling matrix elements

$$\gamma_{ab} = \int_0^\infty du \int_{\mathbb{R}^3} d^3k \varphi_a(\mathbf{k}) \varphi_b^*(\mathbf{k}) e^{-ick \cdot \mathbf{k}_0 u}$$

depend on the specific atom-trap geometry. As an instructive example we consider now a Gaussian atom distribution and assume that \mathbf{k}_0 is aligned with the z -axis of the trap, i.e., $\mathbf{k}_0 = k_0 \mathbf{e}_z$. Then we find the coupling matrix elements

$$\gamma_{WW} = \frac{1}{2A}, \quad \gamma_{WC} = \frac{\mathcal{N}}{V} \frac{1}{6A} = \gamma_{CW}, \quad \gamma_{CC} = \frac{\mathcal{N}^2}{V^2} \frac{1}{6A}, \quad (1.19)$$

with the Süssmann volume and area $V = \prod_{j \in \{x, y, z\}} \sqrt{4\pi\sigma_j^2}$ and

$$A = \left(\int_{\mathbb{R}^2} dx dy p_x^2(x) p_y^2(y) \right)^{-1} = \prod_{j \in \{x, y\}} \sqrt{4\pi\sigma_j^2}, \quad (1.20)$$

respectively. The normalisation factor of $|C\rangle$ becomes $\mathcal{N} = V / (\sqrt{64/27} - 1)$, and σ_j denote the standard deviation of the Gaussian distribution in the three

1 Rydberg superatoms

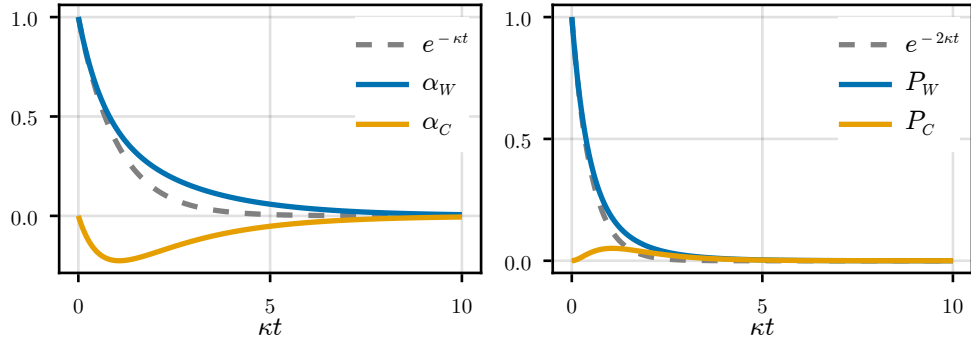


Figure 1.3

Amplitudes of the bright state and second most relevant state for a Gaussian atom distribution and the respective probabilities. Overall the bright state evolution mostly resembles an exponential decay, however, modified compared to the decay without any coupling to $|C\rangle$ (dashed line). The $|C\rangle$ -probability initially increases, but accounts for about 5% of the total population before decaying again.

directions. Interestingly, for the Gaussian distribution, all physical quantities can be collected in the single coupling rate

$$\kappa = \frac{(2\pi)^3 NJ(\omega_0)}{c\hbar^2 2A}, \quad (1.21)$$

which defines the time scale of the bright state decay, while the numerical quantity $\mathcal{N}/V = (\sqrt{64/27} - 1)^{-1} \approx 1.85$ completely controls the qualitative behaviour of α_W and α_C . We want to emphasise at this point that the coupling strength κ scales with the number of atoms, which is one of the key reasons that the interaction of light with superatoms is observable in experiments with only a few photons and represents the superradiant nature of $|W\rangle$.

Figure 1.3 shows the amplitudes and populations in the $|W\rangle$ and $|C\rangle$ states. Most importantly we find that the auxiliary state $|C\rangle$ accounts for $\approx 5\%$ of the total population at most. Below, we will compare our results to values from the literature and find that under different assumptions the chance for secondary

excitations can be higher. Yet our approach shows one key feature: even when accounting for the dipole-dipole interaction of the atoms, the decay of the bright state is predominantly exponential, although with a slightly modified rate, as can be seen in figure 1.3.

It should be also noted that we focused on the coherent exchange of virtual photons for the atom-atom interactions. Yet, there are additional coherent and incoherent mechanism which influence the time evolution of the atoms and excite states orthogonal to $|W\rangle$. For example, as the states depend on the explicit position of the atoms positions, thermal motion and fluctuations in the atom-trap will impact the superatom evolution. At the end of this chapter we will discuss how we include these effects in an effective superatom model.

1.3.3 Emission from an excited superatom

We are now familiar with the intrinsic dynamics of a superatom and have seen that its decay from the bright state $|W\rangle$ is well-captured by an exponential decay of $|W\rangle$ with a weak coupling to an additional state $|C\rangle$. Now we want to determine the state of the photon, after its interaction with the superatom under this process. The photon state is captured by the coefficient $\psi_{\mathbf{k}}$, which we directly obtain from integrating (1.15a).

Hence the asymptotic photon state is given by

$$\begin{aligned} \psi_{\mathbf{k}}(\infty) &= \frac{1}{i\hbar} \sqrt{N} \frac{\sqrt{J(\omega_k)}}{\sqrt{\tilde{V}}} \varphi_W^*(\mathbf{k} - \mathbf{k}_0) \int_0^\infty dt e^{i(\omega_k - \omega_0)t} \alpha_W(t) \\ &+ \frac{1}{i\hbar} \sqrt{N} \frac{\sqrt{J(\omega_k)}}{\sqrt{\tilde{V}}} \varphi_C^*(\mathbf{k} - \mathbf{k}_0) \int_0^\infty dt e^{i(\omega_k - \omega_0)t} \alpha_C(t). \end{aligned} \quad (1.22)$$

As the equations of motions (1.18) for the coefficients α_W , α_C resulted in a coupled system of first order differential equations we know that $\alpha_W(t)$ and

1 Rydberg superatoms

$\alpha_C(t)$ are generally described by a superposition of two exponential decays

$$\alpha_a = c_a^{(1)} e^{-\kappa_1 t} + c_a^{(2)} e^{-\kappa_2 t}, \quad a \in \{W, C\},$$

where κ_j is one of the eigenvalues of the coefficient matrix $\kappa\gamma_{ab}$ (1.19). Consequently, the integrals in (1.22) results in $1/(\kappa_j - i(\omega_k - \omega_0))$. Given a coupling rate κ in the MHz regime, this denominator already vanishes for deviations of k from k_0 on the order of fm^{-1} . Thus emission from the $|C\rangle$ state can be completely neglected, as $\varphi_C(0) = 0$ and since relevant changes of $\varphi_C(\mathbf{k})$ only occur on the scale $1/\sigma$, with the atom-trap size $\sigma \sim 10\mu\text{m}$. Therefore, we find that the asymptotic photon state is well-described by

$$\psi_{\mathbf{k}}(\infty) \approx \frac{1}{i\hbar} \sqrt{N} \frac{\sqrt{J(\omega_k)}}{\sqrt{\tilde{V}}} \varphi_W^*(\mathbf{k} - \mathbf{k}_0) \left[\frac{c_W^{(1)}}{\kappa_1 - i(\omega_k - \omega_0)} + \frac{c_W^{(2)}}{\kappa_2 - i(\omega_k - \omega_0)} \right]. \quad (1.23)$$

This is to say that the photon is dominantly emitted into the \mathbf{k}_0 direction, which was the original direction of the photon before the scattering.

The interaction of a resonant photon with a superatom therefore approximatively preserves the wave vector of the photon and the scattering is thus mostly one-dimensional. Even more, we also see that backscattering is almost completely suppressed. We will refer to this one-dimensional and uni-directional scattering as *chiral* emission in the following. It is one of the most crucial components in the effective superatom model, which we postulate at the end of this chapter.

1.3.4 Comparison to the literature

In the last sections we employed specific assumptions about our system in the derivations of the two central results: The bright state captures most of the superatom dynamics and the emission is chiral, i.e., almost perfectly conserves

the wave vector. Before we now continue and summarise these results in an effective model for the superatom, we should first gauge whether our approach was justified. Luckily for us, in the late 2000s and early 2010s the decay of a weakly excited cloud and the subsequent photon emission was studied in great detail and with multiple complementary approaches [56, 75–82], to which we will compare our results in this section. In particular, we will go over the early works of Scully and coworkers [75–77], and the article by Manassah [56]. These articles and our approach follow slightly different assumptions and employ different approximations, while aiming to answer similar questions. Consequently, this comparison of notes allows us to justify our previous discussions.

Firstly, let us summarise the articles of Scully et al. [75–77]. These articles study the decay of an atom cloud from the bright state in the dipole and rotating wave approximation. However, the coupling between atomic states, denoted as Agarwal-Fano coupling [83] in these articles, is ignored. In this regard, these articles resemble our theory, with the Krylov expansion halted only after the first state, i.e., the bright state. Scully and coworkers find the exponential decay of the bright state and perfect chiral emission for an atomic sample of size $\sigma \gg 1/k_0$, which nicely coincides with our results. Additionally, the most recent article [77] studies large atomic clouds ($\sigma \gg c/\kappa$), where light-propagation through the entire cloud requires more time than the internal dynamics of the superatom and retardation effects cannot be neglected. Here, the bright state undergoes periodic decays and revivals with rate κ (which used to be the decay rate), while the overall bright state decay occurs on the timescale σ/c .

These early articles thus verify our results from the last sections. However, they lack the inclusion of atom-atom interaction, which we already determined to be potentially relevant. Thus, we now turn to the article by Manassah [56], who numerically determined the full excitation probability without truncating atomic states as we did.

Manassah treated the atoms as quantum-mechanical dipoles in a spherically

homogeneous geometry. With the assumption that the atomic density is large enough to treat the atoms as a continuous field β , he arrives at an integro-differential equation

$$\partial_t \beta(\mathbf{r}, t) = \int d\mathbf{r}' G(\mathbf{r} - \mathbf{r}') \beta(\mathbf{r}', t), \quad (1.24)$$

which he solves numerically via an eigenvalue expansion. He then finds the probability that the cloud is excited, without being in the bright state, to reach a maximal value of about 17 %.

Our lower estimation of 5 % is exclusively due to our truncation of the Krylov basis. While Manassah considers corrections beyond the rotating wave approximation in his article, these altogether drop out in his integral Kernel $G(\mathbf{r})$ ³. We could also expect the spherical homogeneous geometry to be the culprit of the large chance for secondary excitations, yet follow-up research on Gaussian traps [80] showed similar large probabilities for secondary excitations.

We see that our truncated Krylov basis approach results in the correct behaviour for the photon emission, but we should ask ourselves whether it is suitable to describe the superatom state, especially since we saw that we are underestimating secondary excitations. Manassah's article, however, showed that the bright state has an initial exponential decay. The decay then slows down due to the repopulation of the bright state from the secondary excitations. However, this only occurs after the bright state population is already down to $P_W < 10^{-3}$. In a full treatment, the secondary excitations thus increase the decay rate but barely lead to revivals of the bright state population, contrary to what we found. In this regard, our truncated basis even over-estimates the impact of secondary

³The kernel is derived in [78]. Here the one-photon-two-atom excitation sector is included as a correction beyond the rotating wave approximation, which yields an $e^{-i\omega_0 t}$ term in the atomic equations of motions, as can be seen in the articles equation (2.15). However, this term vanishes later since in the integral (2.25) the complex integral may be closed without encircling any residue for this term.

excitations in the long-time evolution of the bright state.

We will later, in chapter 6, study the bright state evolution in more detail, where we solve it exactly in a chiral one-dimensional model and qualitatively reproduce Manassah's three-dimensional results. For now, we will summarise our results in an effective model for the interaction of light with superatoms in the next section.

1.3.5 Effective superatom model

We found two important simplifications in our theoretical analysis of the interaction of a single superatom with a single resonant photon. Firstly, by absorbing a photon, the superatom ends up in the superradiant bright state $|W\rangle$, which by itself almost perfectly describes the evolution of the superatom, as the bright state is only weakly coupled to other non-radiating superatom states, the so-called dark states. Secondly, we found that the decay of the bright state produces photons predominantly with the same wave vector \mathbf{k}_0 as the original photon before the absorption.

These results enable us to formulate a simplified description of the coupled light-superatom system. From here on, we will ignore that the superatom consists of potentially thousand interacting atoms and coarse-grain its description to its collective ground state $|G\rangle$ and the bright state $|W\rangle$. As we discussed above, there is a residual coupling of $|W\rangle$ to the dark state manifold, stemming from both coherent and incoherent processes. For most of this thesis, we will take a simplified approach to this coupling, by which the bright state $|W\rangle$ decays incoherently with rate γ_D into an effective dark state $|D\rangle$. This description will be verified by its overall great agreement with experimental results. We will, however, also encounter situations where this simple picture fails to encompass all physical effects. In this case, we will reformulate our model by taking the coherent interaction of the atoms into account by adding a state $|C\rangle$ and a coherent coupling \varkappa between $|C\rangle$ and $|W\rangle$ to our model.

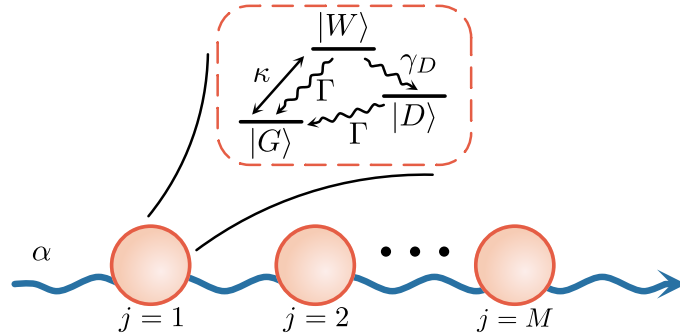


Figure 1.4

Superatoms may simply be considered as three-level atoms, with the indicated level and decay scheme, for most parts of this thesis. Since the interaction of a superatom with the light field is highly directed, as visualised by the blue arrow, we may naturally create a chiral quantum network or multiple chained superatoms.

On the level of the photons the conservation of the wave vector gave rise to the concept of *chirality*. Since the propagation direction of the photons is preserved under the scattering, we can describe the photon propagation in a one-dimensional theory. In a full one-dimensional description we should account for photons traveling to the “left” and “right”. However, since backscattering is strongly suppressed we may also only consider one of these modes. The superatom decay has a slight chance of scattering in any other direction, away from the well-defined photon propagation direction. This process is dominated by the Raman decay of the adiabatically eliminated intermediate states, see equation (1.1). This effect is well-captured by a heuristic Raman decay rate Γ for the superatom, which removes one excitation from our system, as emission in any other direction should do.

Due to the directed emission of single superatom it is easy, at least in concept, to chain up superatoms to build a quantum network of interacting superatoms. Such systems are also implemented by coupling quantum emitters to waveguides or nanofibers [84–89], and, due to this structural similarity, we will also call

our free space setup a *chiral waveguide*. All effects mentioned in the last few paragraphs are summarised in figure 1.4. This sketch summarises our discussion and it conveys the correct image for many of the setups we will study in this thesis.

Experimental Realisation

1.4

We finish this chapter with a discuss on the experimental implementation of Rydberg superatoms. This section will not provide an extensive overview of multiple different platforms or follow the chronological developments in this field. Instead we will put narrow focus on the realisation of Rydberg superatoms by the group of Prof. Sebastian Hofferberth, with whom the author closely collaborated during his doctoral research. All experimental results presented in the later chapters are based on this platform. Here we explain the setup used in the articles [90, 91] for the creation of a single superatom, and the procedure from [92] for the creation of multiple superatoms.

In these experiments S. Hofferberth's group used ensembles of Rubidium (Rb^{87}) atoms. The Rubidium atoms are first loaded from a magneto-optical trap into an optical dipole trap and cooled down to $< 10 \mu\text{K}$, via evaporative methods and Raman sideband cooling. The trap profile is a pancake-like shape with an extension ($1/e$ -width of the Gaussian distribution) of about $\sigma_z = 6.5 \mu\text{m}$ in the short direction and about $\sigma_{x,y} = 10.2 \mu\text{m}$ in the transverse directions. After the cooling step the trap typically contains about 10^4 Rubidium atoms.

The Rubidium atoms are pumped the Rydberg state with a two-photon process in an EIT setup. First a red laser at 780 nm couples the ground state $|g\rangle = |5S_{1/2}, F = 2, m_F = 2\rangle$ to an intermediate state $|e\rangle = |5P_{3/2}, F = 3, m_F = 3\rangle$ with a detuning of $\Delta = 2\pi \cdot 100 \text{ MHz}$. Then a blue laser at 479 nm drives the

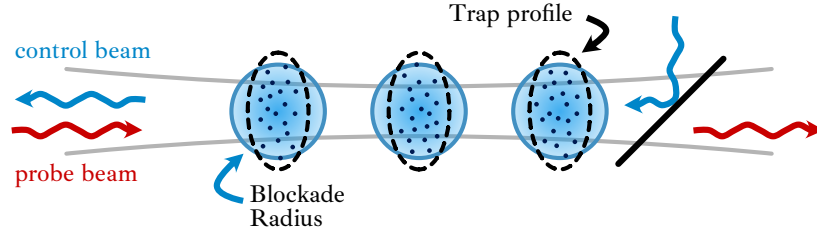


Figure 1.5

Sketch of the experimental setup in the counter-propagating scheme.

transition from $|e\rangle$ to the Rydberg state $|r\rangle = |111S_{1/2}, J = 1/2, m_J = 1/2\rangle$, with overall two-photon resonance for the $|g\rangle \leftrightarrow |r\rangle$ process.

Only the signal of red laser, called probe beam, is detected after interacting with the superatom. For this the blue signal is either filtered out when using a co-propagating beam setup [92] or is directly used in a counter-propagating setup [90, 91]. The counter-propagating setup results in a smaller dephasing γ_D of the Rydberg state into the dark states. This is not always an advantage, as, for example, we will use this platform in chapter 5 to create a single-photon absorber from the superatoms, for which the higher dephasing in the co-propagating setup is explicitly wanted. Since the blue laser effectively turns the Rydberg interaction on, we will denote it as the control beam. The beams are aligned with the short direction of the magneto-optical trap.

For the creation of multiple superatoms the trap geometry is augmented and additional optical traps are needed. First, the atoms are loaded into a cigar-shaped crossed optical dipole trap of radial extend of $6.5\ \mu\text{m}$ and $55\ \mu\text{m}$ length in the transversal direction. The optical dipole trap is then intersected perpendicular by up to three additional tightly focused optical traps. In order to remove atoms between the individual optical traps, the crossed dipole trap is turned off for a short time, but has to be turned on again to provide radial confinement. The number of superatoms generated in this way is limited by the size of the crossed optical dipole trap. This particular setup is summarised in

figure 1.5.

In our model the superatoms are characterised by three parameters: the coupling strength to the probe beam κ , the Raman decay rate Γ and the dephasing rate γ_D into the dark state manifold. Those parameters are experimentally determined by fitting the Rabi profile of a driven superatom to the theoretical model. We will give the precise numerical values later whenever they become relevant. At this moment it is completely sufficient to just discuss their relative magnitude. In the mentioned articles we had $\Gamma \approx 0.02 - 0.2 \mu\text{s}^{-1}$, $\kappa \approx 0.3 - 0.5 \mu\text{s}^{-1}$ and $\gamma_D \approx 1.0 - 2.5 \mu\text{s}^{-1}$ [90–92], i.e., Raman decay typically plays a secondary role and may be neglected occasionally, while the strong dephasing γ_D always has to be considered in any practical discussions.

Appendix: Exact treatment of the energy phase

1.A

In order to solve the k -integration in equation (1.16) we incorporated the frequency by a first order Taylor approximation $\omega_k \approx \omega_0 + c(\mathbf{k} - \mathbf{k}_0) \cdot \hat{\mathbf{k}}_0$. However, by comparing the relevant scales we see that this approximation may not be well-justified. Firstly, $\varphi_a(k)$ changes significantly on scales of $1/\sigma$, which approximately translates into a $0.1 \mu\text{m}^{-1}$ sensitivity in k for the discussed experimental parameters. On the other hand, the experimental timescale is defined by κ , which results in a much greater k sensitivity of $\kappa/\sigma c \approx 3 \cdot 10^8$, i.e., even small changes in k that leave $\varphi_a(\mathbf{k})$ unaltered drastically change the phase in $\exp(-i\omega_k t)$. We now show that the Taylor approximation nevertheless produced the correct result, as long as the atom cloud is much larger as k_0 .

For this we assume a Gaussian trap profile with spherical symmetry and standard deviation σ , and explicitly calculate the k integral in (1.16). For this, we assume that $\mathbf{k}_0 = k_0 \mathbf{e}_z$ and perform the integration in spherical coordinates. For

1 Rydberg superatoms

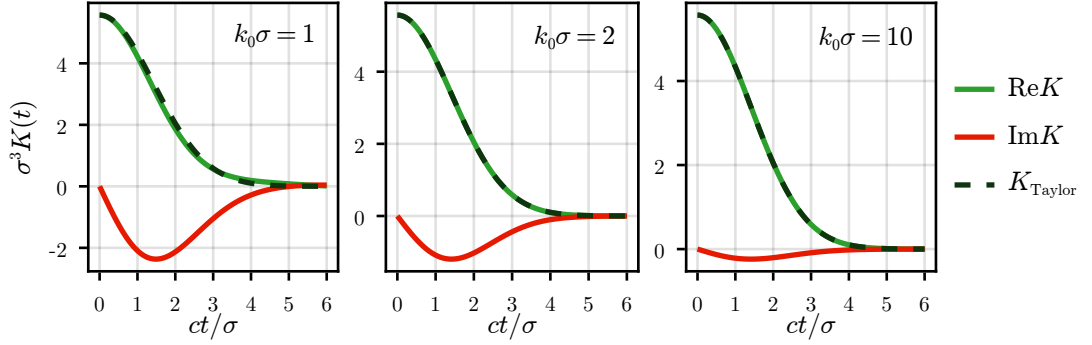


Figure 1.6

Results of the k integral in (1.16) for a Gaussian trap profile. Solid lines indicate the exact results for the real and imaginary part, while the dashed lines represent the result from the Taylor approximation.

simplicity, we just focus on the contributions of $\varphi_W(\mathbf{k}) = \exp(-\sigma^2 k^2/2)$, which results in the kernel

$$\begin{aligned}
 K(t) &= \int_{\mathbb{R}^3} d^3k e^{-\sigma^2(\mathbf{k}-\mathbf{k}_0)^2} e^{-ic(\mathbf{k}-\mathbf{k}_0)t} \\
 &= \int_0^\infty dk \int_0^\pi d\theta \int_0^{2\pi} d\varphi k^2 \sin(\theta) e^{-\sigma^2(k^2 - 2kk_0 \cos(\theta) + k_0^2)} e^{-ic(k-k_0)t} \\
 &= \int_0^\infty dk \frac{\pi k}{k_0 \sigma^2} \left(e^{-\sigma^2(k-k_0)^2} - e^{-\sigma^2(k+k_0)^2} \right) e^{-ic(k-k_0)t} \quad (1.25)
 \end{aligned}$$

This integral can be expressed in terms of error functions, however the exact result does not convey any useful information. Instead, we focus here on the $k_0\sigma \gg 1$ limit and present the exact results below. This coincides with the discussed experiment where $k_0\sigma \approx 10$.

For large k_0 we directly see that the second term in the brackets of (1.25) does not matter. Then we may shift the k integral by k_0 and extend the integration

domain to $(-\infty, \infty)$. This then results in

$$\int_0^\infty dk \left(\frac{\pi}{\sigma^2} + \frac{\pi k}{k_0 \sigma^2} \right) e^{-\sigma^2 k^2 - i c k t} = \frac{\pi^{3/2}}{\sigma^3} e^{-c^2 t^2 / 4 \sigma^2} \left(1 - i \frac{c t}{2 k_0 \sigma^2} \right). \quad (1.26)$$

The real part exactly produces the result from the $\omega_k \approx \omega_{k_0} + c(\mathbf{k} - \mathbf{k}_0) \hat{\mathbf{k}}_0$ approximation, which follows from a simple Fourier transformation

$$K_{\text{Taylor}}(t) = \int_{\mathbb{R}^3} d^3 k e^{-\sigma^2 (k_x^2 + k_y^2 + k_z^2)} e^{-i c k_z t} = \frac{\pi^{3/2}}{\sigma^3} e^{-c^2 t^2 / 4 \sigma^2}. \quad (1.27)$$

Figure 1.6 shows the exact results (1.25) of the k integration for different values of $k_0 \sigma$. We see that already at $k_0 \sigma \approx 2$ there is little difference between the real part of the exact solution and the result obtained from the Taylor approximation of ω_k . The imaginary part only approximatively vanishes at $k_0 \sigma \approx 10$, which is the experimental relevant parameter regime, so we find the Taylor approximation well-justified.

2 Theoretical description of superatom scattering

Now that we have learned about superatoms in the last chapter and derived a simple description of the internal dynamics of an individual superatom, we turn our attention to the interaction of superatoms with the external light field.

Since the light-superatom interaction conserves the wavevector of the photons, we will naturally only consider photons propagating along one direction. We then start with the quantum optical Hamiltonian in one dimension with a dipole-like description of the superatoms and the superatom-photon interaction in the rotating wave approximation. Interestingly, even for multiple atoms, this system has analytic solutions in terms of Bethe states, which we will study first [93–96].

The Bethe states provide every eigenstate of the system and, thus, a complete description of the light-superatom interaction. Yet, these states turn out to be quite cumbersome in any practical calculation, as the number of different Bethe states (equivalent to photonic bound states) grows exponentially with the number of photons. For most applications, we do not need the full information of the emitted light field, but we are content to either be able to determine the field amplitude at some particular point in space or to have all information about **one**

specific spatial mode of emitted light. More clearly, we want to trace out all non-relevant constituents of the entire system and study the reduced dynamics of the remaining degrees of freedom.

This goal is achievable, in particular, due to chirality [97]. Chirality gives rise to simple input-output relations, which relate the incoming light to the emitted light field and the response of the superatoms to the incoming photons [98–100]. The input-output relations allow us to calculate arbitrary n -point correlation functions of the outgoing light field simply by knowing the field by which we drive the atoms and the full quantum statistics of the superatoms. Hence, the correct tool in this situation is the quantum-optical master equation [101–103], where the light field is treated as the bath and traced out, resulting in a master equation for the superatoms. Contrasting full 3d quantum optics, we will find that, up to negligible retardation effects, the quantum optical master equation is exact in chiral systems.

While the quantum optical master equation provides a convenient tool to study correlations in the outgoing light field, we lose all information about the mode profile of the emitted light. We may, however, adapt the superatom’s master equation to encompass **individual** light modes. This theory is based on a powerful framework for quantum input-output networks, like a chiral superatom chain, denoted as the SLH-formalism [104–107]. Within this theory, we place one virtual cavity behind the superatoms for each light mode we want to study. We then have to use specific, time-dependent coupling strengths for the cavities, under which they become transparent only to one specific mode. The asymptotic occupation in the cavity then gives the number statistics of the selected light mode.

In this chapter, we will formulate and review these different formalisms. These formalisms will be the foundation for the analysis in the upcoming chapter.

Bethe Ansatz solutions

2.1

2.1.1 Chiral quantum optical Hamiltonian

We start with the derivation of the full Hamiltonian for the light-superatom system. For this, we will assume, for the moment, that the superatoms are not subject to the Raman decay Γ or the dephasing γ_D . We could already incorporate the dephasing as an imaginary detuning at this point, but we will take care of it when we switch over to the description via the master equation. The Hamiltonian consists of two parts, one describing the chiral propagation of the photons while the second part gives the chiral photon-superatom interaction.

Let us begin with the Hamiltonian for the photon propagation. In a perfect waveguide without dispersion, this Hamiltonian would read as

$$H_{\text{Ph}} = \int_{-\infty}^{\infty} dk \hbar c |k| b^\dagger(k) b(k), \quad (2.1)$$

where $b^{(\dagger)}(k)$ destroys (creates) a photon with momentum k with $[b(k), b^\dagger(k')] = \delta(k - k')$ and all other commutators vanishing.

We, however, need to account for the chiral interaction with the superatoms. For this we first assume, that the superatoms have a resonance frequency ω_0 and only significantly interact with photons within a bandwidth of $2\Delta k$. We may

2 Theoretical description of superatom scattering

thus ignore all other frequencies for the moment

$$\begin{aligned}
 H_{\text{Ph}} &\approx - \int_{-\omega_0/c-\Delta k}^{-\omega_0/c+\Delta k} dk \hbar ck b^\dagger(k) b(k) + \int_{\omega_0/c-\Delta k}^{\omega_0/c+\Delta k} dk \hbar ck b^\dagger(k) b(k) \\
 &= - \int_{-\Delta k}^{\Delta k} dk \hbar (ck - \omega_0) b^\dagger(k - \omega_0/c) b(k - \omega_0/c) \\
 &\quad + \int_{-\Delta k}^{\Delta k} dk \hbar (ck + \omega_0) b^\dagger(k + \omega_0/c) b(k + \omega_0/c). \tag{2.2}
 \end{aligned}$$

By limiting k to the bandwidth we see that $[b(k - \omega_0/c), b^\dagger(k + \omega_0/c)] = 0$. Hence we may treat the fields in the two terms of (2.2) as independent bosonic modes, which we denote as $b_L(k) \equiv b(k - \omega_0/c)$ and $b_R(k) \equiv b(k + \omega_0/c)$ for the moment. These two fields indicate photons propagating to the left and to the right respectively. As the chiral interaction with the superatom does not mix the propagation directions and we will always start with photons moving to the right, we may simply drop the b_L field completely.

We are left with $b_R(k)$ with k limited to $(-\Delta k, \Delta k)$. However, as we already stated, photons beyond this bandwidth will anyway be not relevant for the interaction with the superatom. Thus, we may again extend the k domain to $(-\infty, \infty)$ for convenience and obtain

$$H_{\text{Ph}} = \int_{-\infty}^{\infty} dk \hbar c (k + \omega_0/c) b_R^\dagger(k) b_R(k). \tag{2.3}$$

Finally, as ω_0 is the resonance frequency of the atoms we may go into the rotating frame to drop it from the Hamiltonian. Thus, we end up with the Hamiltonian for chiral photon propagation

$$H_{\text{Ph}} = \int_{-\infty}^{\infty} dk \hbar ck b^\dagger(k) b(k), \tag{2.4}$$

where we now dropped the R -index for simplicity.

Next, we have to specify the photon-superatom interaction. As we already stated, we work within the dipole and rotating wave approximations, so that

$$H_{\text{int}} = \sqrt{\kappa\hbar} \sum_{j=1}^N \left(b^\dagger(x_j)\sigma_j^- + b(x_j)\sigma_j^+ \right), \quad (2.5)$$

where we consider N superatoms at locations x_j , with $\sigma_j^+ = |W_j\rangle\langle G_j| = (\sigma_j^-)^\dagger$, $|G_j\rangle$ and $|W_j\rangle$ denoting the collective ground state and bright state of the j -th superatom respectively. Here, κ denotes the superradiant coupling of the bright state to the light field, as discussed in the previous chapter. As we are in the rotating frame we have already taken care of the energy $\hbar\omega_0$ of the bright state and we do not have to include it here.

2.1.2 Bethe state solutions

The eigenstates of the full Hamiltonian $H = H_{\text{Ph}} + H_{\text{int}}$ follow from the Bethe Ansatz [93, 94]. In this section we will not give a full derivation of the Bethe states, but we will sketch out the necessary steps for the case of a single superatom and then discuss the eigenstates in more detail. We will also limit ourselves to just a single superatom for simplicity, as the N atom derivation follows the same steps. The N atom results can be found in [95, 96]. At the end of this section, we will use the Bethe states to derive the Green's function for scattering n photons on a single superatom, with which we can solve the respective scattering problems. We will use $\hbar = 1 = c$ from here on.

For the Bethe Ansatz solutions one starts by constructing the single-excitation eigenstates. For our Hamiltonian this is straightforward and we obtain a plane-wave like solution

$$|\lambda\rangle = C(\lambda) \int dy f(y, \lambda) e^{i\lambda y} r^\dagger(y, \lambda) |0\rangle, \quad (2.6)$$

2 Theoretical description of superatom scattering

where $|0\rangle$ is the collective photon-superatom ground state, $C(\lambda)$ is a normalisation factor, and

$$f(y, \lambda) = \frac{\lambda - i\kappa/2 \operatorname{sgn}(y)}{\lambda + i\kappa/2},$$

$$r(y, \lambda) = b(y) + \frac{\sqrt{\kappa}}{\lambda} \delta(y) \sigma^-.$$

The quantum number λ in the Bethe Ansatz is commonly called *rapidity*. It gives the eigenenergy $E_\lambda = \lambda$ (in SI units $\hbar c \lambda$) and may be therefore interpreted as the momentum.

Next, we need to construct the eigenstates of the higher excitation sectors. For systems that are solved by the Bethe Ansatz the multi-excitations are simply products of the single-excitation states, with additional prefactors, that account for the exchange of two excitations. For the system at hand this results in the n -particle Bethe states

$$|\lambda\rangle = C_n(\lambda) \int d^n y \prod_{j<l} \left(1 + \frac{i\kappa \operatorname{sgn}(y_j - y_l)}{\lambda_j - \lambda_l} \right) \prod_{j=1}^n f(y_j, \lambda_j) e^{i\lambda_j y_j} r^\dagger(y_j, \lambda_j) |0\rangle, \quad (2.7)$$

with $\lambda = (\lambda_1, \dots, \lambda_n)$.

On a first glimpse, however, it appears that we have not found every eigenstate of H as, for example, the kernel

$$\int_{\mathbb{R}^2} d^2 \lambda |\lambda_1, \lambda_2\rangle \langle \lambda_1, \lambda_2|$$

does not resolve to the identity. This does not happen because the Bethe Ansatz lacks certain states, but since we were too restrictive in our treatment of λ .

As we look for scattering states of a hermitian Hamiltonian we generally have two conditions on the solutions $|\lambda\rangle$: the energies $E_\lambda = \sum \lambda_j$ have to be real and the eigenstates in position space $\langle x_1, \dots, x_n | \lambda \rangle$ have to be bounded. We can

fulfil these conditions with complex λ as well, as long as we form so called strings, i.e., two or more λ_j possess the same real part Λ and differ in the imaginary part by $i\kappa$, with the sum of the imaginary parts vanishing. For example,

$$|\Lambda_3\rangle \equiv |\Lambda - i\kappa, \Lambda, \Lambda + i\kappa\rangle \quad (2.8)$$

gives a three-particle string Bethe state, with central rapidity Λ . We will later see, that these states are related photonic bound states.

In principle, we are now equipped to study scattering problems at a single superatom. In practice, however, the Bethe solutions do not lend themselves to studying more than a few photons as the number of relevant bound states, or Bethe string states, grows as $\exp(\sqrt{n})$ for n excitations. More precisely, there are as many string states for a given number n of excitations as there are ways to partition n into a sum of positive integers. For example, for four photons, we have to consider four independent rapidities, one or two 2-particle string states, a 3-particle string state and a 4-particle string state, with all remaining rapidities being independent. Therefore, we now need to find a way to circumvent the tedious string summation.

2.1.3 Eigenmode decomposition and Green's function

Yudson [94] developed a strategy by which the string summation in the eigenmode decomposition can be completely circumvented. Instead of working with very specific, complex string arrangements, his idea was to modify the eigenstates $|\lambda\rangle$ and allow for arbitrary complex rapidities, such that in a well-tailored contour integral we obtain a simpler representation of the identity

$$|\psi\rangle = \sum_{\text{strings}} \int d\lambda |\lambda\rangle \langle \lambda | \psi \rangle = \int_{\Gamma} d\lambda |\lambda\rangle \langle \lambda | \psi \rangle. \quad (2.9)$$

2 Theoretical description of superatom scattering

Here, we follow the notation of the original publication where the auxiliary state $|\lambda\rangle$ is distinguished from the eigenstate $|\lambda\rangle$ by a round bracket. Let us now outline the key ideas behind this simplified representation; for a full proof we refer to the original publication.

The auxiliary state reads as

$$|\lambda\rangle = \frac{\sqrt{n!}}{(2\pi)^{N/2}} \int d^n y \Theta(y_1 \geq \dots \geq y_n) \prod_{j=1}^n f(y_j, \lambda_j) e^{i\lambda_j y_j} r^\dagger(y_j, \lambda_j) |0\rangle, \quad (2.10)$$

where the Heaviside function Θ is understood to be 1, whenever the condition in the argument is fulfilled. The contour $\Gamma = \gamma_1 \otimes \dots \otimes \gamma_n$ has to be tailored to the wavefunction $|\psi\rangle$. However, it is enough to understand how to pick Γ for the position space basis state

$$|x_1, \dots, x_n\rangle = b^\dagger(x_1) \dots b^\dagger(x_n) |0\rangle,$$

where we sorted the positions as $x_1 \geq \dots \geq x_k > 0 > x_{k+1} \geq \dots \geq x_n$. Then, any curves γ_j that fulfil $\text{Re} \gamma_j(\pm\infty) = \pm\infty$ and the inequalities

$$\text{Im}(\gamma_{j+1}) - \text{Im}(\gamma_j) > \kappa \quad \text{Im}(\gamma_{j \leq k}) < \kappa/2 \quad \text{Im}(\gamma_{j > k}) > \kappa/2,$$

yield Yudson's eigenmode decomposition (2.9).

We now obtained a sufficiently simple way to calculate the time evolution of photonic states in our chiral system. Therefore we should now try to solve scattering problems with the presented method. Luckily for us Yudson's original article [94] also provides one central quantity for these kind of problems: the Green's function. As we have strict chirality it makes sense to start with photons all in front of the superatom and ask for their respective distribution after the

scattering process, that is, we want to find

$$G(y, x) = \lim_{t \rightarrow \infty} \langle y_1, \dots, y_n | e^{-iHt} | x_1, \dots, x_n \rangle,$$

with $x_j < 0, y_j > 0$. With the contour integral from above, Yudson then showed that the Green's function in the $y_n < \dots < y_1$ sector reads as

$$\begin{aligned} G(y, x) &= \sum_{\sigma \in S'_n} \int_{\Gamma} \frac{d^n \lambda}{(2\pi)^n} \prod_{j=1}^n \frac{\lambda_j - i\kappa/2}{\lambda_j + i\kappa/2} e^{i\lambda_j(y_{\sigma(j)} - x_j)} \\ &= \sum_{\sigma \in S'_n} \prod_{j=1}^n (\delta(x_j - y_{\sigma(j)}) - \kappa \Theta(x_j - y_{\sigma(j)})) e^{-\kappa(x_j - y_{\sigma(j)})/2}, \end{aligned} \quad (2.11)$$

where the permutations are restricted to $\sigma(j) \geq j - 1$. In the author's master thesis [108] we proofed that we can circumvent the summation over different permutations and the Green's function may be further simplified to

$$G(y, x) = \lim_{x_{n+1} \rightarrow -\infty} \prod_{j=1}^n \partial_{\alpha_j} e^{-\kappa \alpha_j} \Theta(x_j + \alpha_j - y_j) \Theta(y_j + \alpha_j - x_{j+1}) e^{-\kappa(x_j - y_j)/2} \Big|_{\alpha_j=0} \quad (2.12)$$

in the $y_1 > \dots > y_n$ sector.

Quantum optical master equation

2.2

2.2.1 Derivation

The solutions based on the Bethe Ansatz are well suited to describe the scattering of few photon Fock states. For all other initial conditions, however, we quickly run into problems. Take for example coherent states. They describe the light emitted from a laser and, consequently, are important for us. As they are an

2 Theoretical description of superatom scattering

infinite sum of Fock states, our previous technique is ill-suited for these states.

Conveniently, coherent states possess properties, with which the light field may be completely removed from the description. We will do so in this section and, through this, derive the quantum optical master equation for our chiral superatom system.

We start with the full Hamiltonian $H = H_{\text{Ph}} + H_{\text{int}}$, consisting of the free photon propagation (2.4) and the photon-superatom interaction (2.5). It yields the Heisenberg equation of the photonic annihilation operator

$$\dot{b}(k) = -ikb(k) - i\sqrt{\frac{\kappa}{2\pi}} \sum_{j=1}^N \sigma_j^- e^{-ikx_j}. \quad (2.13)$$

The formal solution to this differential equation is

$$b(k, t) = b(k)e^{-ikt} - i\sqrt{\frac{\kappa}{2\pi}} \sum_{j=1}^N \int_0^t ds \sigma_j^-(s) e^{-ik(x_j+t-s)}, \quad (2.14)$$

or equivalently, in real space,

$$b(x, t) = b(x-t) - i\frac{\sqrt{\kappa}}{2\pi} \sum_{j=1}^N \int dk \int_0^t ds \sigma_j^-(s) e^{-ik(x_j-x+t-s)}. \quad (2.15)$$

Now, let A be some arbitrary superatom operator, i.e., $[A, b(k)] = 0 = [A, b^\dagger(k)]$. Its Heisenberg equation of motion is

$$\dot{A} = \frac{i}{\hbar} [H_{\text{int}}, A] = i\sqrt{\kappa} \sum_{j=1}^N [\sigma_j^+(t), A(t)] b(x_j, t) + b^\dagger(x_j, t) [\sigma_j^-(t), A(t)]$$

$$\begin{aligned}
 &= i\sqrt{\kappa} \sum_{j=1}^N [\sigma_j^+(t), A(t)] b(x_j - t) + b^\dagger(x_j - t) [\sigma_j^-(t), A(t)] \\
 &\quad + \kappa \sum_{j>l} \left([\sigma_j^+(t), A(t)] \sigma_l^-(t - x_{jl}) - \sigma_j^+(t - x_{jl}) [\sigma_j^-(t), A(t)] \right) \\
 &\quad + \frac{\kappa}{2} \sum_{j=1}^N \left([\sigma_j^+(t), A(t)] \sigma_j^-(t) - \sigma_j^+(t) [\sigma_j^-(t), A(t)] \right). \tag{2.16}
 \end{aligned}$$

The $j > l$ summation emerges, as the k -integral from (2.15) yields $\delta(t - x_j + x_l - s) \equiv \delta(t - x_{jl} - s)$, which vanishes in the s integration for $j < l$, when we sort the atoms such that $x_1 < \dots < x_N$. The factor $1/2$ for $j = l$ was included since the delta distribution $\delta(t - s)$ acts at boundary of the integration.

We can bring the atom operators in (2.16) into a Markovian Lindblad master equation, if we neglect the retardation effects $\sigma_k^\pm(t - x_{jl}) \approx \sigma_k^\pm(t)$ due to the finite separation of the atoms. This is justified in the experimental settings we are interested in, since we already saw that the superatoms are spaced with micrometer distance, corresponding to retardation effects on the order of femtoseconds, which is too fast to be resolved by the microsecond dynamics of the light-atom interaction. With that we find

$$\begin{aligned}
 &\kappa \sum_{j>l} \left([\sigma_j^+, A] \sigma_l^- - \sigma_l^+ [\sigma_j^-, A] \right) + \frac{\kappa}{2} \sum_{j=1}^N [\sigma_j^+, A] \sigma_j^- - \sigma_j^+ [\sigma_j^-, A] \\
 &= \kappa \sum_{j>l} \left(\sigma_j^+ A \sigma_l^- + \sigma_l^+ A \sigma_j^- - A \sigma_j^+ \sigma_l^- - \sigma_l^+ \sigma_j^- A \right) \\
 &\quad + \kappa \sum_{j=1}^N \left(\sigma_j^+ A \sigma_j^- - \frac{1}{2} (\sigma_j^+ \sigma_j^- A + A \sigma_j^+ \sigma_j^-) \right) \\
 &= \kappa \sum_{j,l} \left(\sigma_j^+ A \sigma_l^- - \frac{1}{2} (\sigma_j^+ \sigma_l^- A + A \sigma_j^+ \sigma_l^-) \right) + \frac{\kappa}{2} \sum_{j>l} [\sigma_j^+ \sigma_l^- - \sigma_l^+ \sigma_j^-, A] \\
 &\equiv \kappa \mathcal{D}_{\sigma^-}^\dagger[A] + i[H_{\text{exc}}, A], \tag{2.17}
 \end{aligned}$$

2 Theoretical description of superatom scattering

where \mathcal{D}^\dagger is the adjoint Lindblad dissipator $\mathcal{D}_{\sigma^-}^\dagger[A] = \sigma^+ A \sigma^- - \{\sigma^+ \sigma^-, A\}/2$ with the collective decay operator $\sigma^- = \sum_j \sigma_j^-$ and we found the atom-atom interaction Hamiltonian $H_{\text{exc}} = i\kappa/2 \sum_{j>l} \sigma_l^+ \sigma_j^- - \sigma_j^+ \sigma_l^-$, which describes the exchange of a virtual photon between two superatoms.

It should be noted that our result in the Lindbladian form does not convey the chiral propagation of excitations in the system. However, chirality emerges as an interplay of the superatom decay and the atom-atom interaction. This may be seen if we go over to a *quantum jump trajectory* description [109, 110], where the effective Hamiltonian is given by the combination of the original Hamiltonian and the anti-commutator term of the dissipator, i.e.,

$$H_{\text{eff}} = -iH_{\text{exc}} - \frac{\kappa}{2} \sigma^+ \sigma^- = \kappa \sum_{j>l} \sigma_j^+ \sigma_l^- + \frac{\kappa}{2} \sum_j \sigma_j^+ \sigma_j^-. \quad (2.18)$$

The effective Hamiltonian clearly acts on the superatoms by destroying excitations at some early point in the atom chain and re-creating it at some later superatom, thus showing the chirality.

Next, we have to trace out the photons, which is straightforward as we consider a coherent input state $\rho = \rho_{\text{At}} \otimes |\alpha\rangle\langle\alpha|$. We take the photon operator terms in (2.16) and trace out the photonic degrees of freedom

$$\begin{aligned} & i\sqrt{\kappa} \sum_{j=1}^N \text{Tr}_{\text{Ph}} \left(([\sigma_j^+(t), A(t)] b(x_j - t) + b^\dagger(x_j - t) [\sigma_j^-(t), A(t)]) \rho \right) \\ & \approx i\sqrt{\kappa} \sum_{j=1}^N \text{Tr}_{\text{Ph}} \left([\sigma_j^+(t), A(t)] b(x_1 - t) \rho + [\sigma_j^-(t), A(t)] \rho b^\dagger(x_1 - t) \right) \\ & = i\sqrt{\kappa} \sum_{j=1}^N \text{Tr}_{\text{Ph}} \left([\alpha(t - x_1) \sigma_j^+(t) + \alpha^*(t - x_1) \sigma_m^-(t), A(t)] \rho \right) \\ & \equiv \text{Tr}_{\text{Ph}} (i[H'_{\text{drive}}(t), A(t)] \rho). \end{aligned} \quad (2.19)$$

where we again neglected retardation by approximating $x_j \approx x_1$ and defined $\alpha(t)$ as the classical field amplitude at the first atom at time t . The external light field thus provides a coherent drive of the superatoms.

We not have yet obtained equations of motion for A that only depend on superatom operators and $\rho_{\text{At}} = \text{Tr}_{\text{Ph}}(\rho)$, since we cannot pull the partial trace in (2.19) to ρ , due to the time evolution in the commutator. This problem can be circumvented however, if we consider the expectation value $\langle A \rangle = \text{Tr}(A\rho)$, where we can switch between the Heisenberg and Schrödinger picture. The time evolution of $\langle A \rangle$ thus becomes

$$\partial_t \langle A \rangle = \text{Tr}_{\text{At}} \left[-iA[H_{\text{exc}} + H_{\text{drive}}(t), \rho_{\text{At}}(t)] + \kappa A \mathcal{D}_{\sigma^-}[\rho_{\text{At}}(t)] \right]. \quad (2.20)$$

Here, the driving Hamiltonian $H_{\text{drive}}(t) = \sqrt{\kappa}\alpha(t-x)\sigma^+ + \text{h.c.}$ still depends on time since the c-number $\alpha(t)$ remains a function of time both in the Heisenberg and Schrödinger picture

Overall we find that the expectation value of an arbitrary superatom-operator follows from the master equation [101, 102] solution of the density matrix

$$\dot{\rho}_{\text{At}} = -i[H_{\text{drive}} + H_{\text{exc}}, A] + \kappa \mathcal{D}_{\sigma^-}[\rho_{\text{At}}], \quad (2.21)$$

with $\mathcal{D}_{\sigma^-}[\rho_{\text{At}}] = \sigma^- \rho_{\text{At}} \sigma^+ - \{\sigma^+ \sigma^-, \rho_{\text{At}}\}/2$. To this master equation we can manually add the Raman decay Γ and the dephasing γ_D , as we have discussed in section 1.3.5, to obtain the full master equation of our superatom model

$$\begin{aligned} \dot{\rho}_{\text{At}} = & -i[H_{\text{drive}} + H_{\text{exc}}, A] + \kappa \mathcal{D}_{\sigma^-}[\rho_{\text{At}}] \\ & + \sum_j \Gamma \mathcal{D}_{|G_j\rangle\langle W_j|}[\rho_{\text{At}}] + \sum_j \Gamma \mathcal{D}_{|G_j\rangle\langle D_j|}[\rho_{\text{At}}] + \sum_j \gamma_D \mathcal{D}_{|D_j\rangle\langle W_j|}[\rho_{\text{At}}], \end{aligned} \quad (2.22)$$

where we extended each emitter j by a dark state $|D_j\rangle$. Finally, we want to emphasize once again, that in the derivation we neglected only retardation effects,

stemming from the finite spacing of the atoms. The absence of further non-Markovian effects is a consequence of the chirality of our system.

2.2.2 Input-Output relations and photonic correlation functions

Since the superatoms occupy a region of an extent $\sim 100 \mu\text{m}$ we are justified to place all atoms at the origin $x_j \approx 0$ as an approximation. This naturally divides our system into two regions: The half-space $x < 0$, which we call the input region, as every photon from here will eventually interact with the superatoms, and the half-space $x > 0$, which we subsequently denote as output region as every photon here will leave the system without interacting with the atoms ever again.

As the photons are only subject to free propagation in both these half-spaces, all the information about the input and output fields is encoded in the field amplitudes directly in front and behind the atoms, respectively. For this we define the input field $b_{\text{in}}(t) = \lim_{\varepsilon \rightarrow 0^-} b(\varepsilon, t)$ and the output field $b_{\text{out}}(t) = \lim_{\varepsilon \rightarrow 0^+} b(\varepsilon, t)$.

The input and output field are directly related by the solution of the photonic Heisenberg equation (2.15)

$$b_{\text{out}}(t) = b_{\text{in}}(t) - i\sqrt{\kappa} \sum_{j=1}^N \sigma_j^-(t), \quad (2.23)$$

which is known as the *input-output relation* [98, 111]. It simply states, that the output of the superatom system is its input, together with the response of the atoms. With the input-output relations we can, for example, evaluate photonic correlation functions for a coherent input, if we know the time evolution of the atoms. This is readily achieved, thanks to the quantum optical master equation from the last section.

As an example consider $G^{(2)}(y, z)$, the non-normalised correlation function

to measure one photon at location y and one at z at some specific time t . It becomes, in terms of the initial coherent field amplitude $\alpha(t)$ at the position $x = 0$ of the atoms and the atom operators,

$$\begin{aligned}
 G^{(2)}(y, z) &= \langle b^\dagger(y, t)b^\dagger(z, t)b(z, t)b(y, t) \rangle \\
 &= \langle b_{\text{out}}^\dagger(t - y)b_{\text{out}}^\dagger(t - z)b_{\text{out}}(t - z)b_{\text{out}}(t - y) \rangle \\
 &= \left\langle \left(\alpha^*(t - y) - i\sqrt{\kappa} \sum \sigma_j^+(t - y) \right) \left(\alpha^*(t - z) - i\sqrt{\kappa} \sum \sigma_j^+(t - z) \right) \right. \\
 &\quad \left. \times \left(\alpha(t - z) - i\sqrt{\kappa} \sum \sigma_j^-(t - z) \right) \left(\alpha(t - y) - i\sqrt{\kappa} \sum \sigma_j^-(t - y) \right) \right\rangle,
 \end{aligned} \tag{2.24}$$

where we assumed $y > z$. The unequal-time atom operator correlation function can be determined with the *quantum regression theorem* [99, 100, 110–112]. The quantum regression theorem states, for example, that two-point correlation functions $\langle A(t_2)B(t_1) \rangle$, $t_2 > t_1$ can be calculated by first evolving ρ up to t_1 and then evolving $B\rho(t_1)$ for the remaining time $t_2 - t_1$ under the same master equation.

Mode population in the SLH formalism

2.3

The Bethe Ansatz solutions provide all the information about the outgoing light field when dealing with Fock states, but at the cost of cumbersome calculations. The chiral master equation, on the other hand, is straightforward to solve numerically, but we are limited to the study of n -point correlation functions of the output light field. In this section, we find a third description for our superatom system, which is almost as powerful as the Bethe Ansatz description but is still given by a finite-dimensional master equation. The new formulation is based on the SLH-formalism [104, 105], which we introduce below, and the restriction of

2 Theoretical description of superatom scattering

the input and output light field to a few specific temporal modes, instead of the full Fock space.

To begin, we need a change of perspective. So far, we have pictured the atoms as chiral emitters, passing photons from left to right. To be more general, we can think of our system as an instance of a chiral *quantum input-output network*. Such a network consists of individual quantum nodes that absorb and emit bosonic modes with directed and non-dispersive propagation between the nodes.

To describe the evolution of the network, we need three pieces of information about each node: the “scattering matrix” S of the node, the coupling operator L between the node and the bosonic background, and the Hamiltonian H , describing the free evolution of the node. Here S simply describes the node’s action on the bosonic background; for example, a phase shifter has $S = e^{i\phi}$. This description of the quantum network provides the name SLH-formalism, as this triple $G = (S, L, H)$ fully determines the evolution.

Given the triple $G = (S, L, H)$ for each node of the network we can construct the full master equation for the quantum network from some simple rules. Here we only need the concatenation rule $\triangleleft : G_2 \times G_1 \rightarrow G_3$ for chaining up two nodes, which is

$$(S_2, L_2, H_2) \triangleleft (S_1, L_1, H_1) = \left(S_2 S_1, L_2 + S_2 L_1, H_1 + H_2 + \frac{1}{2i} (L_2^\dagger S_2 L_1 - L_1^\dagger S_2^\dagger L_2) \right). \quad (2.25)$$

Provided the triple (S, L, H) of the full network, it then evolves according to the Hamiltonian H and Lindblad dissipator \mathcal{D}_L .

For example, a single superatom has the triple $(S = 1, L = \sqrt{\kappa}\sigma_i^-, H = 0)$, i.e., it decays with rate κ by emitting a photon but does not convey any other

dynamics. Two superatoms in a row then give

$$(1, \sqrt{\kappa}\sigma_2^-, 0) \triangleleft (1, \sqrt{\kappa}\sigma_1^-, 0) = \left(1, \sqrt{\kappa}(\sigma_1^- + \sigma_2^-), \frac{i\kappa}{2}(\sigma_1^+\sigma_2^- - \sigma_2^+\sigma_1^-)\right), \quad (2.26)$$

which perfectly reproduces our previous result (2.17) for the collective decay and exchange Hamiltonian in the two-atom case.

Now we discuss, how incoming and outgoing photons are included as SLH-nodes. This was solved by A. H. Kiilerich and K. Mølmer in their articles [106, 107]. They showed that for each considered temporal mode in the input (output) field, one has to place a virtual cavity in front (after) the superatom chain, each with a specific cavity coupling rate $L = g(t)b$ that makes the cavity transparent only to a single mode. In the following we will be content with discussing the simplified situation of a single input and a single output cavity.

First, let us consider an initial photon state $|\psi_{\text{in}}\rangle = \sum_{n=0}^{\infty} c_n (b_u^\dagger)^n |0\rangle$. Here, b_u^\dagger creates a photon in the temporal mode $u(t)$, with $u(t)$ describing the field amplitude at the superatoms $x = 0$ at time t . We then have to give the input cavity the coupling rate

$$g_u(t) = \frac{u^*(t)}{\sqrt{1 - \int_{-\infty}^t ds |u(s)|^2}}, \quad (2.27)$$

and put the cavity in the initial state $|\psi_{\text{in}}\rangle$, where b_u are now operators on the cavity Fock space. Similarly, if we want to study photons in the specific output mode $v(t)$, measuring the field amplitude directly behind the superatom chain at time t , we have to place a virtual cavity behind the superatoms with the coupling rate

$$g_v(t) = -\frac{v^*(t)}{\sqrt{\int_{-\infty}^t ds |v(s)|^2}}. \quad (2.28)$$

The asymptotic state of the output cavity then gives precisely the photon number

2 Theoretical description of superatom scattering

distribution of the photons emitted in the mode $v(t)$.

In total, given the superatom chain SLH-triple $(1, \sqrt{\kappa}\sigma^-, H_{\text{exc}})$, we can study arbitrary photon input states in mode $u(t)$ and observe output photons in mode $v(t)$ by simulating the quantum network

$$(1, g_v^*(t)b_v, 0) \triangleleft (1, \sqrt{\kappa}\sigma^-, H_{\text{exc}}) \triangleleft (1, g_u^*(t)b_u, 0), \quad (2.29)$$

with b_u (b_v) the input (output) cavity annihilation operator. This results in a master equation for the cavity-superatom system which consists of the collective decay

$$L = \sqrt{\kappa}\sigma^- + g_u^*(t)b_u + g_v^*(t)b_v \quad (2.30)$$

and the cavity-superatom exchange Hamiltonian

$$H_{\text{exc}} + \frac{i}{2}(\sqrt{\kappa}g_u(t)b_u^\dagger\sigma^- + \sqrt{\kappa}g_v^*(t)\sigma^+b_v + g_u(t)g_v^*(t)b_u^\dagger b_v - \text{h.c.}). \quad (2.31)$$

Alternatively, if we just consider a coherent input field, i.e., $|\psi_{\text{in}}\rangle = |\alpha\rangle$, we may trace out the initial photon field again. This removes the input cavity from our system, but introduces the driving Hamiltonian

$$H_{\text{drive}} = i(\alpha^*(t)L - \alpha(t)L^\dagger), \quad (2.32)$$

for the superatom chain and output cavity with $\alpha(t) = \alpha u(t)$. Notice, that without the output cavity this reproduces our previous result (2.19) after a phase rotation $\alpha(t) \mapsto i\alpha(t)$.

3

Photon correlations by superatom interaction

The ability to facilitate and control the interaction between two photons is essential for many modern applications [113, 114]. Examples include quantum communication [115], quantum metrology [116, 117], and quantum computation with photons [21, 118, 119], which always requires optical non-linearity [120, 121]. Effective photon-photon interactions emerge in many platforms, like atoms in optical cavities [122–125] or quantum emitters coupled to waveguides [126–131]. In this chapter, we study how a single superatom mediates effective photon-photon interactions, which are strong enough to provide measurable three-photon correlations [90, 132].

The discussion in this chapter follows the article [90], where the author of this thesis contributed the Bethe state analysis. This analysis reveals the string solutions, which may be interpreted as photonic bound states, to be the origin of the observed correlations. Moreover, as the bound states show a universal dependency on the photon-photon separation for sufficiently broad initial wave functions, they predict a generic form for the emerging correlation functions.

In addition to the author’s contribution, we will discuss the experimental

results and show the predictive power of the quantum optical master equation (2.21). Other than the Bethe Ansatz, the master equation can account for Raman decay Γ of the superatom and its dephasing γ_D into a dark state. With these two additional parameters, the master equation is able to almost perfectly reproduce the experimental results.

Predictions from the Bethe states

3.1

3.1.1 Few Photon scattering solutions

We first want to describe the scattering within the Bethe Ansatz. For this, we consider the scattering of a few-photon Fock state on the superatom and determine the two- and three-photon correlation functions from the scattering solutions.

We are mainly interested in the two- and three-body correlations and consequently analyse the scattering of a two- and three-photon product state $\psi_0(x_1, \dots, x_n) = \psi_{\text{in}}(x_1) \dots \psi_{\text{in}}(x_n)$. Let us start with the two-photons state, for which the outgoing wave function in the $y_1 > y_2$ sector reads as

$$\psi_{\text{out}}(y_1, y_2) = \psi_{\text{out}}(y_1)\psi_{\text{out}}(y_2) - \kappa^2 e^{-\kappa(y_1 - y_2)/2} \psi_T^2(y_1), \quad (3.1)$$

according to our Green's function (2.12). Here, ψ_{out} denotes the single-photon scattered state

$$\begin{aligned} \psi_{\text{out}}(y) &= \partial_\alpha \Big|_{\alpha=0} e^{-\kappa\alpha} \int_{-\alpha}^{\infty} dx e^{-\kappa x/2} \psi_{\text{in}}(x + y) \\ &\equiv \partial_\alpha \Big|_{\alpha=0} e^{-\kappa\alpha} \psi_T(y, \alpha) \\ &= \psi_{\text{in}}(y) - \kappa \psi_T(y, 0), \end{aligned} \quad (3.2)$$

and ψ_T is the convolution of the single-photon input state with the exponential kernel.

The two-photon scattering result has a straightforward interpretation: When two photons interact with a single superatom, they are either independently scattered, resulting in a product wave function $\psi_{\text{out}}(y_1)\psi_{\text{out}}(y_2)$, or stimulated emission occurs, leading to strong spatial correlation between both photons. This is indicated by the exponential suppression $\exp(-\kappa(y_1 - y_2)/2)$ in the relative distance between both photons. To underline the spatial proximity of both photons, we will call the second term a *two-photon bound state*

$$\psi_B(y_1, y_2) = e^{-\kappa(y_1 - y_2)} \psi_T^2(y_1) \quad (3.3)$$

for $y_1 > y_2$.

The two-photon result (3.1) is only valid in the $y_1 > y_2$ sector. Hence we symmetrise the result by replacing $y_1 \mapsto \max(y_1, y_2) = R + |r|/2$ and $y_2 \mapsto \min(y_1, y_2) = R - |r|/2$, where $R = (y_1 + y_2)/2$ is the centre of mass coordinate and $r = y_1 - y_2$ the relative distance. Therefore, the symmetrised bound state becomes $\psi_B(y_1, y_2) = e^{-\kappa|r|/2} \psi_T^2(R + |r|/2)$.

If the initial wave function is broad compared to κ , we may drop the r dependency in ψ_T . The photon separation thus comes mostly from the exponential prefactor, while the original wave function only impacts the centre of mass shape. We therefore expect and will see that the correlation functions have a quite universal form, which comes from the $e^{-\kappa|r|/2}$ dependency.

Let us now discuss the three-photon result. Here the scattered wave function becomes

$$\begin{aligned} \psi_{\text{out}}(y_1, y_2, y_3) &= \psi_{\text{out}}(y_1)\psi_{\text{out}}(y_2)\psi_{\text{out}}(y_3) \\ &\quad - \kappa^2 \left(\psi_{\text{out}}(y_1)\psi_B(y_2, y_3) + \psi_{\text{out}}(y_2)\psi_B(y_1, y_3) + \psi_{\text{out}}(y_3)\psi_B(y_1, y_2) \right) \\ &\quad - 2\kappa^3 e^{-\kappa(y_1 - y_3)/2} \psi_T(y_2)\psi_T^2(y_1). \end{aligned} \quad (3.4)$$

3 Photon correlations by superatom interaction

The three-photon result again consists of the scattering of three independent photons and the three possibilities for pairing two photons into bound states with one free photon remaining. Additionally, we find a term with exponential prefactor $\exp(-\kappa(y_1 - y_3)/2)$. This term also enforces that the second photon cannot be separated from the other two photons, as the result (3.4) is only valid in the sector $y_1 > y_2 > y_3$. Therefore we should interpret the last line of (3.4) as a three-photon bound state. This becomes more evident with the exponent in its symmetrised form, which reads as

$$\max(y_1, y_2, y_3) - \min(y_1, y_2, y_3) = (|y_1 - y_2| + |y_2 - y_3| + |y_3 - y_1|)/2. \quad (3.5)$$

3.1.2 Two- and three-photon correlations

Before we analyse the correlation functions for the scattering solutions, we should first discuss the relevant parameter regime. In the article [90] we studied coherent light scattered on a single superatom. We excited the superatom by a Tukey shaped pulse¹ of about $6 \mu\text{s}$ with negligible ramp up and down times. By comparing the observed Rabi oscillations of the superatom to the predictions from the master equation (2.21), as indicated by the figure to the right, we find that the superatoms is well-described by the parameters $\kappa = 0.55 \mu\text{s}^{-1}$, $\Gamma = 0.14 \mu\text{s}^{-1}$ and $\gamma_D = 1.49 \mu\text{s}^{-1}$.

The superatom, at sufficiently strong driving strength, shows damped Rabi oscillations [103] and typically reaches its steady state after a few Rabi cycles, which is accelerated by the dissipative impact of Γ and γ_D . This was the case even for the largest experimen-

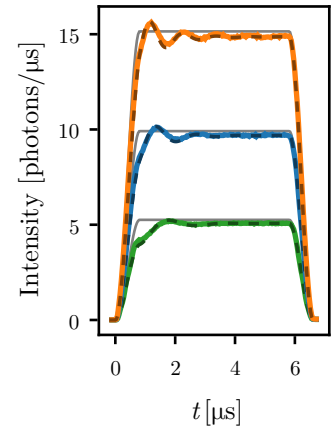


Figure 3.1

Photon intensity after scattering probe beams of different intensity (grey lines). Dashed lines show fits from the master equation.

¹A Tukey shaped pulse consists of a cosine-ramp up and down, with flat plateau between

tal photon rate of $|\alpha|^2 = 15.6$ photons/ μs , as shown in figure 3.1. Therefore, as we may neglect ramp up effects, we will be justified to study the scattering of resonant plane waves, which we approximate as

$$\psi_{\text{in}}(x) = \begin{cases} \frac{1}{\sqrt{w}} & x \in \{-w/2, w/2\} \\ 0 & \text{otherwise} \end{cases} \quad (3.6)$$

with $w \rightarrow \infty$. We then find $-\psi_{\text{out}}(y) = \psi_{\text{in}}(y) = \kappa\psi_T(y)/2$. Thus, at the centre $y_i \approx 0$ of the wave function we find

$$w\psi_{\text{out}}(y_1, y_2) \approx 1 - 4e^{-\kappa|y_1 - y_2|/2}, \quad (3.7)$$

$$\begin{aligned} w^{3/2}\psi_{\text{out}}(y_1, y_2, y_3) \approx & 1 - 4\left(e^{-\kappa|y_1 - y_2|/2} + e^{-\kappa|y_2 - y_3|/2} + e^{-\kappa|y_1 - y_3|/2}\right) \\ & + 16e^{-\kappa(|y_1 - y_2| + |y_2 - y_3| + |y_3 - y_1|)/4}. \end{aligned} \quad (3.8)$$

These results allow us to determine the two- and three-body correlation functions, for the scattering of a weak probe beam on a single superatom. For this assume the initial state of light is a coherent plane wave $|\alpha\rangle$ with the coherent amplitude $\alpha \ll 1$, so that we are justified to only consider the lowest, most relevant contributions in α . Then, the n -point expectation values becomes

$$\langle b^\dagger(y_1) \dots b^\dagger(y_n) b(y_n) \dots b(y_1) \rangle \approx \frac{|\alpha|^{2n}}{w^n} |\psi_{\text{out}}(y_1, \dots, y_n)|^2. \quad (3.9)$$

For the plane wave we subsequently find the two-photon correlation function

$$\begin{aligned} g^{(2)}(y_1, y_2) &= \frac{\langle b^\dagger(y_1) b^\dagger(y_2) b(y_2) b(y_1) \rangle}{\langle b^\dagger(y_1) b(y_1) \rangle \langle b^\dagger(y_2) b(y_2) \rangle} \\ &= |\psi_{\text{out}}(y_1, y_2)|^2 \end{aligned} \quad (3.10)$$

3 Photon correlations by superatom interaction

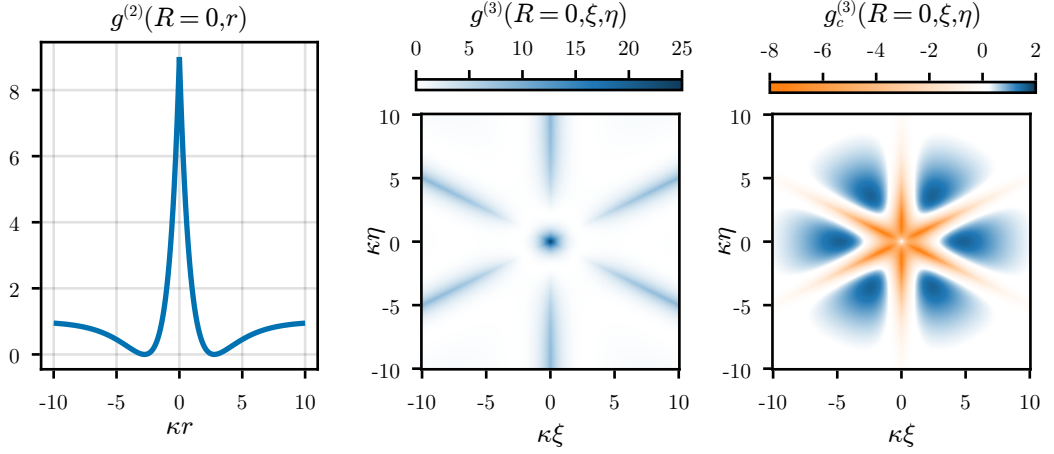


Figure 3.2

Two-point (left) and three-point (middle) correlation functions for a flat input mode from the Bethe Ansatz. The rightmost panel shows connected three-point correlation function, i.e., the three-body correlations after removing the two-photon contributions.

and the three-point correlation function

$$\begin{aligned}
 g^{(3)}(y_1, y_2, y_3) &= \frac{\langle b^\dagger(y_1)b^\dagger(y_2)b^\dagger(y_3)b(y_3)b(y_2)b(y_1) \rangle}{\langle b^\dagger(y_1)b(y_1) \rangle \langle b^\dagger(y_2)b(y_2) \rangle \langle b^\dagger(y_3)b(y_3) \rangle} \\
 &= |\psi_{\text{out}}(y_1, y_2, y_3)|^2,
 \end{aligned} \tag{3.11}$$

i.e., they are simply given by the respective outgoing wave functions.

For the visualisation of the three-body correlation function we use Jacobi coordinates

$$R = \frac{y_1 + y_2 + y_3}{3}, \tag{3.12a}$$

$$\xi = y_1 - y_2, \tag{3.12b}$$

$$\eta = \frac{y_1 + y_2}{2} - y_3, \tag{3.12c}$$

which generalise centre of mass and relative coordinates to higher dimension.

The two- and three-photon correlation functions in these coordinates are depicted in figure 3.2. First, the two-photon correlation functions shows strong bunching coming from the formation of the sharply located two-photon bound state. Similarly the three-photon correlation function possesses a substantial bunching peak right at its centre, together with three lines of noticeable correlations, which correspond to the positions where two photons are close to each other, while the third photon is at some different location.

Especially this last contribution is purely due to the two-photon bound states. In order get proper information about the three-photon correlations we should subtract the two-photon bound state contribution from $g^{(3)}$. This then gives raise to the *connected three-body correlation function*

$$g_c^{(3)}(y_1, y_2, y_3) = g^{(3)}(y_1, y_2, y_3) - \sum_{j < l} g^{(2)}(y_j, y_l) + 2, \quad (3.13)$$

where the +2 normalises $g_c^{(3)}$ to zero at $\xi, \eta \rightarrow \infty$. The connected $g^{(3)}$ function reveals a ring like structure of positive correlations around the centre $\xi \approx 0 \approx \eta$, originating from the three-photon bound state.

The Bethe Ansatz revealed how the superatom mediates effective photon-photon interactions that lead to the formation of photonic bound states. These bound states then result in strong correlations in the n -photon correlation functions. The bound state interpretation should not be taken too seriously, as these states are neither orthogonal to the states which we interpreted as independent photon scattering, nor lead to a lowering of the energy. They simply describe the bunched spatial photon distribution. Furthermore, the approach from above is clearly only valid for very weak coherent input states and without any noise on the superatom. Therefore, we should now approach the problem of the photon correlations from the master equation (2.21), with which we can study a broader set of parameters. This analysis was originally performed by J. Kumlin, co-author of [90].

Master equation solutions and experimental results

3.2

In the absence of dephasing, the predicted correlations (figure 3.2) are substantial. However, the experimental results reveal that we need to take noise into account, as discussed in section 1.4, especially since the dephasing γ_D turns out to be the dominant decay mechanism of the superatom.

For this, consider the measurement of the emitted intensity, which directly reveals the Rabi oscillations of the superatom through the input-output relations (2.23): $b_{\text{out}}(t) = b_{\text{in}}(t) - i\sqrt{\kappa}\sigma^-(t)$. The fit of the master equation to the experimental results, displayed in figure 3.1, results in a coupling rate of $\kappa \approx 0.55 \mu\text{s}^{-1}$, and dephasing rates of $\Gamma \approx 0.14 \mu\text{s}^{-1}$, $\gamma_D \approx 1.49 \mu\text{s}^{-1}$.

With these parameters, the master equation (2.21) provides a more realistic estimation of the n -photon correlations. We then obtain the connected three-body correlation functions depicted in the top row of figure 3.3. For weak α , we find a qualitative agreement with the previous Bethe results from figure 3.2 as we see a similar hexagonal bunching ring around the anti-bunched centre at $\xi \approx 0 \approx \eta$, however, modified due to the dissipation Γ and dephasing γ_D . With increasing α , the relevant time scales become faster, but we also introduce additional bunching and anti-bunching rings. These additional bunching regions must come from higher photon contributions since we already showed that the noiseless Bethe solutions in the three-photon problem could only yield one anti-bunching to bunching transition.

Compared to the Bethe solutions, the magnitude of the correlations is reduced by a factor of 10^{-2} to 10^{-3} due to the noise. Yet, $g_c^{(3)}$ can still be resolved experimentally, as shown in the bottom row of figure 3.3. Remarkably, the qualitative agreement between the master equation solution and the experimental data is relatively high, especially at high photon numbers. It should be no surprise

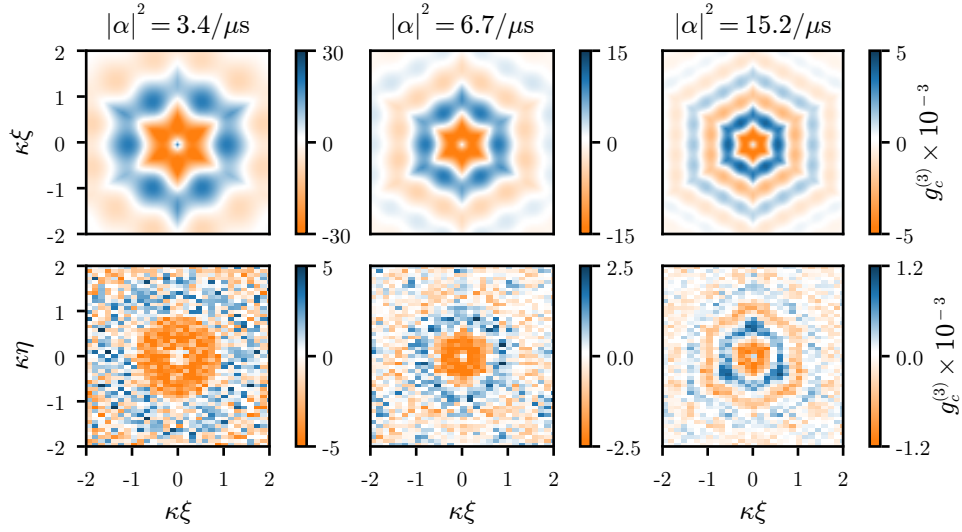


Figure 3.3

Connected three-point correlation functions at different driving strength α . The top row depicts the numerical results obtained from the master equation, the bottom row shows the respective experimental results.

that our master equation, which essentially describes damped Rabi oscillations, could capture the experimentally measured intensity, see figure 3.1. A more convincing verification of our superatom model lies in the fact that we can use the same set of parameters to predict the correct behaviour of the n -photon correlation functions.

4

Photon number statistics in binned modes

The previous chapter showed that the superatom-mediated photon-photon interaction leads to strong temporal correlations, even on a multi-photon level. Temporal correlations are necessarily a multi-mode effect, as any product wave function possesses constant n -body correlation functions. Through the lens of the Bethe Ansatz, we saw that the temporal correlations follow from a superposition of the independent scattering states and the photonic bound states. However, while we know the constituents of the multi-mode wave function, we have no information about the occupation of these particular states. Therefore we will now, in some regard, ask the complementary question to what we did in the last chapter and investigate the photon number occupation of a single output mode in this chapter.

In particular, we will see that a single superatom, under coherent drive, populates specific modes with a non-classical photon number distribution as indicated by a negative Wigner function. Non-classical states of light are essential resources in many experimental settings, such as quantum metrology [133–135], the violation of Bell inequalities using entangled photon pairs [136–138], or in quan-

tum cryptography [139–142] and information processing [143, 144]. Meanwhile, the generation of highly non-classical states of light is not straightforward. For example, squeezed states [145] are limited to a few decibels [146, 147], state-of-the-art NOON states [148] are still limited to the few-photon regime [149], and generating non-classical light often requires heralding or post-selection [150, 151].

From an exact limit for short temporal modes, we find that the emerging non-classical states in our system highly resemble photon-added coherent states. We explain this by the emission of a previously absorbed photon from the superatoms. Increasing the number of superatoms, however, does not lead to a linear scaling of this effect, and, in certain limits, the non-classicality vanishes entirely, and we will obtain the input photon state again. This surprising result follows from the behaviour of the photon bound states for a plane wave input. In these particular cases, the scattering phase on each Bethe state vanishes after scattering on a second superatom. Therefore a superatom chain of an even number of atoms will approximatively emit the original input state.

Based on these results, we will then discuss experimental applications of the obtainable non-classical states. We will see that the non-classicality is directly observable under homodyne detection. Nevertheless, even without such a detection scheme, the non-classicality is useful, as, in linear-optics experiments, there is no mode mixing, and we can work directly with the multi-mode output. With this, we discuss an application in quantum metrology. This chapter is based on yet unpublished work of the author of this manuscript.

Photon number statistics and phase space distributions

4.1

A classical emitter emitting at a constant rate will produce light with a Poissonian number distribution in a fixed time frame. In a quantum mechanical

4.1 Photon number statistics and phase space distributions

language, these are precisely the coherent states. For this reason, one might classify coherent states as classical states [152, 153]. At this point, “classical state” should simply be considered a figure of speech, and we give a proper definition below. Furthermore, any statistical mixture of classical states should be considered classical as well, as these states can emerge from a collection of the aforementioned classical emitters. For example, thermal states can be considered a Gaussian mixture of coherent states.

This discussion naturally leads to the definition of *classical states*: these are the states within the convex hull of the set of coherent states [154–156]

$$\mathcal{M}_{\text{cl}} = \text{conv}\{|\alpha\rangle\langle\alpha|\} \equiv \left\{ \int d^2\alpha P(\alpha) |\alpha\rangle\langle\alpha| \mid P \geq 0, \int d^2\alpha P(\alpha) = 1 \right\}. \quad (4.1)$$

Due to the simple geometry of classical states, we can directly quantify how much a particular state ρ differs from a classical state by measuring its *non-classical distance* δ to \mathcal{M}_{cl}

$$\delta[\rho] = \inf_{\rho_{\text{cl}} \in \mathcal{M}_{\text{cl}}} \|\rho - \rho_{\text{cl}}\|_1, \quad (4.2)$$

where $\|A\|_1 = \text{Tr}(|A|)$ denotes the trace norm with $|A| = \sqrt{A^\dagger A}$. Now, while the definitions from this paragraph are quite natural, they are impractical at best, as the non-classical distance can rarely be calculated and we have to be content with weak inequalities as, for example,

$$\delta[\rho] \geq \frac{1}{\sqrt{\text{Tr}(\rho^2)}} \left(\text{Tr}(\rho^2) - \sup_{\alpha} \langle \alpha | \rho | \alpha \rangle \right). \quad (4.3)$$

Therefore, we should quantify the non-classicality of a state ρ either by some heuristic or by a weaker yet more practical condition. One particular useful heuristic is the *entanglement potential* [157]

$$\text{EP}[\rho] \equiv \log_2 \|(\rho_{\text{BS}})^{T_A}\|_1, \quad (4.4)$$

4 Photon number statistics in binned modes

where $\rho_{\text{BS}} = U_{\text{BS}}(\rho \otimes |0\rangle\langle 0|)U_{\text{BS}}^\dagger$ with U_{BS} the unitary transformation of a 50:50 beam splitter and ρ^{TA} denotes the partial transpose with respect to the first subsystem. The entanglement potential effectively measures the amount of entanglement we can generate from ρ by using linear optical devices. For example, it would vanish for a coherent state and $\text{EP}[|1\rangle\langle 1|] = 1$.

An alternative approach is to study the phase space distribution of ρ . Consider the integral representation of the classical states in (4.1). If we forgo the $P \geq 0$ condition for classical states, we can express any state as a combination of coherent states, which is the *Glauber-Sudarshan P-representation* [158, 159]

$$\rho = \int d^2\alpha P(\alpha)|\alpha\rangle\langle\alpha|. \quad (4.5)$$

Thus, through the sign of the P -representation, we can directly distinguish classical from non-classical states.

However, the P -representation of many important pure states, like coherent states and Fock states, typically involve distributions [160], which makes the P -representation itself impractical for numerical analysis. Closely related to the P -representation is the Wigner-representation, which follows from the P -representation by a Weierstrass transformation

$$W(\alpha) = \frac{2}{\pi} \int d^2\beta P(\beta)e^{-2|\alpha-\beta|^2}. \quad (4.6)$$

A simple corollary follows: the P -representation is negative whenever W is negative¹, i.e., the Wigner negativity indicates non-classicality. The Wigner function directly follows from the density matrix ρ [111, 160]

$$W(\alpha) = \frac{1}{\pi^2} \int d^2\lambda \text{Tr} \left(\rho e^{\lambda(a^\dagger - \alpha^*) - \lambda^*(a - \alpha)} \right), \quad (4.7)$$

¹The converse is not true. The Wigner negativity therefore provides a stronger measure of non-classicality. As an example, and an analogy to the Gottesman-Knill theorem [161, 162], Wigner positive states possess an efficient description via classical resources [163].

which should be considered the critical advantage of the Wigner function over P . Additionally, W is a regular function and can be efficiently computed numerically [164]. Therefore, we will utilise the *integrated Wigner negativity*

$$W_{\text{neg}}[\rho] \equiv \int d^2\alpha \min(W(\alpha), 0) \quad (4.8)$$

as another measure of non-classicality.

Single superatom

4.2

4.2.1 Setup and Wigner functions

We now study the photon-number occupation of a single mode in the output field after scattering on a single superatom, with the SLH-formalism discussed in chapter 2. We start with a noise-free superatom ($\Gamma = 0 = \gamma_D$) in the ground state. Then, at time $t = 0$, a coherent driving field of constant amplitude α switches on and starts to excite the superatom. To make the input and output modes comparable, we study the occupation of a piecewise constant output mode

$$v(t) = \begin{cases} \frac{1}{\sqrt{w}} & t \in (t_0, t_0 + w) \\ 0 & \text{otherwise} \end{cases}. \quad (4.9)$$

We will analyse the number statistics of the photons in mode v , i.e., $\rho_v = \text{Tr}_{\text{atom}}[\rho]$, with the measures discussed in the last section.

Let us first discuss the dynamics of the superatom, as depicted in figure 4.1 (a). At $t = 0$, the superatom starts to undergo damped Rabi oscillations and shows two peaks in the bright state population before settling into a steady state, where the coherent drive and spontaneous decay cancel. This implies that we can identify three parameter regions for the binning interval $(t_0, t_0 + w)$. Firstly, we

4 Photon number statistics in binned modes

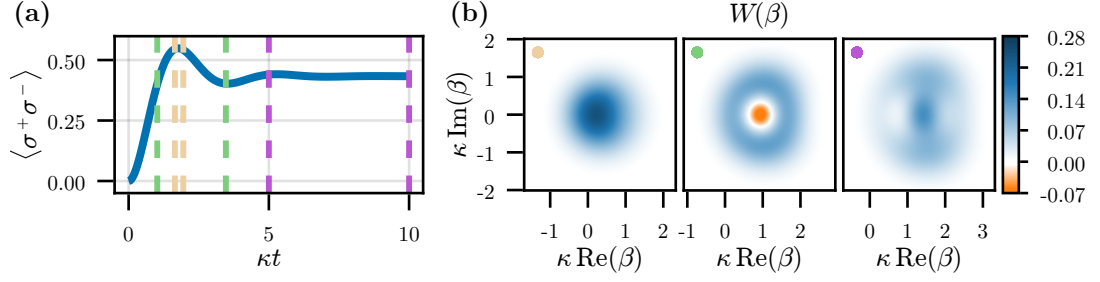


Figure 4.1

(a) Bright state population of the superatom for $\alpha = 0.9\sqrt{\kappa}$ and $\Gamma = 0 = \gamma_D$. The vertical lines indicate the binning interval $(t_0, t_0 + w)$ for the different Wigner functions studied in (b). (b) Wigner functions of the mode population for $v(t)$ with different binning choices. For short time bins (left) ρ_v mostly resembles the coherent state $|\sqrt{w}\alpha\rangle$ and for large bins $\kappa w \gg 1$ (right) ρ_v becomes non-trivial but remains positive. Only for intermediate widths w (middle) do we find a negative Wigner function.

have the short binning limit $\kappa w \ll 1$, for which we expect that the light in mode v is close to the vacuum, independent of t_0 , as the chance to find a single photon should scale as $w|\alpha|^2$ in this limit. Secondly, we have the opposite limit $\kappa w \gg 1$, for which we approximatively expect a translation invariance in t_0 , since we mainly resolve the steady state emission of the superatom for large bins w . Lastly, we have intermediate sized bins $\kappa w \approx 1$. Here we expect the precise choice of t_0 to matter significantly, as long as we are not in the steady state.

In the short bin limit $w \rightarrow 0$ we find ρ_v by the input-output relations

$$\begin{aligned} \mathcal{D}^\dagger(\sqrt{w}\alpha)\rho_v\mathcal{D}(\sqrt{w}\alpha) = & \\ & \left[|0\rangle\langle 0| + \sqrt{\kappa w}[\langle\sigma^-(t_0)\rangle|1\rangle\langle 0| + \langle\sigma^+(t_0)\rangle|0\rangle\langle 1|] \right. \\ & \left. + \kappa w\langle\sigma^+(t_0)\sigma^-(t_0)\rangle(|1\rangle\langle 1| - |0\rangle\langle 0|) \right]. \end{aligned} \quad (4.10)$$

We perform the derivation of this result in the appendix 4.A of this chapter. Here \mathcal{D} denotes the displacement operator. Thus, ρ_v becomes a mixture of

photon-added coherent states $(c_0 + c_1 a^\dagger)|\sqrt{w}\alpha\rangle$ in the limit $w \rightarrow 0$.

With the exact result (4.10), we can identify the underlying processes that create ρ_v and develop a strategy to optimise ρ_v for non-classicality. We already saw, by the input-output relations, that the outgoing light field is a superposition of the input field and the superatom response. This explains that ρ_v mainly resembles the coherent state $|\sqrt{w}\alpha\rangle$, which is the binned input field. Additionally, for $w \rightarrow 0$, there is a small chance that the superatom emits a previously absorbed photon within the time bin, which results in the photon-added contribution. This is verified by the fact that this term scales with the bright state population $\langle\sigma^+(t_0)\sigma^-(t_0)\rangle$ and we will find further numerical evidence for this later.

A single-photon Fock state is an important example of a non-classical state. This remains true for photon-added coherent states, like (4.10), since the displacement only results in a translation in the P -representation and the Wigner function. Ergo, we should increase the chance for a photon-emission event in order to optimise the non-classicality.

We achieve this for intermediate-sized bins $\kappa w \approx 1$ by choosing (t_0, t_0+w) such that the bin lies around the first Rabi peak of the superatom as this is the time when the superatom has the highest chance to emit a photon. This is verified numerically by optimising the binning parameters (t_0, w) for the integrated Wigner negativity, which results in the green binning window indicated in figure 4.1 (a) and the Wigner function in the middle of figure 4.1 (b). It shows a well-defined non-classical region.

We may try to increase the binning size $\kappa w \gg 1$ to increase the chance for the emission of additional photons by the superatom and thus create larger Wigner negativities. Yet, for large w , the bin no longer just includes times of high emission and the relative rate of photons emitted per unit time decreases. In total, this results in a negative trade-off for us and the overall Wigner-negativity decreases and vanishes for $\kappa w \gg 1$. This is indicated by the violet binning window in figure 4.1, which results in the rightmost Wigner function. While it

4 Photon number statistics in binned modes

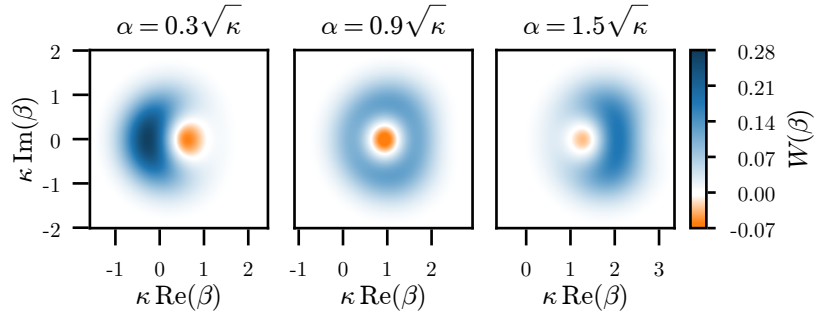


Figure 4.2

Wigner functions for different α and at $\Gamma = 0 = \gamma_D$. The binning interval $(t_0, t_0 + w)$ of each Wigner function was optimised for the integrated Wigner-negativity.

does not resemble a coherent state, and it will likely be non-classical in some of the measures of non-classicality from above, this state lost all Wigner-negativity, and we, therefore, consider it as more classical as its intermediate bin width $\kappa w \approx 1$ counterpart.

In the examples in figure 4.1, we chose $\alpha = 0.9\sqrt{\kappa}$ simply for aesthetic reasons. Our arguments from the last paragraphs hold for all values of α , but the dependency of the dominant timescale (the Rabi oscillations) on α results in a non-trivial behaviour of the Wigner function on α . In fact, we can only create Wigner-negative states up to some threshold value around $\alpha \approx 1.5\sqrt{\kappa}$, as indicated by figure 4.2.

For the explanation, consider increasing α and thus also the Rabi-frequency $\sqrt{\kappa}\alpha$. As we already argued, we should bin around the first Rabi peak to obtain the most non-classical output states. For large α , however, this means that $w \propto 1/\sqrt{\kappa}\alpha$ and we approach the short bin limit, where we already saw in the exact result (4.10) that then ρ_v mainly resembles a coherent, i.e., classical state. Numerically we find that the Wigner negativity vanishes at about $\alpha = 1.6\sqrt{\kappa}$, slightly above the last example in figure 4.2. On the other hand, if we choose α too small, we do not drive the superatom strong enough, and the chance for the

emission of a photon becomes small. Thus, there is an optimal driving strength, which we numerically find to be $\alpha \approx 0.5\sqrt{\kappa}$.

Lastly, we want to give further numerical evidence that our picture of the superatom emitting an additional photon onto the coherent background is accurate. For this we numerically optimise ρ_v for its integrated Wigner-negativity at different α and fit a mixture of two-photon added coherent states to ρ_v , i.e., we use the Ansatz

$$\rho_v = \sum_{j=1}^3 \lambda_j \mathcal{D}(\sqrt{w}\alpha) |\psi_j\rangle \langle \psi_j| \mathcal{D}^\dagger(\sqrt{w}\alpha), \quad (4.11a)$$

$$|\psi_j\rangle = c_0^{(j)} |0\rangle + c_1^{(j)} |1\rangle + c_2^{(j)} |2\rangle. \quad (4.11b)$$

Here we set the probability amplitudes λ_j directly to the numerically determined three most dominant eigenvalues of ρ_v and we constrain the coefficients $c_l^{(j)}$ of $|\psi_j\rangle$ by requiring orthonormalisation of $\{|\psi_j\rangle\}$. In total this results in only 3 free fit parameters of the Ansatz for the description of ρ_v . We used a two-photon added coherent state as an Ansatz since for $\kappa w \approx 1$ we need to account for the small chance that the superatom emits one photon and then absorbs and re-emits a second within the time bin $(t_0, t_0 + w_0)$.

For $\alpha \in \{0.1, 0.2, \dots, 1.5\}\sqrt{\kappa}$ we overall find that the three most dominant eigenvalues of ρ_v make up $> 99.99\%$ of the total probability. Additionally the fidelity of the fits lie above 98.8% . This is a strong numerical indicator that ρ_v is indeed created by photon-emission from the superatom on top of a coherent background.

4.2.2 Comparing metrics of non-classicality

In the last section we used the integrated Wigner-negativity (4.8) to measure the non-classicality of a given state ρ_v . Yet, many non-classical states possess a purely positive Wigner functions, for example squeezed states [145]. Thus

4 Photon number statistics in binned modes

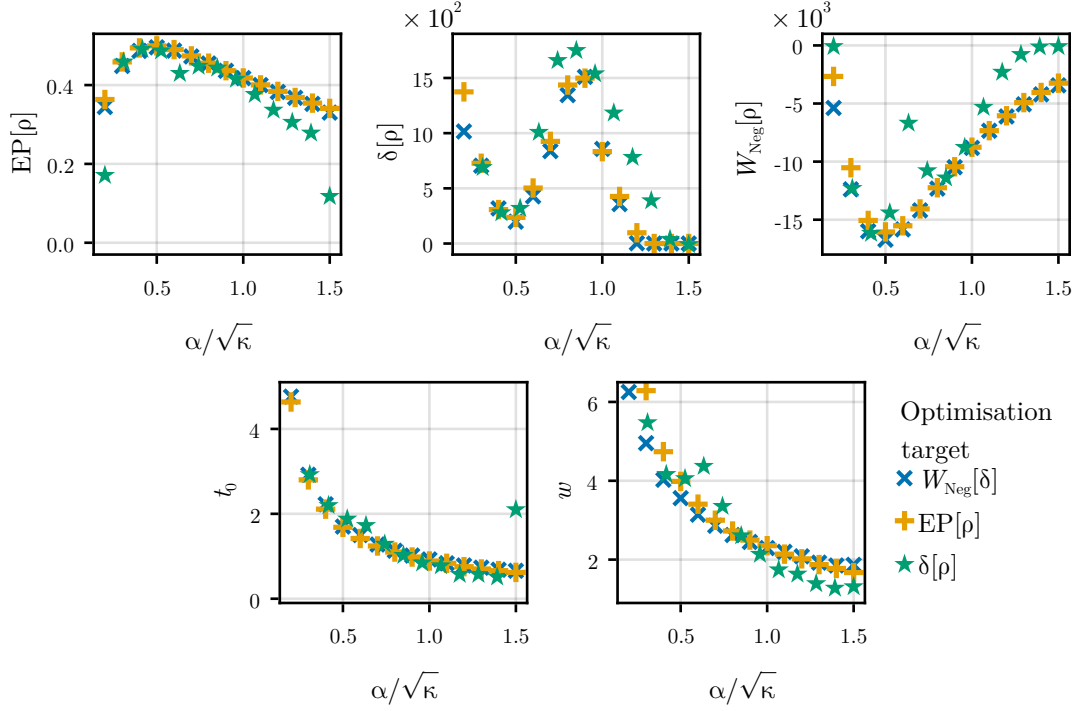


Figure 4.3

Entanglement potential $EP[\rho]$, lower bound of the non-classical distance $\delta[\rho]$, the integrated Wigner-negativity $W_{\text{Neg}}[\rho]$, and the binning interval $(t_0, t_0 + w)$ for different α when optimising t_0 and w for the different metrics of non-classicality. $\Gamma = 0 = \gamma_D$.

we should ask ourselves whether any of the other measures of non-classicality we introduced, namely the lower bound of the non-classical distance (4.3) and the entanglement potential (4.4), provide different results.

This question is answered in figure 4.3. Here we optimise t_0 and w for the three measures of non-classicality, $EP[\rho]$, $\delta[\rho]$, and $W_{\text{Neg}}[\rho]$, and then compare these metrics and the resulting binning parameters. We find that there are only insignificant differences whether we optimise for $EP[\rho]$ or $W_{\text{Neg}}[\rho]$ and these two quantities seem to be well-correlated overall. Optimising for the lower bound (4.3) on $\delta[\rho]$, however, results in slightly different values for $W_{\text{Neg}}[\rho]$ and

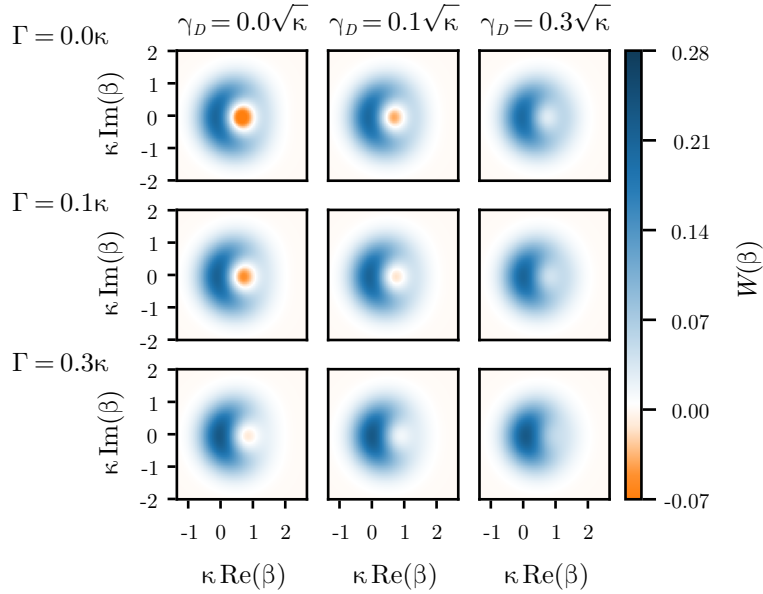


Figure 4.4

Wigner function for different γ_D and Γ at $\alpha = 0.5\sqrt{\kappa}$. Here we use the same binning interval $(t_0, t_0 + w)$ for all examples, which was chosen to maximise $W_{\text{Neg}}[\rho]$ at $\Gamma = 0 = \gamma_D$.

$\text{EP}[\rho]$, especially in regions in which $\delta[\rho]$ is small. Yet, independent of which metric we choose for the optimisation, we overall find quite similar binning intervals $(t_0, t_0 + w)$. Therefore, our previous analysis based on W_{Neg} was well-justified and we may continue by only considering the integrated Wigner-negativity.

4.2.3 Sensitivity on dephasing and dissipation

So far, we have considered a perfect noiseless superatom. However, we already saw that the dephasing γ_D into the dark states and the Raman decay Γ are crucial for an accurate description of the superatom. In this section we want to briefly discuss how the outgoing light state ρ_v is affected by both of these effects.

Figure 4.4 shows the dependency of the Wigner function on the dephasing γ_D

and dissipation Γ . Overall we find there is little qualitative difference between both noise sources, only the effects of the dephasing seem to be a little stronger than the effects of the dissipation for similar γ_D and Γ . We explain this with our previous findings for the dynamics of ρ_v . We saw that the non-classicality in ρ_v comes from the emission of a photon from the excited Rydberg atom. Both decay mechanisms remove this energy quantum from the system and thus act similarly on ρ_v . However, the impact of γ_D is slightly larger since, after the decay into the dark state, the superatom remains blockaded, while after the Raman decay there is still a small chance that the superatom absorbs and re-emits a second photon within the time-bin $(t_0, t_0 + w)$. Even though this photon is absorbed and emitted within $(t_0, t_0 + w)$ and thus does not change the mean intensity, it still changes the photon field on the level of the individual temporal modes.

Multiple Superatoms

4.3

For a single superatom we saw that it can generate non-classical states of light by shelving an excitation into the superatom's bright state, which then re-emits the photon and thus adds a non-classical single-photon Fock state onto the coherent background. This then naturally raises the question: can we chain up multiple superatoms and have them emit into the same mode?

Like for the single superatom we first consider the short binning limit $\kappa w \rightarrow 0$, for which we can exactly determine the photon state

$$\begin{aligned} \mathcal{D}^\dagger(\sqrt{w}\alpha)\rho_v\mathcal{D}(\sqrt{w}\alpha) &= \sum_{n=0}^N \sum_{m=0}^N \langle (\sqrt{\kappa w}\sigma^+(t_0))^n (\sqrt{\kappa w}\sigma^-(t_0))^m \rangle \\ &\times \sum_{k=0}^{\min(n,m)} (-1)^k \frac{|m-k\rangle\langle n-k|}{k! \sqrt{(n-k)!} \sqrt{(m-k)!}}, \end{aligned} \quad (4.12)$$

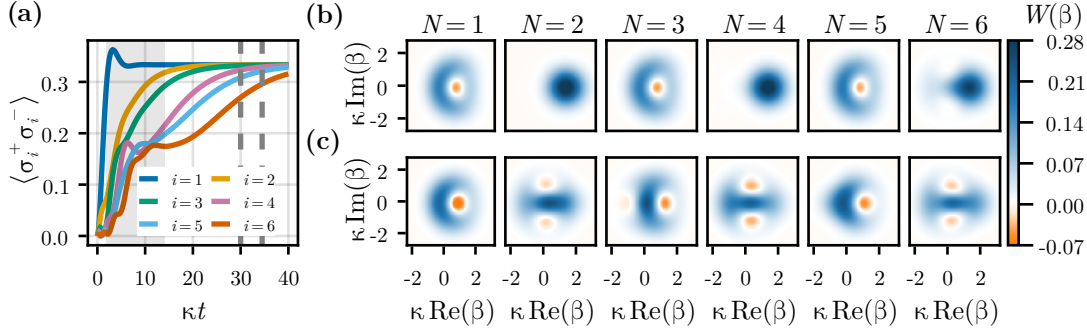


Figure 4.5

All figures at $\alpha = 0.5\sqrt{\kappa}$ and $\Gamma = 0 = \gamma_D$. **(a)** Bright state population of each superatom in a 6 superatom chain. **(b)** Wigner function of ρ_v for different number of superatoms N , as indicated by the title. The binning interval lies in the steady state for the first 5 superatoms and is indicated by vertical dashed lines in (a). **(c)** Wigner function of ρ_v for different numbers of superatoms. Here we optimised the binning interval for $W_{\text{Neg}}[\rho]$ for each N . The respective binning intervals lie in the shaded area of (a).

with $\sigma^\pm = \sum_{j=1}^N \sigma_j^\pm$ the collective ladder operators of the N superatoms. On the first glance we see our question answered in the affirmative. In the $\kappa w \rightarrow 0$ limit we can generate a N -photon state, i.e., one photon coming from each superatom. However, each photon state $|n\rangle\langle m|$ is, at least, suppressed as $(\kappa w)^{(n+m)/2}$ and ρ_v therefore mainly resembles a coherent state $|\sqrt{w}\alpha\rangle\langle\sqrt{w}\alpha|$ close to the vacuum. Hence, we again need to consider broader bins in order to generate truly non-classical states.

With $\kappa w \approx 1$ we again find that the qualitative form of the Wigner functions depends on t_0 . The two distinct regions for the bin $(t_0, t_0 + w)$ are the superatoms' steady states and the times when some superatoms still undergo Rabi oscillations. Let us first consider a bin in the steady state, as indicated by the vertical dashed lines in figure 4.5 (a). The Wigner functions show an almost perfect alternating pattern depending on whether we consider an even or odd number of superatoms,

as shown in figure 4.5 (b). More precisely, an odd number of superatoms produce the same Wigner functions as just a single superatom, while an even number configuration results in a trivial coherent state $|\sqrt{w\alpha}\rangle\langle\sqrt{w\alpha}|$.

While this result seems surprising at first, we directly find its explanation in a Bethe Ansatz analysis. Firstly, we may disregard any ramp up effects in the steady state and consider the scattering of resonant plane waves. We then split the input state into Bethe states, which decompose into different bound state configurations, as discussed in section 2.1.2. As an eigenstate of the scattering problem the bound states acquire only a phase under the scattering on a single superatom. For a bound state of n photons with eigenenergy E this phase factor becomes [165]

$$t_{E,n} = \frac{E - i\kappa n^2/2}{E + i\kappa n^2/2}. \quad (4.13)$$

Hence, for resonant plane waves, the scattering phase simplifies to $t_{0,n} = -1$ for each bound state.

Scattering on a single superatom therefore separates the incoming state into configurations of even and odd numbers of resonant bound states by phase. A second scattering event, however, completely reverts all phases back to 1 and we end up with the original input state again. Notice, that in figure 4.5 only the six superatom configuration shows slight deviations from the alternating pattern, which perfectly fits to the explanation, since, for the chosen time bin, the sixth atom is not yet in its steady state and the light can thus not be considered similar to a resonant plane wave.

We now turn our attention to bins $(t_0, t_0 + w)$ around the superatoms' Rabi oscillations, which are again the optimal choice for minimising W_{Neg} . The Wigner functions for a growing number of superatoms is depicted in figure 4.5 (c) and shows again an alternating pattern. While our previous resonant bound state argument cannot hold in this parameter regime, we can nevertheless modify it to explain why the alternating pattern remains consistent.

Firstly, we notice for multiple superatoms the superatom-superatom interactions make it impossible to define clear Rabi oscillations for all atoms. Additionally, we see that the bright state dynamics for atoms in the rear of the chain have a delayed onset. Already the fourth atom only obtains a significant bright state population after the first superatom reached its steady state. Hence, we cannot choose a binning interval $(t_0, t_0 + w)$ which has optimal emission characteristics for all superatoms. It numerically follows that we should choose the bin to favour the emission of the latter atoms.

Now, in order to see that the first superatoms in the chain are mostly irrelevant for ρ_v , which then leads to the alternating pattern of figure 4.5 (c), let us consider the Bethe state analysis again. For this, let us write the photonic input state schematically as

$$|\text{input}\rangle = |\text{resonant}\rangle + |\text{correction}\rangle, \quad (4.14)$$

where $|\text{resonant}\rangle$ is the input state for resonant plane waves, which we discussed in the paragraphs about steady state bins, and $|\text{correction}\rangle$ are the corrections due to the α -quench at $t = 0$, which we now have to take into account.

The resonant part leads to the aforementioned alternating pattern, while the correction only result in an approximatively superatom number-independent correction. To see this, let us consider the transfer matrix $t_{E,n}$ (4.13) in position space, where it becomes a convolution with the kernel $\delta(x) - \kappa n^2 e^{-\kappa n^2 x/2} \varphi(x)$. The exponential part of the kernel broadens the corrections on a scale of κn^2 per superatom scattering, which subsequently narrows the overlap with the localised mode $v(t)$. The $\delta(x)$ part of the transfer kernel leaves $|\text{correction}\rangle$ invariant, which gives the (approximatively constant) qualitative difference to the steady state bins in figure 4.5 (b).

In summary we find that with the presented setup there is a difference between the output from one and two superatoms. However, due to the observed alter-

nating pattern in the output, there is little sense in considering any additional superatoms from the point of the Wigner negativity. We may and should, however, wonder which knobs we can turn in order to make additional superatoms useful.

On the one hand, the choice for the mode projection $v(t)$ was quite specific and a more generic Ansatz will adapt better to the most non-classical mode in the output. On the other hand, we study (after the quench of α at $t = 0$) the scattering of a constant input, for which we saw that the one-particle scattering does not alter the wave function $\psi_{\text{out}}(x) = -\psi_{\text{in}}(x)$. Therefore the flat mode $v(t)$ is the best choice on the level of single-photon scattering and we will see in the next section that this choice of $v(t)$ generally captures quite a lot of the respective photons in the time bin $(t_0, t_0 + w)$. Additionally, numerical tests with the Fourier Ansatz

$$v(t) = a_0 + \sum_{n=1}^m \left[a_n \cos\left(\frac{2\pi(t-t_0)}{w}\right) + b_n \sin\left(\frac{2\pi(t-t_0)}{w}\right) \right], \quad (4.15)$$

with some cut-off m , shows no qualitative difference in the previous discussed results compared to the flat mode, but it can increase $W_{\text{Neg}}[\rho]$ by about a factor of 2.

We assume, however, that a more generic time-dependent input pulse $\alpha(t)$ may lead to significant improvements in the multiple-superatom case. This is already motivated by realising that an exponentially increasing input pulse

$$\psi_{\text{in}}(t) \propto e^{kt/2} \Theta(-t), \quad (4.16)$$

with the time evolution starting at $t = -\infty$, results in a perfect transition of the superatom into its bright state on the single-photon level [166–168]. This, on the other hand, will lead to a strongly enhanced emission of a single photon from the superatom. For a generic setup of N superatoms, we can find the optimal input

state by considering the state in which all superatoms are perfectly excited and then use the Bethe Ansatz to reverse the time evolution and find the respective photonic input state. This approach however results in multi-mode input states, as preliminary calculations for two atoms revealed. Yet, this only points to the fact, that, with a time-dependent drive $\alpha(t)$, we expect better chances to synchronise the emission of all superatoms and thus create higher non-classical states.

Observation and application of the non-classical state

4.4

4.4.1 Homodyne Detection

We have seen that we can create non-classical states ρ_v from the interaction of classical light with a single superatom. However, ρ_v just describes a single mode in the output field and we should wonder whether the light in this mode is directly accessible. For this we may compare the mean number of photons in ρ_v to the overall number of photons in the time bin $(t_0, t_0 + w)$ by integrating the mean photon intensity

$$\begin{aligned} I &= \int_{t_0}^{t_0+w} dt \langle b_{\text{out}}^\dagger(t) b_{\text{out}}(t) \rangle \\ &= \int_{t_0}^{t_0+w} dt \langle (b_{\text{in}}^\dagger(t) + i\sqrt{\kappa}\sigma^+(t)) (b_{\text{in}}(t) - i\sqrt{\kappa}\sigma^-(t)) \rangle. \end{aligned} \quad (4.17)$$

We find that ρ_v accounts for at least 70 % of all the photons in $(t_0, t_0 + w)$, when optimised for the Wigner negativity, as indicated by figure 4.6. While this shows that $v(t)$ has a good overlap with the outgoing light field, it also reveals that in any applications we also need to consider the remaining photons in the bin and it raises the question whether we can observe ρ_v in practice. Luckily for us,

4 Photon number statistics in binned modes

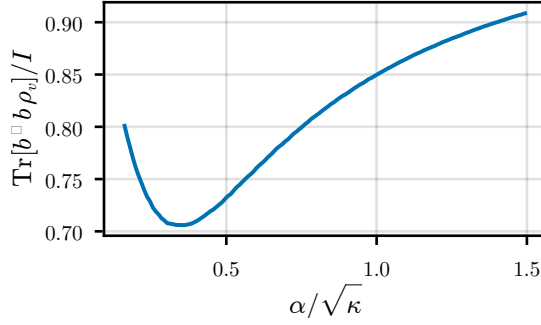


Figure 4.6

Comparison of the number of photons in mode v to the total number of photons I in the time bin $(t_0, t_0 + w)$ for different α . The bin is determined by optimising ρ_v at each α for the integrated Wigner negativity.

homodyne detection provides a way to measure ρ_v and it can aid in “removing” the unwanted orthogonal states in certain applications.

Homodyne detection provides a method to directly measure the Wigner function of a specific mode $v(t)$. This is achieved by measuring the field quadrature

$$X_\varphi = \frac{b^\dagger e^{i\varphi} + b e^{-i\varphi}}{2}. \quad (4.18)$$

From the quadrature results we then determine the characteristic function of X_φ

$$\begin{aligned} \chi(\lambda, \varphi) &= \langle e^{i\lambda X_\varphi} \rangle = \left\langle \exp \left(i \frac{b^\dagger \lambda e^{i\varphi} + b \lambda e^{-i\varphi}}{2} \right) \right\rangle \\ &= \langle \mathcal{D}(i\lambda e^{i\varphi}) \rangle, \end{aligned} \quad (4.19)$$

with \mathcal{D} the displacement operator. We can directly determine the Wigner function from χ , which follows immediately from our original definition of the

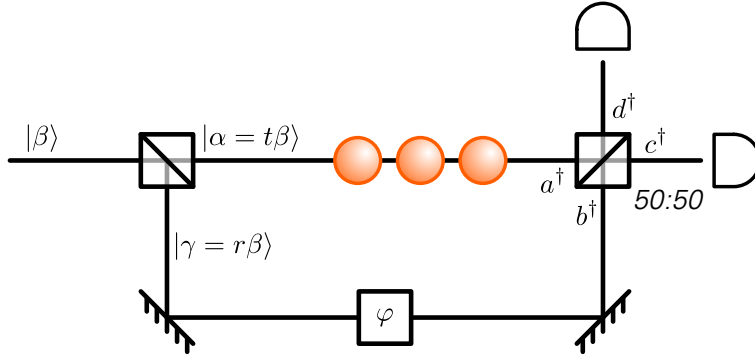


Figure 4.7

Homodyne detection scheme. First, an coherent input beam is split at a beam splitter of reflectance r and transmittance t with $r \gg t$. The transmitted light interacts with the superatom system. The reflected beam is rerouted and recombined with the transmitted beam at a balanced beam splitter, while picking up a controlled phase of φ relative to the transmitted beam. Finally, two detectors measure the intensity of both output beams.

Wigner function (4.7)

$$\begin{aligned} W(\alpha) &= \frac{1}{\pi^2} \int d^2\beta \operatorname{Tr} \left(\rho e^{\beta(a^\dagger - \alpha^*) - \beta^*(a - \alpha)} \right) \\ &= \frac{1}{\pi^2} \int d^2\beta e^{-\beta\alpha^* + \beta^*\alpha} \langle \mathcal{D}(\beta) \rangle. \end{aligned} \quad (4.20)$$

Hence, we only need an efficient way to measure the quadrature X_φ . For this consider now the setup depicted in figure 4.7. First we start with a strong coherent state $|\beta\rangle$ and split it at the first beam splitter into the probe beam $|\alpha = t\beta\rangle$ and a reference beam $|\gamma = r\beta\rangle$, with the reference beam stronger than the probe, i.e., $|r| \gg |t|$. The probe beam interacts with the superatoms, while the reference beam's phase relative to $|\alpha\rangle$ is shifted to φ . Now, both beams are combined at a 50 : 50 beam splitter and we measure the intensity in both output ports, labelled c and d .

The crucial step now is to consider the difference in the measured intensity

$$I = \frac{d^\dagger d - c^\dagger c}{2|\gamma|} = \frac{a^\dagger b + b^\dagger a}{2|\gamma|}, \quad (4.21)$$

normalised to the reference beam's amplitude $|\gamma|$. Here we used the input-output relations of a balanced beam splitter $c = (a - b)/\sqrt{2}$, $d = (a + b)/\sqrt{2}$. It then follows that, in the $|\gamma| \rightarrow \infty$ limit, the characteristic function of I and X_φ coincide [169]

$$\lim_{|\gamma| \rightarrow \infty} \langle e^{i\lambda I} \rangle = \chi(\lambda, \varphi). \quad (4.22)$$

In order to measure ρ_v in the specific flat mode v , we can simply cut out the specific part in $|\gamma\rangle$, for example, by placing a fast shutter in the reference beam path or by only taking detection results within this time window. All other modes in the a channel, orthogonal to $v(t)$ are then suppressed in the $|\gamma| \rightarrow \infty$ limit. Thus, we have direct access to ρ_v by augmenting our setup just by linear optical devices and two detectors.

4.4.2 Application in quantum metrology

The last section revealed that we can directly measure ρ_v . Yet, this does not imply that we may use ρ_v in arbitrary experiments, since, depending on the application, quantum interactions mixes the light in mode v with arbitrary other modes. On the other hand, this problem does not emerge in applications that only rely on linear quantum optics, where there is no mode-mixing. Here we can directly route the superatom output into the experiment and select the correct mode v at the end via homodyne detection, as discussed before.

As such an application, we discuss is phase estimation in quantum metrology. Before we explain our setup, however, we should first introduce more general concepts of quantum metrology and establish the needed notation.

Assume we possess a quantum state ρ with which we want to determine some

4.4 Observation and application of the non-classical state

unknown quantity φ . For this we need two things: a φ -dependent interaction G of ρ with the environment, and an estimator Φ_{est} that we can measure and which is correlated to φ , i.e., $\langle \Phi_{\text{est}} \rangle \approx \varphi$. Let us from here on assume the interaction is Hermitian and linear in φ

$$\rho_\varphi = e^{-i\varphi G} \rho e^{i\varphi G}. \quad (4.23)$$

In order to gauge the precisions for the φ -estimation we should now investigate the mean squared distance

$$\langle (\Phi_{\text{est}} - \varphi)^2 \rangle = \Delta\Phi_{\text{est}}^2 + b^2(\varphi), \quad (4.24)$$

where $\Delta\Phi_{\text{est}}$ is the standard deviation of the estimator and $b(\varphi) = \langle \Phi_{\text{eff}} - \varphi \rangle$ its bias. The standard deviation may now be bounded from below by the Heisenberg uncertainty principle

$$\begin{aligned} \Delta\Phi_{\text{est}}^2 \Delta G^2 &\geq \frac{1}{4} |\text{Tr}([\Phi_{\text{est}}, G]\rho_\varphi)|^2 \\ &= \frac{1}{4} |\text{Tr}(\Phi_{\text{est}} \partial_\varphi \rho_\varphi)|^2 \\ &= \frac{1}{4} \left| \frac{\partial \langle \Phi_{\text{est}} \rangle}{\partial \varphi} \right|^2 = \frac{1}{4} |1 + b'(\varphi)|^2. \end{aligned} \quad (4.25)$$

This then leads to the *Helstrom-Holevo lower bound* [170, 171]

$$\langle (\Phi_{\text{est}} - \varphi)^2 \rangle \geq \frac{|1 + b'(\varphi)|^2}{4\Delta G^2} + b^2(\varphi), \quad (4.26)$$

or, for an unbiased estimator $b = 0$,

$$\Delta\Phi_{\text{est}}^2 \geq \frac{1}{4\Delta G^2}. \quad (4.27)$$

The Helstrom-Holevo bound is one of the most generic bounds on the sensi-

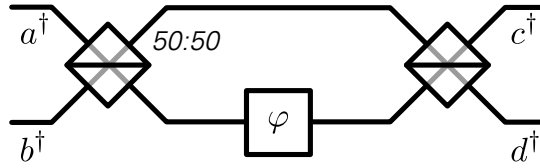


Figure 4.8

Interferometer setup for estimation of the unknown phase φ .

tivity of many metrology experiments. It directly reveals that the best obtainable precision is always bounded by the standard deviation of G . This implies that optimal parameter estimation is an interplay between choosing both the correct experimental protocol G and a suitable input state ρ as only these two quantities enter in ΔG .

The Helstrom-Holevo lower bound has one blemish, which is that the bound is generally not sharp, especially for mixed states. Generally, the *Cramér-Rao bound* for an unbiased estimator [172, 173] improves on the Helstrom-Holevo bound

$$\langle \Delta \Phi_{\text{eff}}^2 \rangle \geq \frac{1}{F(\varphi)} \geq \frac{1}{4\Delta G^2}. \quad (4.28)$$

Here, the Quantum-Fisher information is defined as $F(\varphi) = \text{Tr}(\rho_\varphi L^2(\rho_\varphi, G))$, where L is the *symmetric logarithmic derivative* defined by the equation $i[\rho_\varphi, G] = \{\rho_\varphi, L(\rho_\varphi, G)\}/2$. Considering only pure states ρ , we can always find a state ρ and a measurement G such that $F(\varphi) = 4\Delta G^2$. For mixed states this is no longer true [116], and the Cramér-Rao bound provides a sharper bound for the optimal parameter estimation.

We now turn our attention to the quantum metrology problem we want to study, which is the estimation of an unknown phase φ by interferometry, as depicted in figure 4.8. Here we want to send in light at the input ports a and b , which then enter a balanced interferometer, whose two beam paths acquire an unknown relative phase difference of φ . The light then interferes at the output beam splitter and we want to subsequently estimate φ by intensity measurements

4.4 Observation and application of the non-classical state

at the output ports c and d .

The simplest input for this setup is probably a single coherent state on one of the input ports, which leads to a precision of the estimation

$$\Delta\Phi_{\text{est}}^2 \propto \frac{1}{N}, \quad (4.29)$$

where N is the mean photon number of the input beam. This $1/N$ scaling is known as *shot noise* or the *standard quantum limit of interferometry*. The natural question is whether a non-classical state can improve this limit and the first surprising result is that even a N -photon Fock state shows the same $1/N$ scaling in precision. However, the trick lies in using both input ports and let the light from both ports interfere in such a way to increase the precision of the estimation. With this, a scaling of up to $1/N^2$ is possible, denoted as the Heisenberg limit. For details on these results we refer to the textbook [116] and the review article [174].

Yet reaching the Heisenberg limit requires highly entangled or non-classical input states and perfect experimental control [175–177]. Therefore let us consider a more practical setup, where we want to input coherent light in one of the input ports and augment it by a non-classical state in the second input port. The most prominent example for this is the use of squeezed light, for which C. M. Caves and co-workers first determined the improvement over the standard quantum limit [178, 179] and later proofed that squeezed light is the asymptotically optimal auxiliary input to augment coherent light [180]. Famously, modern gravitational wave detectors utilise this coherent state and squeezed state input combination in order to achieve the necessary precisions in their interferometers [134, 135, 181].

Creating strongly squeezed light is a formidable task and typically requires complex setups [182]. Therefore, we now want to study whether the non-classical state ρ_v , which we can easily generate from the interaction of classical light with superatoms, is a suitable auxiliary state for the quantum phase estimation problem.

4 Photon number statistics in binned modes

We use the setup depicted in figure 4.8 and use the relative intensity on both output ports

$$J_z = \frac{d^\dagger d - c^\dagger c}{2} \quad (4.30)$$

as the estimator for φ . By the error propagation formula $\Delta J_z \approx \Delta\varphi \partial\langle J_z \rangle / \partial\varphi$ we define the *optimal sensitivity* as

$$\Delta\varphi = \min_{\varphi} \frac{\Delta J_z}{\left| \frac{\partial\langle J_z \rangle}{\partial\varphi} \right|}. \quad (4.31)$$

For the actual calculations we use the input-output relations of a phase shifter $a_{\text{out}} = e^{-i\varphi} a_{\text{in}}$ and of a balanced beam splitter (see below equation (4.21)) in order to express J_z by the input fields [174]

$$J_z = \cos(\varphi) J_z^{(\text{in})} - \sin(\varphi) J_x^{(\text{in})} \quad (4.32)$$

with

$$J_z^{(\text{in})} = \frac{a^\dagger a - b^\dagger b}{2}, \quad J_x^{(\text{in})} = \frac{a^\dagger b + b^\dagger a}{2}, \quad (4.33)$$

up to a global phase².

In figure 4.9 we compare the achievable φ -sensitivity for our combination of a coherent state $|\sqrt{N_b}\rangle$ and ρ_v against shot-noise $\Delta\varphi_{\text{SN}} = 1/\sqrt{N_a + N_b}$. For a fair comparison we take $N_a = w|\alpha|^2$, i.e., we assume that in the shot-noise case all photons in the input port a contribute to detection. As previously discussed, in section 4.3, we generally assume at $\gamma_D = 0$ an alternating behaviour depending on the parity of the number of superatoms, therefore we limit the discussion to only one and two superatoms.

We find that, at already moderate coherent probe strengths $N_b \geq 10$, there is a consistent improvement of the sensitivity compared to shot-noise. For a single

²The J_a notation follows from the Jordan-Schwinger representation of angular momentum operators by two coupled harmonic oscillators [183, 184].

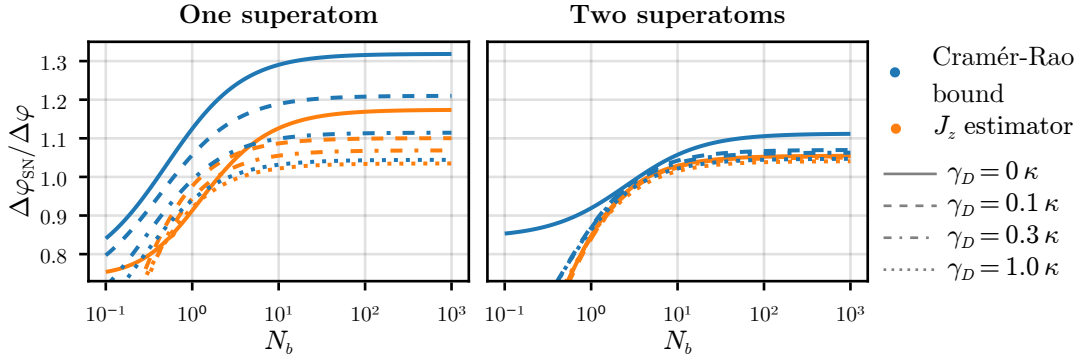


Figure 4.9

Sensitivity improvements over shot noise for ρ_v generated from one and two superatoms. Blue curves represent the Cramér-Rao bound, i.e., the theoretically highest obtainable sensitivity, and orange curves show the obtainable sensitivity from the J_z estimator (4.30). The different dashed lines represent different values of γ_D . The binning intervals $(t_0, t_0 + w)$ were determined by numerically optimising the Cramér-Rao bound and the J_z estimation at γ_D and $N_b = 100$.

superatom the sensitivity improvement can be as large as 30 % from the Cramér-Rao bound, and even with the simple J_z estimator we reach a 17 % improvement. On the one hand, the sensitivity gain is sensitive to dephasing γ_D and already weak noise reduces the sensitivity significantly for a single superatom. On the other hand, even at high dephasing $\gamma_D = \kappa$ we find a consistent improvement over the standard quantum limit, which is on the order of 3.5 %.

Compared to ρ_v from a single superatom, the two superatom results show a much tighter grouping, with barely any γ_D dependence for the J_z estimator. While the overall sensitivity at small γ_D is smaller than for a single superatom, the sensitivity at large dephasing $\gamma_D = \kappa$ lies a little over the single superatom result with an improvement of 4 %.

This behaviour appears to be a consistent when increasing the number of superatoms, as illustrated in figure 4.10. At very large detuning $\gamma_D = 2\kappa$ using

4 Photon number statistics in binned modes

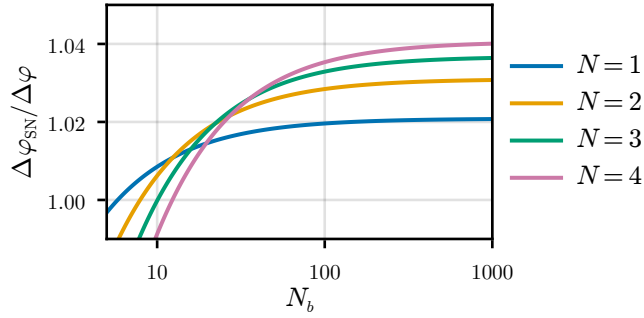


Figure 4.10

Sensitivity improvement at high dephasing $\gamma_D = 2\kappa$ for N superatoms. The binning interval is obtained by optimising ρ_v for $\Delta\varphi$ at $N_b = 100$.

multiple superatoms for the creation of ρ_v has positive effects on the obtainable sensitivity. We explain this by noting that at high dephasing our previous Bethe state analysis breaks down and each superatom only weakly adds to the non-classicality of ρ_v , however the effect from multiple superatoms is now accumulative.

It should be noted, that a squeezed state with the same mean number of photons as in our dephasing free single superatom example shows a 30% sensitivity improvement with J_z , clearly outperforming our non-classical state ρ_v . However, the optimal non-classical resource is also determined by practical considerations and we should remember that our analysis holds for any chiral two-level system and is not just bound to Rydberg superatoms. Therefore, ρ_v might be a promising candidate for metrology experiments in some platforms.

Appendix: Exact density matrix for short bins

4.A

In principle, we can find the density matrix ρ_v of the photons in mode v by determining each matrix element separately

$$(\rho_v)_{m,n} = \langle |n\rangle\langle m| \rangle = \frac{1}{\sqrt{n!m!}} \langle : (b_v^\dagger)^n e^{-b_v^\dagger b_v} b_v^m : \rangle. \quad (4.34)$$

Here, $: f(b_v^\dagger, b_v) :$ denotes the normal ordering of $f(b_v^\dagger, b_v)$. Since

$$b_v = \frac{1}{\sqrt{w}} \int_{t_0}^{t_0+w} dt (\alpha + \sqrt{\kappa} \sigma^-(t)), \quad (4.35)$$

the relation (4.34) for ρ_v generally yields out-of-time-ordered correlation functions. Therefore, the direct determination of ρ_v is impractical in most situations. However, in the $w \rightarrow 0$ limit we approximatively have $b_v \approx \sqrt{w}(\alpha + \sqrt{\kappa} \sigma^-(t_0))$, which allows us to calculate ρ_v from the superatom density matrix at time t_0 .

Assuming N superatoms, we can expand the expectation value in (4.34) as

$$\begin{aligned} : (b_v^\dagger)^n e^{-b_v^\dagger b_v} b_v^m : &= \sqrt{w}^{n+m} \sum_{k=0}^{\infty} \frac{(-w)^k}{k!} (\alpha^* + \sqrt{\kappa} \sigma^+)^{n+k} (\alpha + \sqrt{\kappa} \sigma^-)^{m+k} \\ &= \sqrt{w}^{n+m} \sum_{\tilde{n}=0}^N (\alpha^*)^{n-\tilde{n}} (\sqrt{\kappa} \sigma^+)^{\tilde{n}} \sum_{\tilde{m}=0}^N \alpha^{m-\tilde{m}} (\sqrt{\kappa} \sigma^-)^{\tilde{m}} \\ &\quad \times \sum_{k=0}^{\infty} \frac{(-w|\alpha|^2)^k}{k!} \binom{n+k}{\tilde{n}} \binom{m+k}{\tilde{m}} \end{aligned} \quad (4.36)$$

As the output cavity is constantly pumped by the coherent background α , we expect that ρ_v largely resembles a coherent state $|\sqrt{w}\alpha\rangle$. Therefore, we want to rearrange (4.36) such that we can directly identify the coherent state contribution.

4 Photon number statistics in binned modes

For this we first introduce the coherent state normalisation factor $e^{-w|\alpha|^2}$ by inserting $1 = e^{-w|\alpha|^2} e^{w|\alpha|^2}$. Then we expand the positive exponential and thereon collect all terms of equal power in $(w|\alpha|^2)^k$, resulting in

$$\begin{aligned}
& : (b_v^\dagger)^n e^{-b_v^\dagger b_v} b_v^m : \\
& = (\sqrt{w}\alpha^*)^n (\sqrt{w}\alpha)^m e^{-w|\alpha|^2} \sum_{\tilde{n}=0}^N \frac{1}{\tilde{n}!} \left(\frac{\sqrt{\kappa}\sigma^+}{\alpha^*} \right)^{\tilde{n}} \sum_{\tilde{m}=0}^N \frac{1}{\tilde{m}!} \left(\frac{\sqrt{\kappa}\sigma^-}{\alpha} \right)^{\tilde{m}} \quad (4.37) \\
& \quad \times \sum_{k=0}^{\infty} \frac{(w|\alpha|^2)^k}{k!} \sum_{i=0}^k (-1)^i \binom{k}{i} (n+i)^{\tilde{n}} (m+i)^{\tilde{m}} \\
& = \sqrt{n!m!} \langle m | \sqrt{w}\alpha \rangle \langle \sqrt{w}\alpha | n \rangle \sum_{\tilde{n}=0}^N \frac{1}{\tilde{n}!} \left(\frac{\sqrt{\kappa}\sigma^+}{\alpha^*} \right)^{\tilde{n}} \sum_{\tilde{m}=0}^N \frac{1}{\tilde{m}!} \left(\frac{\sqrt{\kappa}\sigma^-}{\alpha} \right)^{\tilde{m}} \\
& \quad \times \sum_{k=0}^{\infty} \frac{(-w|\alpha|^2)^k}{k!} \Delta^k \Big|_{x=0} (n+x)^{\tilde{n}} (m+x)^{\tilde{m}}. \quad (4.38)
\end{aligned}$$

In the last line we used $\langle n, m | \sqrt{w}\alpha \rangle$ to get rid of the $(\sqrt{w}\alpha)^{n,m}$ terms and to make the identification of the density matrix element $(\rho_v)_{m,n} = \langle m | \rho_v | n \rangle$ easier.

In (4.38) we introduced the falling factorial $x^{\underline{n}} = x(x-1)\dots(x-n+1)$, and the forward difference operator $\Delta f(x) \equiv f(x+1) - f(x)$. For the simplification in the second step we used

$$(-1)^k \Delta^k f(x) = \sum_{i=0}^k (-1)^i \binom{k}{i} f(x+i) \quad (4.39)$$

which essentially is Newton's interpolation formula [185]. Next, we eliminate n

and m from (4.38) with the number operator $n|n\rangle = b^\dagger b|n\rangle$, resulting in

$$\begin{aligned} \rho_v = & \sum_{\tilde{n}=0}^N \sum_{\tilde{m}=0}^N \frac{1}{\tilde{n}!} \frac{1}{\tilde{m}!} \left\langle \left(\frac{\sqrt{\kappa}\sigma^+}{\alpha^*} \right)^{\tilde{n}} \left(\frac{\sqrt{\kappa}\sigma^-}{\alpha} \right)^{\tilde{m}} \right\rangle \\ & \times \sum_{k=0}^{\infty} \frac{(-w|\alpha|^2)^k}{k!} \Delta^k \Big|_{x=0} (b^\dagger b + x)^{\tilde{m}} |\sqrt{w}\alpha\rangle \langle \sqrt{w}\alpha| (b^\dagger b + x)^{\tilde{n}}. \end{aligned} \quad (4.40)$$

It is now evident that the coherent state $|\sqrt{w}\alpha\rangle \langle \sqrt{w}\alpha|$ enters ρ_v . Yet, the repeated application of the operator $b^\dagger b$ in the sums can potentially result in a ρ_v , which has little resemblance to a coherent state. This is not the case, however, and in the next part we show that the sums terminate and the $b^\dagger b$ -operator products only add up to N photons to ρ_v .

The algebra of finite differences with falling factorials are in many ways similar to the algebra of derivatives and monomials. For example, we have $\Delta x^n = nx^{n-1}$, and there is the generalised product rule $\Delta fg = (\Delta f)g + f(\Delta g) + (\Delta f)(\Delta g)$. Therefore, equation (4.40) will only contain falling factorials of the number operator, which are exactly its normal ordered powers $(b^\dagger b)^n =: (b^\dagger b)^n$. Therefore, ρ_v in (4.40) is invariant under the set of replacements

$$\Delta \Big|_{x=0} \mapsto (\partial_x + \partial_y + \partial_x \partial_y) \Big|_{x=0=y} \quad (4.41)$$

$$\begin{aligned} (b^\dagger b + x)^{\tilde{m}} |\sqrt{w}\alpha\rangle & \mapsto : (b^\dagger b + x)^{\tilde{m}} : |\sqrt{w}\alpha\rangle = (\sqrt{w}\alpha b^\dagger + x)^{\tilde{m}} |\sqrt{w}\alpha\rangle \\ & = \mathcal{D}(\sqrt{w}\alpha) (\sqrt{w}\alpha b^\dagger + w|\alpha|^2 + x)^{\tilde{m}} |0\rangle \end{aligned} \quad (4.42)$$

$$\begin{aligned} \langle \sqrt{w}\alpha| (b^\dagger b + x)^{\tilde{n}} & \mapsto \langle \sqrt{w}\alpha| : (b^\dagger b + y)^{\tilde{n}} := \langle \sqrt{w}\alpha| (\sqrt{w}\alpha^* b + y)^{\tilde{n}} \\ & = \langle 0| (\sqrt{w}\alpha^* b + w|\alpha|^2 + y)^{\tilde{n}} \mathcal{D}^\dagger(\sqrt{w}\alpha). \end{aligned} \quad (4.43)$$

The k -summation now yields two translation operators $T_{x,y}(-w|\alpha|^2)$ for x, y , and the operator $\exp(-w|\alpha|^2 \partial_x \partial_y)$. The translation operators exactly cancel the $w|\alpha|^2$ terms in (4.42) and (4.43), and, after rescaling $x \mapsto \sqrt{w}\alpha x, y \mapsto \sqrt{w}\alpha^* y$,

4 Photon number statistics in binned modes

we end up with the density matrix

$$\begin{aligned}
& \mathcal{D}^\dagger(\sqrt{w}\alpha)\rho_v\mathcal{D}(\sqrt{w}\alpha) \\
&= \sum_{\tilde{n}=0}^N \sum_{\tilde{m}=0}^N \frac{1}{\tilde{n}!} \frac{1}{\tilde{m}!} \left\langle (\sqrt{\kappa w}\sigma^+)^{\tilde{n}} (\sqrt{\kappa w}\sigma^-)^{\tilde{m}} \right\rangle e^{-\partial_x\partial_y} \Big|_{x,y=0} (b^\dagger + x)^{\tilde{m}} |0\rangle \langle 0| (b + y)^{\tilde{n}} \\
&= \sum_{\tilde{n}=0}^N \sum_{\tilde{m}=0}^N \left\langle (\sqrt{\kappa w}\sigma^+)^{\tilde{n}} (\sqrt{\kappa w}\sigma^-)^{\tilde{m}} \right\rangle \sum_{k=0}^{\min(\tilde{n},\tilde{m})} (-1)^k \frac{|\tilde{m} - k\rangle \langle \tilde{n} - k|}{k! \sqrt{(\tilde{n} - k)!} \sqrt{(\tilde{m} - k)!}}.
\end{aligned}$$

Here, the right hand side is spanned by the truncated Fock space $\{|0\rangle, \dots, |N\rangle\}$. Thus, we see that, in the $w \rightarrow 0$ limit, ρ_v becomes a $(N + 1)$ -state mixture of N -photon added coherent states.

5

Photon subtraction with cascaded superatoms

In the previous two chapters, we analysed how the superatom-mediated photon-photon interactions lead to strong temporal and number correlations in the transmitted light field. In both cases, we identified the dephasing γ_D of the Rydberg superatom into one of its non-radiating dark states as the most significant inhibitor to the observed and predicted effects. Once a superatom dephases into the dark state manifold, it effectively vanishes from the system on the time scales of the experiment. While this effect is detrimental to the photon correlations, it opens the door for another application. More precisely, the superatoms act as controlled photon absorbers, as each dephased superatom removes exactly one photon from the transmitted light field.

One of the major applications of photon subtraction is in state preparation. More concretely, photon-subtracted states are crucial resources in quantum computing [186–188], metrology [189], and the study of fundamental aspects of quantum optics [190]. Photon subtraction is readily achieved via post-selection or in heralded systems [191, 192], such as imbalanced beam splitters [193]. This, however, introduces a probabilistic component. On the other hand, the Rydberg

blockade guarantees the absorption of no more than one photon by the superatom, making it an ideal system for deterministic photon subtraction.

In this chapter, we will analyse the optimal parameter regimes for photon subtraction with dephased Rydberg superatoms. We will see that Raman decay becomes one of the greatest obstacles for controlled photon subtraction, and we will demonstrate that the proposed setup scales well to systems with multiple superatoms, therefore showing the potential for the subtraction of an arbitrary number of photons from an input pulse. Finally, we will show experimental results for a system of up to 3 superatoms and discuss the potential scaling to up to 8 atoms.

This chapter is based on the article [92]. Here, the author of this thesis contributed the theoretical analysis and all theoretical results in this chapter are from the author, if not explicitly stated otherwise.

Optimal parameters for a single-photon subtractor

5.1

5.1.1 Perfect absorption of a single-photon Fock state

At first glance, we might expect that increasing γ_D will also increase the chance of subtracting a photon from the input field. Contrary to the intuition, this approach fails, which we readily see by considering the dynamics of a single superatom in the presence of dephasing. Effectively, the dephasing acts like an imaginary detuning

$$H_{\text{det}} = -i\gamma_D\sigma^+\sigma^- \quad (5.1)$$

of the bright state. This follows from the quantum Monte Carlo wave function [109] or quantum trajectory [110] approach, where the anti-commutator part of the Lindblad dissipator $\gamma_D\mathcal{D}_{|D\rangle\langle W|}[\rho]$ is added to the Hamiltonian. Hence,

5.1 Optimal parameters for a single-photon subtractor

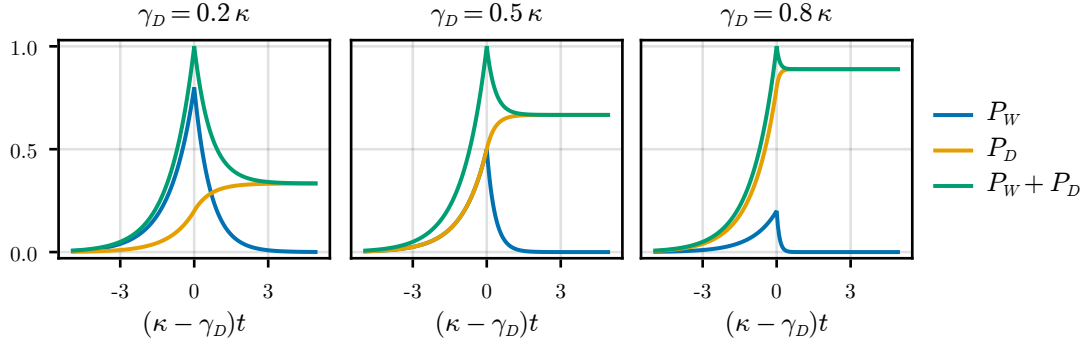


Figure 5.1

Bright state population P_W , dark state population P_D and total population of a single superatom for an incoming single photon with the wave function (5.2) at different γ_D .

strong dephasing brings the atom out of resonance, and we expect an overall weakened coupling of the incoming light field to the superatom.

This brings us to the question of how we should pick γ_D to have the best chance for subtracting a photon. Let us first answer this question for a single input photon, which will provide us with first insights for our subsequent analysis of a coherent input field. As a secondary result, we will see that we can achieve perfect photon subtraction in the case of a single input photon.

We already discussed in section 4.3 that for a superatom without dephasing an exponentially increasing mode $\psi_{\text{in}}(t) = \sqrt{\kappa}\Theta(-t)\exp(\kappa t/2)$ yields perfect absorption of the incoming photon into the bright state. This should be the starting point for our analysis, as we first have to populate the bright state $|W\rangle$ before we can dephase into the dark state manifold $|D\rangle$. We now modify this Ansatz, for $\gamma_D < \kappa$, to

$$\psi_{\text{in}}(t) = \sqrt{\kappa - \gamma_D}\Theta(-t)e^{-(\kappa - \gamma_D)t/2}. \quad (5.2)$$

We show this in appendix 5.A of this chapter that this state yields perfect absorption into the $\{|W\rangle, |D\rangle\}$ manifold at $t = 0$, as illustrated in figure 5.1.

From this, we also find the asymptotic dark state population

$$\lim_{t \rightarrow \infty} P_D(t) = \frac{2\gamma_D}{\kappa + \gamma_D}, \quad \text{when } \gamma_D < \kappa. \quad (5.3)$$

Perfect transition into the dark state thus occurs for $\gamma_D = \kappa$. This directly shows that perfect absorption is indeed possible at finite dephasing and not necessarily in the $\gamma_D \rightarrow \infty$ limit. Yet, this result comes with one caveat: the input state (5.2) is not well-defined for $\gamma_D \rightarrow \kappa$. As ψ_{in} becomes increasingly flat as γ_D approaches κ , we should interpret ψ_{in} in the $\gamma_D \rightarrow \kappa$ limit as a resonant plane wave.

Additionally, our Ansatz (5.2) cannot predict the absorption behaviour for $\gamma_D > \kappa$. While we know that photon absorption eventually has to become unlikely for sufficiently large γ_D , we yet have no way to quantify this with the presented Ansatz. In the next section, we discuss coherent light, for which we perform a full numerical parameter scan, and we find that photon subtraction is quite efficient for an extensive range of γ_D but eventually diminishes as $\gamma_D \rightarrow \infty$, as predicted in the beginning.

5.1.2 Optimal absorption with resonant, coherent light

Our single-photon discussion revealed that a resonant plane wave is optimal for absorption. While this certainly can change in a multi-photon setup, the plane wave is an excellent starting point for the discussion of the interaction of a superatom with coherent light since this lends itself to a quite simple theoretical model and describes a superatom in a continuous wave setup. Therefore, similar to the last chapter, we now consider a single superatom with dephasing γ_D in the vacuum. Then at time $t = 0$, we turn on a coherent light field of amplitude α and drive damped Rabi oscillations. We now want to maximise the probability for the superatom to be in the dark state at some later time τ .

We show in figure 5.2 multiple parameter scans of the dark state population

5.1 Optimal parameters for a single-photon subtractor

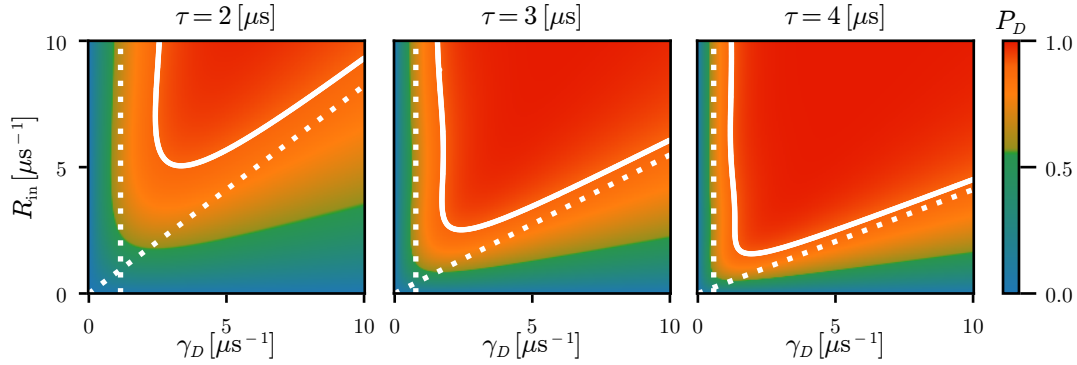


Figure 5.2

Dark state population for a single superatom for different coherent pumping durations τ . The white lines show the 90 % population level and the dashed vertical and diagonal lines indicate $\exp(-\gamma_D \tau) = 0.1$ and $\exp(-4\kappa R_{\text{in}} \tau / \gamma_D) = 0.1$, respectively. We use $\kappa = 0.35 \mu\text{s}$, $\Gamma = 0$, and SI-units for better comparison with the experimental results.

P_D for different driving durations τ . It is evident that for a fixed input photon rate R_{in} , there is an optimal region for γ_D for which photon subtraction becomes very likely. Obviously, when we increase the pulse duration τ , then the optimal parameter range for R_{in} and γ_D increases as well, as the superatom has more time to decay into the dark state manifold, even with suboptimal parameters. However, in the next section, we will discuss the impact of the Raman decay Γ , and we will see strong non-deterministic photon losses at large τ . We should therefore limit ourselves to short pulses and discuss the two relevant mechanisms that bound the photon subtraction in this regime.

First of all, we need a large enough dephasing $\gamma_D \tau \gg 1$ so that the dark state can be populated during the pulse. On the other hand, we showed in the last section that for large γ_D , the bright state becomes effectively detuned, which inhibits photon absorption. In this regime, the bright state can never reach a significant population, and we may adiabatically eliminate it from our master equation. We then end up with a classical rate equation for the ground state

5 Photon subtraction with cascaded superatoms

and dark state population

$$\partial_t \rho_{GG} = -\gamma_{\text{eff}} \rho_{GG}, \quad (5.4)$$

$$\partial_t \rho_{DD} = \gamma_{\text{eff}} \rho_{GG}, \quad (5.5)$$

where we have the effective decay rate

$$\gamma_{\text{eff}} = \frac{4\kappa R_{\text{in}} \gamma_D}{(\kappa + \gamma_D)^2 + 4\kappa R_{\text{in}}}. \quad (5.6)$$

As expected, the effective decay rate vanishes for large γ_D , i.e., it becomes increasingly unlikely to populate the dark state for $\gamma_D \rightarrow \infty$. For large γ_D , we may approximate the effective decay rate as $\gamma_{\text{eff}} \approx 4\kappa R_{\text{in}}/\gamma_D$ and therefore see that we can counteract the detrimental effects of large γ_D by increasing the input photon rate accordingly. This accumulates to the second condition for ideal photon subtraction, which is $\gamma_{\text{eff}} \tau \gg 1$. This condition, in the large γ_D approximation, is indicated by the diagonal line in figure 5.2 and almost perfectly reproduces numerical $P_D = \text{const.}$ levels for large γ_D .

5.1.3 Influence of Raman decay

So far, our setup yields deterministic photon subtraction in the sense that we can bring the dark state population P_D arbitrarily close to 100 %, which translates directly into the removal of a single photon from the transmitted photon field. However, this is no longer true when we have Raman decay Γ , as this can scatter a photon outside of the waveguide and thus leads to additional photon losses. More importantly, these losses are non-deterministic since the number of photons lost due to Raman decay fluctuates with each experimental realisation.

Our current superatom model allows us to estimate the mean number of lost

5.1 Optimal parameters for a single-photon subtractor

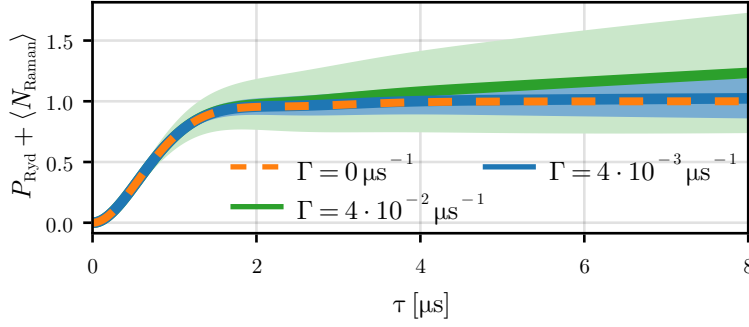


Figure 5.3

Total Rydberg population and Raman losses for a single superatom at an input intensity of $R_{\text{in}} = 5$ photons/ μs , a dephasing of $\gamma_D = 2.4 \mu\text{s}^{-1}$, and $\kappa = 0.35 \mu\text{s}^{-1}$. The shaded regions show one standard deviation Δn of the number of photons lost due to Raman emission. The blue curve represents the experimental parameters $\{\kappa, \Gamma, \gamma_D\}$ for three superatom.

photons due to Raman decay, which is

$$\langle N_{\text{Raman}} \rangle = \Gamma \int_0^t ds P_{\text{Ryd}}(s), \quad (5.7)$$

with $P_{\text{Ryd}} = P_W + P_D$. This directly follows from the superatom master equation in which both the bright and the dark states are subject to Raman decay with rate Γ . However, with our current superatom model, we cannot access the photon fluctuations due to the Raman decay.

For this, we now augment our description of the superatom by an auxiliary cavity, which stores the Raman emitted photons. More precisely, we modify the Raman decay operators in the master equation (2.21) to

$$\Gamma \mathcal{D}_{|G\rangle\langle W|\otimes V^\dagger}[\rho] + \Gamma \mathcal{D}_{|G\rangle\langle D|\otimes V^\dagger}[\rho], \quad (5.8)$$

where the auxiliary cavity is described by a harmonic oscillator for which we

introduced the *Susskind-Glogower ladder operator* [194]

$$V^\dagger = \sum_{n=0}^{\infty} |n+1\rangle\langle n| = a^\dagger \frac{1}{\sqrt{aa^\dagger}}. \quad (5.9)$$

We need the Susskind-Glogower ladder operator instead of the ordinary ladder operator a^\dagger , as the action of a^\dagger leads to stimulated emission, while V^\dagger results in a constant Raman decay rate Γ , independent of the number of photons in the auxiliary cavity¹. We then have access to the mean number of photons and the photon fluctuations in the cavity through the cavity number operator, i.e., $\langle n \rangle = \langle a^\dagger a \rangle$ and $\langle \Delta n^2 \rangle$, respectively.

Figure 5.3 shows the total number of subtracted photons, i.e., the Rydberg population, together with the Raman losses and the respective uncertainty due to the probabilistic decay. Even for $\Gamma = 0.04 \mu\text{s}^{-1}$, which is two orders of magnitude smaller than γ_D , we find that the chance of losing an additional photon is substantial. Already at short times $\tau = 1 \mu\text{s}$, the uncertainty in the lost photons Δn is on the order of 0.1 photons, increasing approximately linearly in the pulse duration τ . The discussed Raman decay rate $\Gamma = 0.04 \mu\text{s}^{-1}$ coincides with the experimentally determined value [92]. So, while a reduction of Γ obviously helps against these effects, this cannot be achieved without modifications to the experiment, and we should therefore limit the photon subtraction to short pulses.

¹We numerically verified that this modification leaves the superatom dynamics invariant.

Experimental results and scaling to multiple superatoms

5.2

5.2.1 Discussion of the experiment

In the actual experiment, we studied up to three superatoms. For their creation, we first loaded the crossed optical dipole trap with a cigar-shaped ensemble of Rubidium atoms. After a cooling step, we activated up to three tightly focused optical traps, orthogonally intersecting the original ensemble. The positions of these optical traps could be tuned, and we used separations of $\approx 75 \mu\text{m}$ for two superatoms and $\approx 50 \mu\text{m}$ for three superatoms between each individual sub-ensemble. The extent of the reservoir trap limited the overall separation and the potential number of superatoms. Next, we turned off the crossed dipole trap so that additional atoms outside the sub-traps could escape the inter-trap region before turning the dipole trap back on. This trapping scheme shows a qualitative difference in the number of Rubidium atoms per superatom, depending on the number of subtractors n_{sub} . This leads to different parameters $\{\kappa, \Gamma, \gamma_D\}$ for each choice of n_{sub} , as listed below.

We aligned the control and probe beam with the (up to) three superatoms. Contrary to the setup in chapter 3, we here used co-propagating beams, as this leads to higher γ_D . Before we discuss the experimental results, it should be noted that all numerical calculations in this section were performed by N. Stiesdal and H. Busche, co-authors of the article [92] on which this chapter is based.

Figure 5.4 shows the intensity for the transmitted light field for $n_{\text{sub}} \in \{1, 2, 3\}$ and for $R_{\text{in}} \approx 1 \mu\text{s}^{-1}$ (top row), $R_{\text{in}} \approx 5 \mu\text{s}^{-1}$ (middle), and $R_{\text{in}} \approx 10 \mu\text{s}^{-1}$ (bottom). This provides the first experimental verification of our previous discussion, as we find that the transmission signal only reaches the intensity of the input field for sufficiently large input rates and pulse durations, which then indicates that all superatoms are dephased into the dark state and no longer interact with

5 Photon subtraction with cascaded superatoms

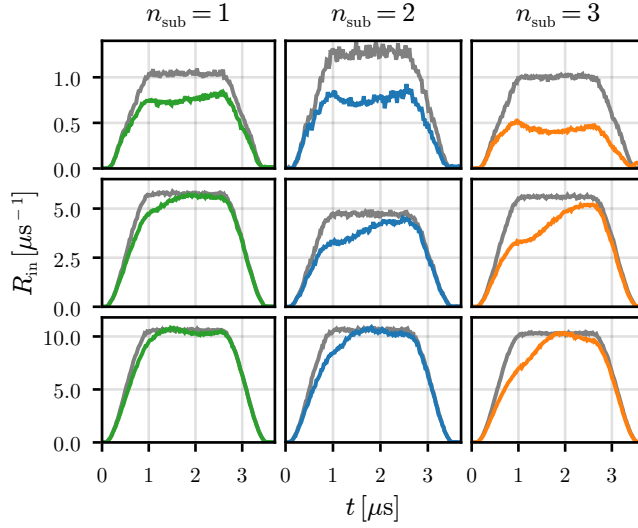


Figure 5.4

Transmitted light intensity for 1 (left), 2 (middle), and 3 (right) superatoms and for different input intensities, indicated by the grey lines.

the input field. As one would expect, the required pulse duration and R_{in} for saturating all superatoms increases with the number of superatoms. Assuming that every superatom for fixed n_{sub} is described by the same set of parameters, we may fit the superatom master equation (2.21) to the transmitted intensity and obtain $\{\kappa, \Gamma, \gamma_D\} = \{0.49, 0.045, 2.3\} \mu\text{s}^{-1}$ for $n_{\text{sub}} = 1$, $\{0.33, 0.020, 3.2\} \mu\text{s}^{-1}$ for $n_{\text{sub}} = 2$, and $\{0.35, 0.040, 2.4\} \mu\text{s}^{-1}$ for $n_{\text{sub}} = 3$.

Figure 5.5 shows the measured number of transmitted photons versus the number of input photons $\langle n_{\text{in}} \rangle = \int R_{\text{in}} dt$. As previously predicted, we find that each superatom approximatively removes one photon from the input beam for sufficiently strong input rates. The critical input strength seems to be $\langle n_{\text{in}} \rangle \approx 10$. At larger $\langle n_{\text{in}} \rangle$ we see an increased chance for additional photon losses, which we contribute to the Raman decay. Overall, we find an excellent agreement between the experiment and the theoretical predictions.

In addition, we verified that the subtracted photons were shelved into Rydberg

5.2 Experimental results and scaling to multiple superatoms

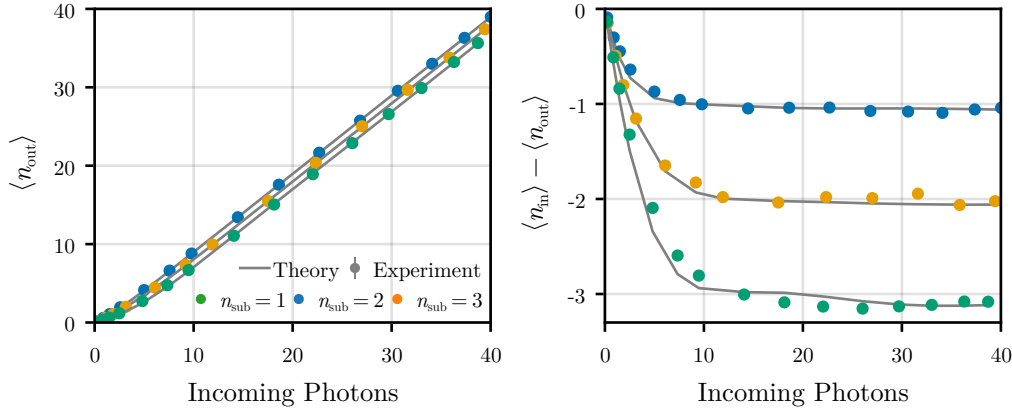


Figure 5.5

Measured number of transmitted photons (left) and the number of subtracted photons (right). Theory curves are predictions from the master equation. The error bars on the experimental data (statistical variance) are smaller than the data points.

dark states by performing field ionisation measurements. For this, we ionised the atoms in the Rydberg state $|r\rangle$ and detected the number of ionisation events on a multi-channel plate. We could resolve which superatom produced the respective ion through the time-of-flight measurements. The detection efficiency η of the multi-channel plate ranged between 0.18 and 0.25, depending on the position of the superatoms.

Figure 5.6 (a) shows the mean number of detected ions for $n_{\text{sub}} = 3$, which approximately saturates at $\langle n_{\text{ions}} \rangle \approx \eta$ for $\langle n_{\text{in}} \rangle > 10$ per superatom, thus indicating that each superatom shelved one photon into its dark state manifold. A second metric for the dark state population is the Mandel- Q parameter

$$Q = \frac{\Delta^2 n_{\text{ions}}}{\langle n_{\text{ions}} \rangle} - 1. \quad (5.10)$$

The Mandel- Q parameter gives insight into the underlying absorption statistic with $Q = 0$ for a Poissonian process, and $Q < 0$ for a sub-Poissonian process.

5 Photon subtraction with cascaded superatoms

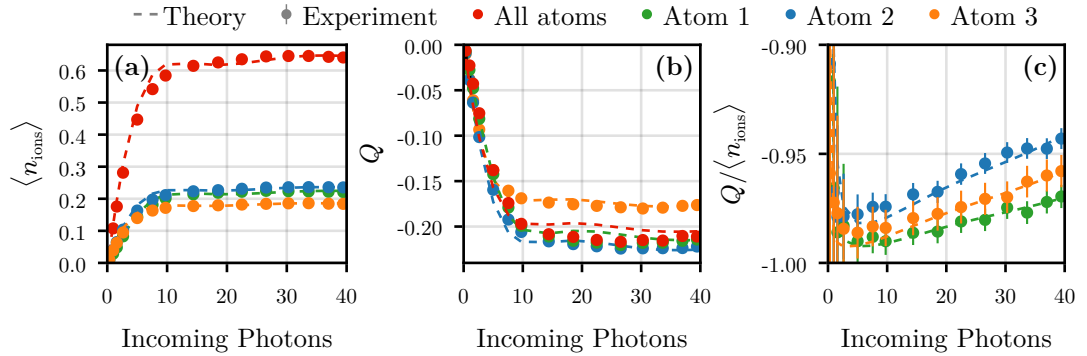


Figure 5.6

(a) Mean detected number of ions following the field ionisation for $n_{\text{sub}} = 3$ for different number of input photons. The red points show the combined signal. Curves are the dark state populations from the master equation, reduced by the respective detection efficiency η . (b) Mandel- Q parameter against the number of incoming photons for each superatom and for the combined signal. The dashed curves were produced from the Monte-Carlo model. (c) Ratio of the Mandel- Q parameter and $\langle n_{\text{ion}} \rangle$. The theory curves stem again from the Monte-Carlo model. The error bars represent the statistical variance.

For perfect absorption, we expect $Q = -\eta$, which we find to good precision in our setup, as verified by figure 5.6 (b). Lastly, due to the behaviour of the Mandel- Q parameter, we may expect $Q / \langle n_{\text{ion}} \rangle = -1$. In figure 5.6 (c), we find slight deviations from this, which increase with the number of input photons. We explain this by secondary Rydberg excitation, which can occur when sufficiently many photons are present. This is verified by a Monte-Carlo model, in which each input photon has a chance p_1 to be absorbed by a superatom and bring it into the Rydberg state or create a secondary excitation with probability $p_2 \cdot \langle n_{\text{in}} \rangle$. Fitting this simple model to the experimental results yields the dashed lines in figure 5.6 (b) and (c), which agree well with the experimental values. We further motivate and discuss the Monte-Carlo model in appendix 5.B of this chapter.

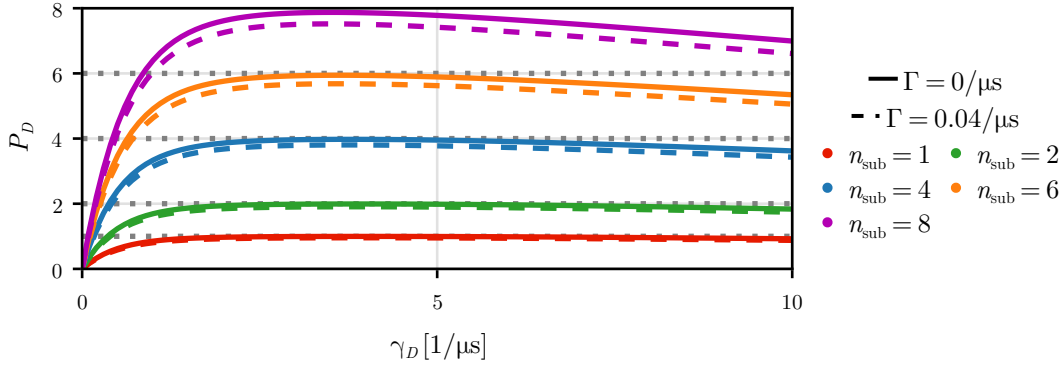


Figure 5.7

Total dark state population for superatom chains of up to $n_{\text{sub}} = 8$ subtractors versus γ_D after a constant drive at $R_{\text{in}} = 5$ photons/ μs and $\tau = 4$ μs . Solid and dashed lines show results for no Raman decay and $\Gamma = 0.04$ μs^{-1} , respectively.

5.2.2 Scaling to multi-photon subtractors

So far, we have fully analysed the dynamics of a single-photon subtractor and discussed the experimental realisation of a chain of up to 3 subtractors. We now want to end this chapter by showing that our subtractor setup scales well to even larger systems with more superatoms.

This can be seen in figure 5.7 where we show the total dark state population $P_D = \sum_j P_D^{(j)}$ for systems of up to $n_{\text{sub}} = 8$ subtractors, with the dark state population $P_D^{(j)}$ of the j -th superatom. In the presented example, with $\langle n_{\text{in}} \rangle = 20$, we find that near-optimal photon subtraction is always possible. However, we also see that the γ_D -range for which almost all superatoms are excited narrows with increasing n_{sub} . This is expected, as, with $n_{\text{sub}} = 8$, almost half of all incoming photons are absorbed. Therefore, we should assume that the chain's last superatom is in the weak R_{in} regime, where the choice of γ_D matters more than for large R_{in} , as we saw in figure 5.2.

Additionally, we find that increasing Γ to the experimental value barely affects the dark state population. However, the Raman losses are additive in the number

of superatoms, and, as we already saw, the uncertainty in the number of lost photons can become substantial. We cannot exactly quantify the impact of the Raman decay as before since our simulations were limited by the size of the superatom Hilbert space. However, we saw in figure 5.3 that the uncertainty for a single superatom at $t = 4$ is about $\Delta N_{\text{Raman}} \approx 0.33$, and we can extrapolate an uncertainty of about 2.6 photons for $n_{\text{sub}} = 8$ superatoms. Hence, deterministic multi-photon subtraction necessitates improvements in the Raman decay rate.

Appendix: Bright and dark state population for a single input photon

5.A

In this section we derive exact expressions for the bright and dark state population of a single superatom for an initial single-photon state. For this we consider the full dynamics of the photon field, i.e., we work with the Hamiltonian

$$H = H_{\text{Ph}} + H_{\text{int}} \quad (5.11)$$

where H_{Ph} is the Hamiltonian of the free photon propagation (2.4) and H_{int} describes the photon-superatom interaction (2.5). We also consider the dephasing of the superatom into the dark state, given by the dissipator

$$\gamma_D \mathcal{D}_{|D\rangle\langle W|}[\rho] = \gamma_D \left(|D\rangle\langle W| \rho |W\rangle\langle D| - \{ |W\rangle\langle W|, \rho \} / 2 \right). \quad (5.12)$$

From the dissipator we directly find for the superatom's dark state population

$$\dot{\rho}_{DD} = \gamma_D \rho_{WW}, \quad (5.13)$$

with $\rho_{ab} = \langle a | \text{Tr}_{\text{Ph}}[\rho] | b \rangle$. Thus, we obtain the dark state population by integrat-

5.A Bright and dark state population for a single input photon

ing the bright state population. Next, we go into a quantum jump trajectory formulation [109]. Here we add the anti-commutator part of the dissipator (5.12) to the Hamiltonian (5.11) and obtain the effective Hamiltonian

$$H_{\text{eff}} = H - \frac{i}{2}\gamma_D|W\rangle\langle W|. \quad (5.14)$$

In the quantum jump description of open quantum systems we evolve the initial wave function $|\psi_{\text{in}}\rangle$, instead of the density matrix ρ , under the action of H_{eff} . As H_{eff} is non-hermitian it does not conserve the norm and when the norm falls below the threshold $|\langle\psi(t)|\psi(t)\rangle| \leq p$, with $0 < p < 1$, we say that a quantum jump occurred and set $|\psi(t)\rangle = |D\rangle$. We then obtain the full density matrix ρ by averaging each $|\psi(t)\rangle\langle\psi(t)|$, the *quantum trajectory*, over a uniform distribution of p .

The advantage of this formulation is that H_{eff} only acts on the $\{|G\rangle, |W\rangle\}$ manifold of the superatom. More precisely, H_{eff} equals the full Hamiltonian of our Bethe approach, with an additional imaginary dephasing of $-i\gamma_D/2$. The dephased problem was also solved by the Bethe Ansatz [95] and the solutions are qualitatively similar to what we have seen before. For example, in the single-excitation sector, we find the eigenstate

$$|\lambda\rangle = \frac{1}{\sqrt{2\pi}} \int dy \frac{\lambda + i\gamma_D/2 - (i\kappa/2) \text{sgn}(y)}{\lambda + i\gamma_D/2 + i\kappa/2} e^{i\lambda y} r^\dagger(y, \lambda) |0\rangle. \quad (5.15)$$

with $r(y, \lambda) = b^\dagger(y) - \sqrt{\kappa}\sigma^+\delta(y)/(\lambda + i\gamma_D/2)$.

We can determine the full time evolution of our input state (5.2) by projecting on the eigenstates of H_{eff} . This gives

$$\langle\lambda|\psi_{\text{in}}\rangle = \frac{1}{\sqrt{2\pi}} \frac{\sqrt{\kappa - \gamma_D}}{i\lambda - \gamma_D/2 + \kappa/2} \quad (5.16)$$

and we thus find the amplitude to be in the bright state

$$\begin{aligned}
 c_W(t) &= \langle W | \psi(t) \rangle = \int_{-\infty}^{\infty} d\lambda e^{-i\lambda t} \langle W | \lambda \rangle \langle \lambda | \psi \rangle \\
 &= i \int_{-\infty}^{\infty} \frac{d\lambda}{2\pi} e^{-i\lambda t} \frac{\sqrt{\kappa} \sqrt{\kappa - \gamma_D}}{(\lambda - i\kappa/2 + i\gamma_D/2)(\lambda + i\gamma_D/2 + i\kappa/2)} \\
 &= \begin{cases} i \sqrt{\frac{\kappa - \gamma_D}{\kappa}} e^{(\kappa - \gamma_D)t/2} & t \leq 0 \\ i \sqrt{\frac{\kappa - \gamma_D}{\kappa}} e^{-(\kappa + \gamma_D)t/2} & t \geq 0 \end{cases}. \tag{5.17}
 \end{aligned}$$

This then directly leads to the bright state population $P_W(t) = |c_W(t)|^2$ and, by integration of (5.13), the dark state population.

Appendix: Monte-Carlo Model

5.B

In the main part of this chapter we used a classical Monte-Carlo model of the photon-superatom interaction, in order to describe the statistical nature of the ion detection in the presence of secondary Rydberg excitations. In this section we will motivate this model from a microscopic analysis and describe it in more detail.

First, we assume that the photons are in a quenched plane wave, which arrives at time $t = 0$ at the position of the superatom, i.e., $\psi_{\text{in}}(x) = 1$ for $x < 0$ and $\psi_{\text{in}}(x) = 0$ for $x > 0$. The projection onto the single-excitation Bethe state then is

$$\langle \lambda | \psi_{\text{in}} \rangle = \sqrt{2\pi} \delta(\lambda) \tag{5.18}$$

and we find, for $x > 0$,

$$\psi_{\text{out}}(x) = \lim_{t \rightarrow \infty} \psi_{\text{in}}(x, t) = \frac{\gamma_D - \kappa}{\gamma_D + \kappa}. \tag{5.19}$$

Therefore, according to the quantum jump trajectory description, we find the probability $p_1 = (\gamma_D - \kappa)^2 / (\gamma_D + \kappa)^2$ that the incoming photon gets transmitted.

For the multi-photon scattering the Bethe Ansatz again shows that the outgoing state is a combination of individually scattered photons and multi-photon bound states. Now, if we assume well-separated photons, we may neglect the photonic bound states and find that each photon scatters independent of the others, with a probability of $1 - p_1$ to be absorbed into the dark state, if the superatom is not yet dephased. Importantly, we saw in (5.19), that the scattering of a resonant plane wave does not alter the wave function, so this analysis carries over to multiple superatoms and each superatom has the same probability $1 - p_1$ to absorb an incoming photon.

In order to arrive at our full Monte-Carlo model, we additionally allow for secondary Rydberg excitations. For this we heuristically introduce the photon-number dependent probability $p_2 \cdot \langle n_{\text{in}} \rangle$ to excite the superatoms into an additional dark state. Interestingly, this simple model already captures the superatom dynamics quite well and, even though we assumed well-separated photons above, it reproduces the experiment results even for large $\langle n_{\text{in}} \rangle$.

6

Nonexponential decay in multiple-emitter chains

At this point, we have a clear understanding of the interaction of light with a single superatom. Regarding the transmitted photons, we analysed the temporal and number statistics in chapters 3 and 4, respectively. Furthermore, the discussion of the parameter dependence of the single-photon subtractor in the last chapter 5 equates to a full analysis of the single-superatom dynamics.

Systems of a few superatoms show a modified behaviour due to the chiral exchange interaction between superatoms. As an example, we saw the breakdown of well-defined Rabi oscillations for a superatom chain or that a two-superatom system may become completely trivial with regard to the photon transmission, as discussed in section 4.3. The exchange interactions thus have a substantial impact on the superatoms and photon dynamics.

In this chapter, we will study a waveguide of N emitters, where the influence of the coherent exchange interaction becomes increasingly dominant. For this, we will study the decay of a single excitation: the collective bright state of the emitter chain, i.e., the state of the chain immediately after the absorption of a single resonant photon. This discussion follows the same underlying idea as

our derivation of the internal dynamics of the superatom in section 1.3. More precisely, the external light field couples to the emitter chain via the collective jump operator $\sigma^+ = \sum_j \sigma_j^+ e^{ik_0 x_j}$, resulting in the *collective bright state*

$$|W\rangle = \frac{1}{\sqrt{N}} \sum_{j=1}^N e^{ik_0 x_j} \sigma_j^+ |G\rangle, \quad (6.1)$$

where $|G\rangle = |G_1, \dots, G_N\rangle$ denotes the collective ground state, $|G_j\rangle$ is the ground state of the j -th emitter, and $k_0 = \omega_0/c$ is the wave vector at the resonance frequency ω_0 of the emitters.

Our discussion here possesses strong ties to the similar setup of the collective decay of three-dimensional systems [70, 72, 76, 77, 79–81, 195]. In these systems, superradiant emission of the excitation was predicted [72, 76] and subsequently measured in multiple different platforms, like cavity-trapped atoms [196], cold atoms [197–200], and quantum dots [201, 202]. Furthermore, the light-emitter interaction results in a **cooperative** Lamb-Shift of the emitters [71, 203, 204], again observed in multiple different systems [196, 205–207]. Lastly, as we already discussed in section 1.3.3, directed emission is another emerging effect in these systems [55, 75, 78, 208], as observed in cold atoms [209] or Rydberg superatoms [90].

The one-dimensional system discussed here will be similar to these three-dimensional systems in many ways. We will see that $|W\rangle$ is the superradiant state of the chiral waveguide, with the correspondingly enhanced decay. However, only the initial decay occurs at the superradiant decay rate $N\kappa$, after which the coherent exchange interactions slow down the decay to subradiant levels. More specifically, we find that, for multiple emitters, the asymptotic decay of $|W\rangle$ transitions from an exponential into an algebraic decay.

Furthermore, we will contrast the chiral interaction against the interactions in a bidirectional waveguide, which we will introduce in this chapter. Interestingly, we

will find little qualitative differences between a chiral waveguide and an extended bidirectional waveguide. On the other hand, we will find pure superradiant decay for bidirectional waveguides smaller than the wavelength of a resonant photon.

This chapter is based on the publication [210], for which the manuscript's author performed the first derivation of the algebraic decay of the N emitters chain, using the Bethe Ansatz. Calculations based on the master equation were performed by the co-author of the publication J. Kumlin unless stated otherwise.

The bidirectional waveguide

6.1

An extension of our theory to bidirectional emitters is straightforward and only requires two modifications to our previous derivation of the master equation. When we derived the master equation (2.22), we split the free-photon propagation Hamiltonian (2.2) into two modes b_L and b_R , for the left and right moving photons, respectively. We then dropped one mode as it was generally unimportant for chiral interactions. For a bidirectional waveguide, we have to take both modes into account. This requires that the second mode enters the interaction Hamiltonian (2.5) in the same way as the first mode. We also need to account for the phase factor $e^{\pm ik_0 x_j}$, which we previously included in the definition of the ladder operators $\sigma_j^- e^{-ik_0 x_j} \mapsto \sigma_j^-$. This is no longer possible, as the sign in the phase differs for the left- and right-moving photons.

There are no additional steps required in the derivation of the bidirectional master equation compared to the chiral one. The articles [101, 102], for example,

contain detailed derivations and the bidirectional master equation becomes

$$\begin{aligned} \partial_t \rho = & -i \left[\sum_{j,l} \kappa \sin(k_0 |x_j - x_l|) \sigma_l^+ \sigma_j^-, \rho \right] \\ & + 2\kappa \sum_{j,l} \cos(k_0 |x_j - x_l|) \left(\sigma_j^- \rho \sigma_l^+ - \frac{1}{2} \{ \sigma_l^+ \sigma_j^-, \rho \} \right). \end{aligned} \quad (6.2)$$

Notice that for the chiral waveguide, only the collective mode $\sigma^+ = \sum_j \sigma_j^+ e^{ik_0 x_j}$ occurred in the dephasing, while the dephasing here generally acts on many orthogonal emitter modes.

In order to better compare between both the chiral and the bidirectional waveguide, let us introduce the more general notation for the master equation

$$\partial_t \rho = -i \left[\sum_{j,l} J_{jl} \sigma_l^+ \sigma_j^-, \rho \right] + \sum_{j,l} \Gamma_{jl} \left(\sigma_j^- \rho \sigma_l^+ - \frac{1}{2} \{ \sigma_l^+ \sigma_j^-, \rho \} \right), \quad (6.3)$$

where J_{jl} describes the coherent interaction between the superatoms and Γ_{jl} the correlated decay. For a chiral waveguide, including the phase factors, this yields

$$J_{jl} = \frac{\kappa}{2i} \text{sgn}(x_j - x_l) e^{ik_0(x_j - x_l)}, \quad (6.4a)$$

$$\Gamma_{jl} = \kappa e^{ik_0(x_j - x_l)}. \quad (6.4b)$$

We call the eigenstates of the dephasing Γ_{jl} *superradiant* if they decay faster than κ or *subradiant* for a slower decay.

Decay of two emitters

6.2

As an instructive example we first discuss the minimal model of two emitters, for which we will see the first relevant effects of to the coherent exchange interaction.

For the generic master equation (6.3) we find the superradiant and subradiant states

$$|\pm\rangle = \frac{1}{\sqrt{2}}(\sigma_1^\dagger \pm e^{-i\varphi}\sigma_2^\dagger)|G\rangle \equiv S_\pm^\dagger|G\rangle, \quad (6.5)$$

where $\varphi = \arg(\Gamma_{12}/\Gamma_{11})$ and we used that Γ is a symmetric matrix with $\Gamma_{11} = \Gamma_{22}$ for both types of waveguides. The super- and subradiant states decay with the respective rates $\Gamma_\pm = \Gamma_{11} \pm |\Gamma_{12}|$. Thus, for the bidirectional waveguide, we find the position-dependent decay rates $\Gamma_\pm = 2\kappa[1 \pm |\cos(k_0|x_1 - x_2|)]$ while, for the chiral waveguide, only the superradiant state decays with rate 2κ and the subradiant state is free of dissipation. In the extreme cases, at atom separations of $k_0|x_1 - x_2| = \pi n$, $n \in \mathbb{Z}$, the bidirectional waveguide's decay rates are twice as large as for the chiral waveguide since there are two possible directions for the photon emission.

The super- and subradiant states diagonalise the decay of the emitters. However, these states are not necessarily eigenstates of the exchange interaction, thus the time evolution will mix these different states, and the overall decay will be a combination of all available decay rates. Additionally, for the chiral waveguide, the superradiant state always equals the collective bright state $|W\rangle$, while in the bidirectional waveguide $|W\rangle$ generally becomes a superposition of the super- and subradiant states, except for very fine-tuned emitter positions x_j . Hence, the decay of the collective bright state requires a thorough analysis.

6.2.1 Bidirectional waveguide

First, we analyse the bidirectional waveguide, where, only in the special case of two atoms, the exchange interaction becomes diagonal in the super- and subradiant basis, and the master equation reads as

$$\partial_t \rho = -i[J_{12}(S_+^\dagger S_+ - S_-^\dagger S_-), \rho] + \Gamma_+ \mathcal{D}_{S_+}[\rho] + \Gamma_- \mathcal{D}_{S_-}[\rho], \quad (6.6)$$

6 Nonexponential decay in multiple-emitter chains

where $J_{12} = \kappa \sin(k_0|x_1 - x_2|)$, $\Gamma_{\pm} = 2\kappa(1 \pm \cos(k_0|x_1 - x_2|))$ and S_{\pm}^{\dagger} creates the super- and subradiant states, respectively. From the diagonal form of the master equation (6.6) we directly see that the super- and subradiant state decay with a rate of $\pm J_{12} - \Gamma_{\pm}/2 = \kappa[1 \pm \exp(ik_0|x_1 - x_2|)]$ and we find the time evolution of of the bright state population

$$P_W(t) = e^{-2\kappa t} \left| \cosh(\kappa t e^{ik_0|x_1-x_2|}) - \cos(k_0(x_1 - x_2)) \sinh(\kappa t e^{ik_0|x_1-x_2|}) \right|^2, \quad (6.7)$$

by expressing $|W\rangle$ in the $|\pm\rangle$ basis. In the same way we obtain the population of the state orthogonal to $|W\rangle$, denoted as $|D\rangle$ to make the similarity to our Rydberg superatoms discussed in section 1.3.5 more stringent,

$$P_D(t) = e^{-2\kappa t} \left| \sin(k_0(x_1 - x_2)) \sinh(\kappa t e^{ik_0|x_1-x_2|}) \right|^2. \quad (6.8)$$

The dark and bright state populations are clearly position-dependent. If we control the atom position perfectly, we can alter the dynamics in many ways. For example, for atom separations commensurable to the photon wavelength $k_0(x_1 - x_2) = \pi n$, $n \in \mathbb{Z}$, the dark state will never be populated, and we obtain perfect super- and subradiance, $\Gamma_+ = 2N\kappa$, $\Gamma_- = 0$. In contrast, for the rest of this chapter, we want to focus on a random atom distribution, and we subsequently want to study the average decay of $|W\rangle$.

First, let us assume that the atoms are positioned within one wavelength of each other, $k_0\sigma \ll 1$, where σ is a characteristic width of the atom distribution. We may then approximate $k_0|x_1-x_2| \approx 0$. In this limit, the bright state coincides with the superradiant state $|W\rangle = |+\rangle$ and, consequently, we find superradiant decay $P_W(t) = \exp(-4\kappa t) = \exp(-2N\kappa t)$, i.e., both emitters contribute constructively to the decay, and the factor 2 comes from the two available decay directions.

In contrast, for broad distribution $k_0\sigma \gg 1$ the phase factors $\exp(ik_0(x_1 - x_2))$ become almost uniformly distributed on the unit circle and the collective decay

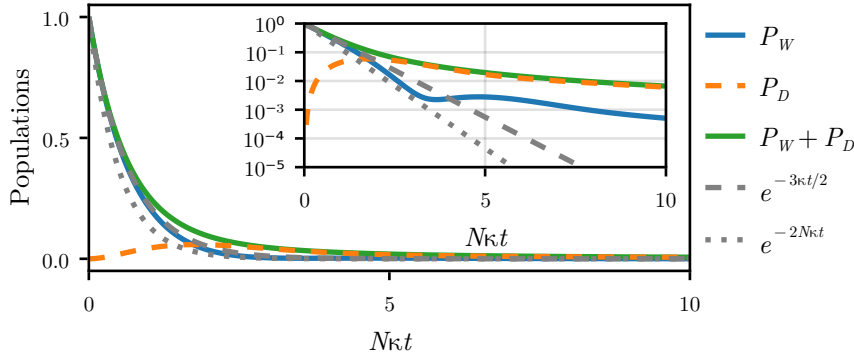


Figure 6.1

Bright state, dark state, and total population of two atoms with bidirectional emission. The bright state decays slower as the single-photon superradiant decay rate $2N\kappa$ (grey, dotted line), which we found for closely packed atoms. The dipole-dipole interaction increases the dark state population on short times, which becomes the dominant contribution to the total population. From then on, the decay is dominated by the slower subradiant decay. The inset shows the time evolution on a logarithmic scale. We assumed a Gaussian atom distribution of mean 0 and variance σ^2 with $k\sigma = 1000$ and averaged over 1000 realisations. The statistical error is smaller than the line width.

effects are damped, as can be seen from the position-averaged initial decay

$$P_W(t) = 1 - 3\kappa t + \mathcal{O}((\kappa t)^2) \approx e^{-3\kappa t/2}, \quad (6.9)$$

$$P_D(t) = \frac{1}{2}(\kappa t)^2 + \mathcal{O}((\kappa t)^3). \quad (6.10)$$

The reasons for the slowed decay are twofold. On the one hand, for arbitrary atom positions, the superradiant decay rate will not obtain its largest value $2N\kappa$, and the decay is limited by Γ_+ . On the other hand, while we had $|W\rangle \approx |+\rangle$ in the $k_0\sigma \rightarrow 0$ limit, the bright state now also overlaps with the subradiant state $|-\rangle$ and the long-term evolution is dominated by the slow, subradiant decay Γ_- . We find this discussion verified by the numerical results displayed in figure 6.1, where we show the time evolution of bright, dark, and total population. Here

we assumed a Gaussian atom distribution at $k_0\sigma = 1000$, but it should be noted that the exact distribution is irrelevant as long as it is almost constant on length scales $1/k_0$ and the variance is sufficiently large $k_0\sigma \gg 1$.

6.2.2 Chiral waveguide

Now we turn to the chiral waveguide where the atoms only emit in one direction. Before going into a full analysis of the bright state dynamics, we can already name a few important differences to the bidirectional waveguide by comparing the respective coupling and decay coefficients (6.2) and (6.4). Firstly, as we have done in the previous chapters, the emitter positions may be absorbed into the ladder operators $\sigma_j^+ e^{ik_0x_j} \mapsto \sigma_j^+ m$ and the dynamic only depends on the relative ordering of the atoms, which we fix to $x_1 < x_2$. Secondly, we find that the bright state is the superradiant state with decay rate $\Gamma_+ = 2\kappa = N\kappa$, while the dark state is subradiant and without decay. Consequently, every deviation from a pure $\exp(-N\kappa t)$ decay has to be attributed to the impact of the dipole-dipole interactions.

Now, the density matrix for the chiral waveguide in the dark and bright state basis becomes

$$\partial_t \rho = -i \left[i \frac{\kappa}{2} (S_W^\dagger S_D - S_D^\dagger S_W), \rho \right] + \Gamma_+ \mathcal{D}_{S_W}[\rho], \quad (6.11)$$

where $S_{W,D}^\dagger = (\sigma_1^\dagger \pm \sigma_2^\dagger)/\sqrt{2}$ create the bright and dark state, respectively. As opposed to the bidirectional waveguide, where we had no coupling between the super- and subradiant states, the dipole-dipole interaction is now purely off-diagonal in this basis. Therefore, the initial bright state population will transition into the dark state, which is non-radiating and therefore slow down the decay process.

More precisely, the bright and dark state populations for the decay of the

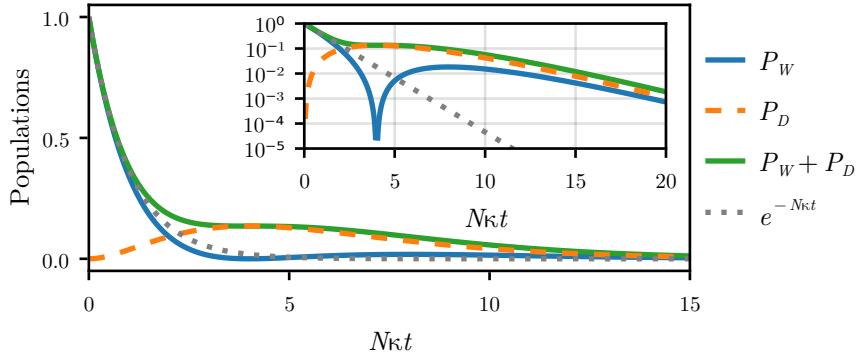


Figure 6.2

Bright state, dark state, and total population for two chiral emitters. Initially, the bright state follows a superradiant decay $\exp(-N\kappa t)$, indicated by the grey dotted line. At time $\kappa t = 2$ the entire remaining emitter population is shelved into the dark state, $P_W = 0$, after which the emitters undergo a damped decay of $\exp(-\kappa t)$.

bright state become

$$P_W(t) = \frac{1}{4}e^{-\kappa t}(\kappa t - 2)^2, \quad (6.12)$$

$$P_D(t) = \frac{1}{4}e^{-\kappa t}(\kappa t)^2. \quad (6.13)$$

For short times we find that the bright state decay is dominated by the superradiant decay, as $P_W(t) = 1 - 2\kappa t + \mathcal{O}((\kappa t)^2) \approx \exp(-2\kappa t)$. Additionally, we find a complete transition into the dark state at $\kappa t = 2$. After the transition, the effective decay rate decreases to $\exp(-\kappa t)$ as the bright state first has to be repopulated from the dark state through the dipole-dipole interaction. These results are clearly visible in figure 6.2, which shows the bright state, dark state, and total population of the two-emitter chiral waveguide.

Decay of multiple atoms

6.3

The discussion on the two-emitter waveguides revealed how the coherent exchange interaction generally slows down the decay of the collective bright state. Especially for the chiral waveguide, we observed that the initial superradiant decay $\exp(-N\kappa t)$ was reduced to an asymptotic single-emitter decay $\exp(-\kappa t)$. We will now discuss the generic situation for an arbitrary number N of emitters. Here we will see that, after an initial superradiant decay, the complex interplay between the bright state and the multiple dark states leads to oscillations in the bright state population with an overall algebraic decay. We will now first discuss the chiral waveguide, for which we can find analytic results for the decay of the collective bright state. Then we turn to the bidirectional waveguide, where we find the same qualitative results for broad distributions $k_0\sigma \rightarrow \infty$.

6.3.1 Chiral waveguide

For the general N -emitter chiral waveguide, our previous two observations are still valid: As only the relative ordering of the emitters enter the master equation, the decay of the collective bright state $|W\rangle$ is independent of the emitter position and $|W\rangle$ is the superradiant state with decay rate $\Gamma = N\kappa$, while all orthogonal states are non-radiating dark states. Different to the two-emitter waveguide, however, the bright state now has $N - 1$ potential dark states to shelve its excitation into, which will reduce the bright state decay to an algebraic $(\kappa t)^{-3/2}$ decay, and the total population decays as $(\kappa t)^{-1/2}$ for intermediated times, as we will now show.

In the appendix 6.A of this chapter, we analytically derive the full time evolution of each atom in the chiral waveguide. From this we then directly find

the exact expressions for the bright state population

$$P_W(t) = \frac{1}{N^2} e^{-\kappa t} [L_{N-1}^{(1)}(\kappa t)]^2 \quad (6.14)$$

and the total population of the emitter chain

$$P_{\text{total}} = e^{-\kappa t} [L_{N-1}^{(0)}(\kappa t)L_N^{(0)}(\kappa t) - L_{N-1}^{(1)}(\kappa t)L_N^{(-1)}(\kappa t)]. \quad (6.15)$$

Here $L_N^{(\alpha)}(x)$ denotes the generalised Laguerre polynomials of degree N .

Let us first discuss the decay of the bright state population. For short times we again find superradiant decay, since

$$P_W(t) = 1 - N\kappa t + \mathcal{O}((\kappa t)^2) \approx e^{-N\kappa t}. \quad (6.16)$$

Additionally, as $L_N^{(1)}(x) \rightarrow (-x)^N/N!$ for $x \rightarrow \infty$, the bright state decay is again dominated by uncorrelated single-emitter decay in the asymptotic limit $t \rightarrow \infty$. However, for intermediate times $1 \ll \kappa t \ll N$, the coherent exchange interaction leads to a complex interplay of the bright state and the multiple dark states, that drastically alters the decay of the collective bright state. This becomes evident, as we find the asymptotic bright state population for many atoms $N \rightarrow \infty$ and fixed $N\kappa$

$$P_W(t) = \frac{[J_1(2\sqrt{N\kappa t})]^2}{N\kappa t}, \quad (6.17)$$

where $J_n(x)$ is the Bessel function of the first kind. We now find, for $\kappa t \gg 1$, the algebraic behaviour

$$P_W(\kappa t \gg 1) \approx \frac{1}{\pi(N\kappa t)^{3/2}} \cos^2 \left(2\sqrt{N\kappa t} - \frac{3\pi}{4} \right). \quad (6.18)$$

Interestingly, the multiple dark states do not lead to some self-averaging behaviour but instead the bright state population has perfect absorption into the

6 Nonexponential decay in multiple-emitter chains

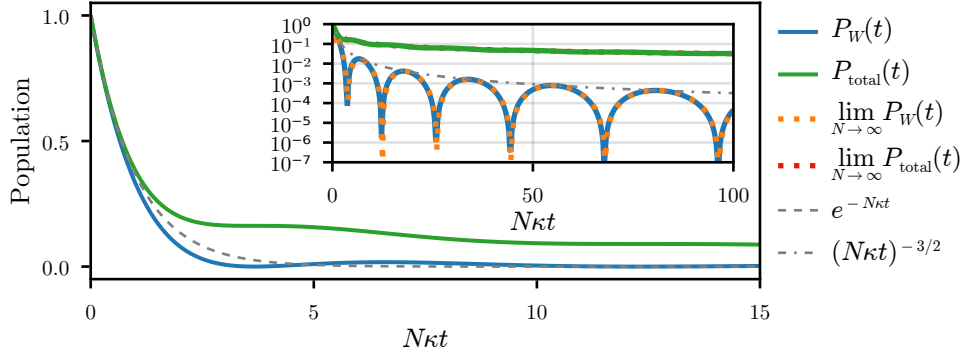


Figure 6.3

Bright state and total population for a chiral waveguide of $N = 1000$ emitters. The inset shows the populations on a logarithmic scale, together with the asymptotic results for $N \rightarrow \infty$ and fixed $N\kappa$. The grey dashed and dash-dotted lines show the superradiant short term and algebraic intermediate term behaviour of the bright state.

dark state manifold with infinitely many revivals, evident by the cosine-oscillations in P_W .

Similarly, the total population has superradiant decay for short times, while for $\kappa t \gg N$ its decay is dominated by the uncorrelated single-emitter decay. For intermediate times $1 \ll \kappa t \ll N$ in the large system limit $N \rightarrow \infty$ we obtain

$$P_{\text{total}}(\kappa t \gg 1) \approx \frac{1}{\pi \sqrt{N\kappa t}}. \quad (6.19)$$

Most noticeably, the total population decays with an even weaker power-law scaling than the bright state. Our results for the bright state and total population are summarised in figure 6.3 for 1000 emitters, and we find excellent agreement between the exact results and their $N \rightarrow \infty$ approximations.

In conclusion, we find that for short times both the bright state population and the total population show superradiant decay. This then transitions into algebraic decay with a scaling law of $(\kappa t)^{-3/2}$ for the bright state and $(\kappa t)^{-1/2}$ for

the total population. Finally, at $\kappa t \gg N$ the decay is dominated by incoherent single-atom decay. Appendix 6.A contains the derivations of the results from this section. These results were originally derived by the author of this manuscript and were his main contribution to the theoretical analysis in the article [210].

6.3.2 Bidirectional waveguide

For the final section in this chapter, we now turn to the bidirectional waveguide with multiple emitters $N \gg 1$ with a Gaussian position distribution. While an exact solution of this problem is out of reach, we find that the two limiting cases of $k_0\sigma \rightarrow \infty$ and $k_0\sigma \rightarrow 0$, are well-described by previously observed effects. Namely, for $k_0\sigma \rightarrow \infty$ we find a self-averaging effect due to the random positions of the atoms, which almost perfectly cancels the back-scattering terms and therefore leads a similar decay as in the chiral waveguide. On the other hand, for $k_0\sigma \rightarrow 0$, we again find the superradiant limit, where the collective bright state decays with the superradiant decay rate $\Gamma_+ = 2N\kappa$.

Let us first discuss the $k_0\sigma \rightarrow \infty$ limit. Figure 6.4 shows the numerical results for $N = 100$ at $k_0\sigma = 1000$ with the bright state and total population averaged over 1000 realisations¹. Interestingly, we find that the bright state and total population deviate little from the exact results for chiral waveguide, equations (6.14) and (6.15), respectively. Furthermore, this does not appear, at least entirely, to be an averaging effect from the multiple realisations, as even individual realisations show almost the same population evolution as atoms in a chiral waveguide for relatively short times $N\kappa t < 50$.

In order to explain this interesting behaviour, we analyse the time evolution in quantum jump trajectory formulation [109, 110]. Here, the effective Hamiltonian

¹Figure 6.4 uses new numerical results, explaining why the individual, random trajectories differ from the original publication. At the same time we increased the number of realisations from 100 to 1000, to make the averaging more consistent with the two-emitter discussion.

6 Nonexponential decay in multiple-emitter chains

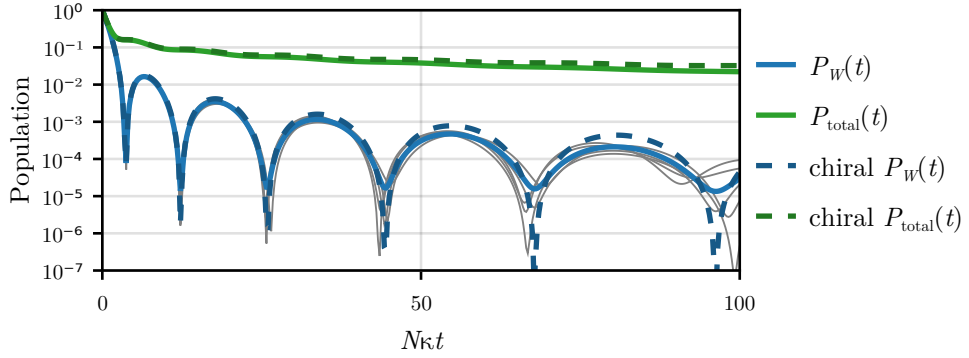


Figure 6.4

Bright state and total population in a bidirectional waveguide for $N = 100$ emitters. The emitter positions follow a Gaussian distribution with standard deviation $k_0\sigma = 1000$. The curves are averaged over 1000 realisations. The dashed lines are the respective results (6.14) and (6.15) for a chiral waveguide and closely follow the averaged curves for long times. Grey lines show individual realisations, which deviate little from the averaged curve up to $N\kappa t \approx 50$.

reads as

$$\begin{aligned}
 H_{\text{eff}} &= -i\kappa \sum_{j,l} e^{ik_0|x_j-x_l|} \sigma_l^+ \sigma_j^- \\
 &\rightarrow -iN\kappa \int dx dy e^{ik_0|x-y|} \psi^\dagger(x) \psi(y),
 \end{aligned} \tag{6.20}$$

where we employed the continuum-limit for large N in the second line, for which we kept $N\kappa$ fixed. Here $\psi^{(\dagger)}(x)$ destroys (creates) an emitter excitation at position x with bosonic exchange statistics, i.e. $[\psi(x), \psi^\dagger(y)] = \delta(x-y)$. The time evolution of the collective bright state, for a uniform atom distribution in the interval $[0, \sigma]$, now reads as

$$\partial_t \psi(x, t) = -\frac{N\kappa}{\sigma} \int_0^\sigma dy \psi(y, t) e^{ik_0|x-y|}, \tag{6.21}$$

with the initial condition $\psi(x, 0) = e^{ik_0x}$. We obtain the solution to (6.21) by two Laplace-transformations in x and t , as shown in the appendix 6.B of this chapter. Doing so, the atom state becomes

$$\psi(x, t) = e^{ik_0x} J_0(2\sqrt{N\kappa t}x/\sigma). \quad (6.22)$$

From this, we directly obtain the bright state population

$$P_W(t) = \left| \int_0^\sigma dx J_0(2\sqrt{N\kappa t}x/\sigma) \right|^2 = \frac{J_1(2\sqrt{N\kappa t})^2}{N\kappa t}, \quad (6.23)$$

which equals the bright state population of the chiral waveguide (6.14). On the other hand we find the total population

$$P_{\text{total}}(t) = \int_0^\sigma dx \left| J_0(2\sqrt{N\kappa t}x/\sigma) \right|^2 = J_0(2\sqrt{N\kappa t})^2 + J_1(2\sqrt{N\kappa t})^2, \quad (6.24)$$

which coincides with the total population (6.15) of the chiral waveguide, see (6.33). While we specifically considered a uniform emitter distribution, it should be noted that the actual distribution does not influence the results in the $k_0\sigma \rightarrow \infty$ limit.

In the $k_0\sigma \rightarrow 0$ limit, the coherent exchange interaction again becomes irrelevant $J_{ij} \approx 0$. Here, the collective bright state becomes the superradiant state of the bidirectional waveguide, and we find the superradiant decay rate $2N\kappa$, with the factor 2 again originating from the two respective decay directions. The $k_0\sigma \rightarrow 0$ limit coincides with the original work of Dicke [53], where superradiant emission from a gas of extent smaller than the wavelength of a resonant photon was first predicted.

Appendix: Exact results for the chiral waveguide

6.A

We now give the derivation of bright state population (6.14) and the total population (6.15) for the chiral waveguide. For this we calculate the transition amplitude for the exchange of an excitation from the j -th superatom to the l -th atom with $l \geq j$. We do this with the Bethe Ansatz solution as this formalism is applied straightforwardly to the problem at hand.

Let $|\psi_j\rangle = \sigma_j^+|G\rangle$. The projection of $|\psi_j(t)\rangle$ on the excited state $|\psi_l\rangle$ reads as

$$\begin{aligned} \langle \psi_l | \psi_j(t) \rangle &= \int_{-\infty}^{\infty} d\lambda e^{-i\lambda t} \langle \psi_l | \lambda \rangle \langle \lambda | \psi_j \rangle \\ &= -i\kappa^2 L_{l-j}^{(-1)}(\kappa t) e^{-\kappa t/2} \end{aligned} \quad (6.25)$$

Now we can determine the time evolution of $|W\rangle$ by summing the individual evolution of each emitter contributing to $|W\rangle$. Then, the amplitude to have the l -th atom excited becomes

$$\begin{aligned} c_l &= \langle \psi_l | W(t) \rangle \\ &= -\frac{i\kappa^2}{\sqrt{N}} \left(\sum_{j=1}^l L_{l-j}^{(-1)}(\kappa t) \right) e^{-\kappa t/2} \\ &= -\frac{i\kappa^2}{\sqrt{N}} L_{l-1}^{(0)}(\kappa t) e^{-\kappa t/2}. \end{aligned} \quad (6.26)$$

From this the bright state population (6.14) in the main text readily follows

$$P_W(t) = \left[\frac{1}{N} \sum_{j=1}^N L_{j-1}^{(0)}(\kappa t) \right]^2 e^{-\kappa t} = \left[\frac{1}{N} L_{N-1}^{(1)}(\kappa t) \right]^2 e^{-\kappa t}. \quad (6.27)$$

The probability to have any emitter excited is the squared norm of $|W(t)\rangle$, i.e.,

$$\begin{aligned} P_{\text{total}}(t) &= \frac{1}{N} \sum_{j=1}^N [L_{j-1}^{(0)}(\kappa t)]^2 e^{-\kappa t} \\ &= \left[L_{N-1}^{(0)}(\kappa t) L_N^{(0)}(\kappa t) - L_{N-1}^{(1)}(\kappa t) L_N^{(-1)}(\kappa t) \right] e^{-\kappa t} \end{aligned} \quad (6.28)$$

$$= \left[L_{N-1}^{(0)}(\kappa t) L_N^{(0)}(\kappa t) - \kappa t L_{N-1}^{(1)}(\kappa t) L_N^{(1)}(\kappa t) / N \right] e^{-\kappa t}. \quad (6.29)$$

For large N the Laguerre polynomials $L_N^{(\alpha)}(x)$ are well-approximated by Bessel functions [211]

$$L_N^{(\alpha)}(x) \approx \sqrt{N^\alpha} \frac{J_\alpha(2\sqrt{Nx})}{\sqrt{x^\alpha}} e^{x/2}. \quad (6.30)$$

Bessel functions are, for large arguments, well-approximated by an algebraic decay, superimposed with a harmonic oscillation [212]

$$J_\alpha(x) \approx \sqrt{\frac{2}{\pi x}} \cos\left(x - \frac{\alpha\pi}{2} - \frac{\pi}{4}\right). \quad (6.31)$$

Hence, for many atoms $N \gg 1$ and for times $\kappa t \gg 1$ we find the asymptotic expressions for the bright state population

$$P_W(t) \approx \frac{1}{\pi \sqrt{(\kappa N t)^3}} \cos^2\left(2\sqrt{\kappa N t} - \frac{3\pi}{4}\right), \quad (6.32)$$

and for the total population

$$P_{\text{total}}(t) = J_0(2\sqrt{N\kappa t})^2 + J_1(2\sqrt{N\kappa t})^2 \approx \frac{1}{\pi \sqrt{\kappa N t}}. \quad (6.33)$$

Appendix: Exact results for the bidirectional waveguide

6.B

In this section we show the detailed derivation of the time evolution of the bidirectional waveguide in the continuum-limit. For $N \rightarrow \infty$ with fixed $N\kappa$ the continuum limit is given by the effective Hamiltonian (6.20), with field creation and annihilation operators $\Psi^\dagger(x)$ and $\Psi(x)$, respectively. In this description the collective bright state becomes

$$|W\rangle = \frac{1}{\sqrt{N}} \int dx e^{ik_0x} \Psi^\dagger(x) |G\rangle . \quad (6.34)$$

Now we determine the time evolution, which follows the Schrödinger equation

$$i\partial_t \psi(x, t) = -i \frac{N\kappa}{\sigma} \int_0^\sigma dy e^{ik_0|x-y|} \psi(y, t), \quad (6.35)$$

with the initial condition $\psi(x, 0) = e^{ik_0x}$. In order to solve this differential equation, we first apply a Laplace transformation from the variable t to the variable s

$$\begin{aligned} s\hat{\psi}(x, s) - \psi(x, 0) &= -\frac{N\kappa}{\sigma} \int_0^\sigma dy e^{ik_0|x-y|} \hat{\psi}(x, s) \\ &= -\frac{N\kappa}{\sigma} \int_0^x dy e^{ik_0(x-y)} \hat{\psi}(x, s) - \frac{N\kappa}{\sigma} \int_x^\sigma dy e^{-ik_0(x-y)} \hat{\psi}(x, s) \\ &= -\frac{N\kappa}{\sigma} \int_0^x dy e^{ik_0(x-y)} \hat{\psi}(y, s) + \frac{N\kappa}{\sigma} \int_0^x dy e^{-ik_0(x-y)} \hat{\psi}(y, s) \\ &\quad - \frac{N\kappa}{\sigma} \int_0^\sigma dy e^{-ik_0(x-y)} \hat{\psi}(y, s). \end{aligned} \quad (6.36)$$

To better suite the initial conditions and to identify fast oscillating terms, we make the Ansatz $\hat{\psi}(x, s) = e^{ik_0x} \hat{\phi}(x, s)$. Under this replacement, equation (6.36)

simplifies to

$$s \hat{\phi}(x, s) - 1 = -\frac{N\kappa}{\sigma} \int_0^x dy \hat{\phi}(y, s) + \frac{N\kappa}{\sigma} \int_0^x dy e^{-2ik_0(x-y)} \hat{\phi}(y, s) - e^{-2ik_0x} \frac{N\kappa}{\sigma} \int_0^\sigma dy e^{2ik_0y} \hat{\phi}(y, s). \quad (6.37)$$

Next, we perform a Laplace transformation from the variable x to u and we obtain

$$s \hat{\phi}(u, s) - \frac{1}{u} = -\frac{N\kappa}{u\sigma} \hat{\phi}(u, s) + \frac{N\kappa}{u\sigma + 2ik_0\sigma} \hat{\phi}(u, s) \quad (6.38)$$

$$- \frac{N\kappa}{u\sigma - 2ik_0\sigma} \int_0^\sigma dy e^{2ik_0y} \hat{\phi}(y, s). \quad (6.39)$$

We now take the $k_0\sigma \rightarrow \infty$ limit, for which the last two terms vanish and end up with an algebraic equation for $\hat{\phi}$, for which we directly find the solution

$$\hat{\phi}(u, s) = \frac{\sigma}{su\sigma + N\kappa}. \quad (6.40)$$

The inverse Laplace transformation of this expression back to the variables x and t is given by

$$\phi(x, t) = J_0(2\sqrt{N\kappa xt/\sigma}), \quad (6.41)$$

and we find the solution of the time evolution for the collective bright state

$$\psi(x, t) = e^{ik_0x} J_0(2\sqrt{N\kappa xt/\sigma}). \quad (6.42)$$

From this, we determine the total bright state population

$$P_W(t) = \left| \int_0^\sigma dx J_0(2\sqrt{N\kappa xt/\sigma}) \right|^2 = \left| \frac{J_1(2\sqrt{N\kappa t})}{\sqrt{N\kappa t}} \right|^2, \quad (6.43)$$

which agrees with the exact result for the chiral waveguide (6.17). Similarly, we

6 *Nonexponential decay in multiple-emitter chains*

obtain the total population in the bidirectional waveguide

$$\begin{aligned} P_{\text{total}}(t) &= \int_0^\sigma dx |J_0(2\sqrt{N\kappa xt/\sigma})|^2 \\ &= J_0(2\sqrt{N\kappa t})^2 + J_1(2\sqrt{N\kappa t})^2. \end{aligned} \tag{6.44}$$

Thus, we again have perfect agreement with the exact result (6.33) for the chiral waveguide.



Collective decay of a single superatom

The previous chapters revealed Rydberg superatoms as powerful and versatile systems with applications in creating highly correlated states of light, non-classical states of light, and in deterministic photon subtraction. Our combined theoretical and experimental analysis further demonstrated that our three-level model is a highly accurate and efficient description, which well-captures all the scenarios above. For the final chapter of this thesis, we now want to bring our three-level model to its limits and discuss a setup for which the so far neglected internal dynamics of the superatom become relevant.

Such a situation occurs when we subject a single superatom to a coherent drive for a finite time and then measure the emission rate of the partially excited superatom right after the driving pulse ends. While the three-level model predicts a constant photon emission rate, given by the sum of the spontaneous emission rate κ , the Raman decay Γ and the dephasing rate γ_D , the experimental results demonstrate an explicit dependency of the emission rate on the strength and duration of the previous driving pulse. We argue that this effect originates from the internal exchange interactions of the superatom, similar to the discussion in

the previous chapter. There we saw that the dipole-dipole interaction between atoms significantly alters their superradiant decay in specific regimes. Under this hypothesis, we extend our previous three-level model by introducing an additional fourth level, with a coherent coupling to the superatom's bright state. This four-level model captures the experimental results on a quantitative level. We further motivate the four-level model by a microscopic analysis of the full N -emitter dynamics in a one-dimensional chain.

This chapter's relevance to the broader scientific community lies in the observation that subradiant states cause the alteration in the decay rate. While superradiance has been measured in multiple different systems, like trapped ions [213], molecules [214], artificial atoms [126], or quantum dots [201, 202], the observation of subradiant effects is typically more difficult due to the weak coupling of the subradiant states to the external modes [215]. In fact, the observation of subradiant states in systems containing multiple emitters is a relatively recent achievement [198, 215]. The superatom system, therefore, becomes a promising candidate for this line of research.

This chapter is based on the article [91]. Here, the author of this thesis performed the theoretical analysis of the N -emitter system. The author and co-author N. Stiesdal performed the subsequent comparison to the four-level model in unison. The co-authors N. Stiesdal, H. Busche and J. Kumlin carried out the comparison between the four-level model and the experimental results.

Superatom decay dynamics

7.1

7.1.1 Experimental Setup

The experiments were performed with the setup outlined in section 1.4. We excited a single superatom under varying pulse durations and measured the

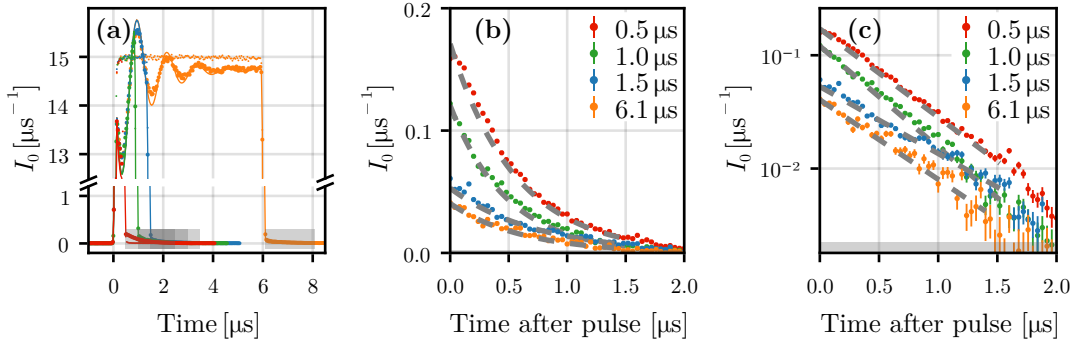


Figure 7.1

(a) Light intensity (in photons/ μs) of a single superatom for different pulse durations. Lines indicate show fits by the four-level model, big dots show measured results and small dots indicate the reference beams, i.e., the intensity in the absence of the superatom. The grey shaded areas indicates the time-regions after the end of the pulses. (b,c) Measured intensity minus the reference intensity after the end of the pulse, as indicated by the grey rectangles in (a). Grey dashed lines shows the $I_0 e^{-\gamma t}$ fit to the data. Error-bars are the standard error of the mean and the grey area at the bottom indicates the data cut-off for the fit.

forward emitted light after the pulse ended (with the control beam remaining on). We then fitted an exponential decay $I_0 e^{-\gamma t}$ to the intensity, to extract the intensity I_0 (in photons/ μs) and the decay rate γ of the superatom. This procedure is outlined in figure 7.1. Figure 7.1 (a) shows the measured intensities for a single superatom and the reference pulses of different durations. Here the grey shaded regions indicate the time intervals after the pulse, which we use for the I_0 and γ extraction. In figure 7.1 we show an enhanced view of these regions, together with the exponential fits to the data. We further verified both by field-ionisation of the Rydberg atom and measuring the ion-statistics, and by determining the two-photon correlation $g^{(2)}(\tau = 0) < 0.1$ that the superatom carried only a single excitation for the presented experimental results.

Particular to our discussion in this chapter, we used different intermediate state

detunings Δ in the experiments. This allows us to tune the spontaneous decay rate κ since the coupling rate κ scales as $1/\Delta^2$, as we showed in section (1.2). By comparing the experimental results to the four-level model, explained below in detail, we then find that the fitted internal coupling rate \varkappa is independent of the external parameters Δ and the Rabi frequency $2\sqrt{\kappa R_{\text{in}}}$. We use this in support of our claim, that the observed pulse-duration dependency of the superatom decay rate γ is due to the internal dynamics of the superatom, which are independent of the external parameters. In the following figures we will directly give the resulting κ instead of the detuning Δ for an easier comparison with previous results.

7.1.2 Superatom decay

Figure 7.2 shows the experimentally determined photon flux (intensity) I_0 and decay rate γ of the superatom immediately after the end of the probe pulse. While we can explain the behaviour of I_0 from the Rabi oscillations of the superatom, the three-level model predicts a constant decay rate $\gamma = \kappa + \Gamma + \gamma_D$. Instead, we find damped oscillations for γ , out of phase with the I_0 oscillations. Furthermore, while γ reaches a steady state for long pulses, the steady state emission rate typically lies below the predicted value from the three-level model for some of the examples.

The frequency of the oscillations in I_0 and γ are linked to the Rabi frequency. To verify this we increased Δ from $2\pi \times 100$ MHz to $2\pi \times 125$ MHz and $2\pi \times 150$ MHz, which leads to a subsequent reduction of κ and Γ and thus to a decreased Rabi frequency, as discussed in the last section. This is displayed in figure 7.2 (a) to (c) for γ and (e) to (g) for I_0 , where we see a slow-down of the oscillations. In order to definitely link the oscillation frequency of γ and I_0 to the Rabi frequency, we further show γ and I_0 at $\kappa = 0.47 \mu\text{s}^{-1}$ and $R_{\text{in}} = 6.7 \mu\text{s}^{-1}$ in figures 7.2 (d) and (h), respectively. This set of parameters yields the same Rabi frequency as $\kappa = 0.21 \mu\text{s}^{-1}$, $R_{\text{in}} = 15 \mu\text{s}^{-1}$, displayed in the panels (c) and

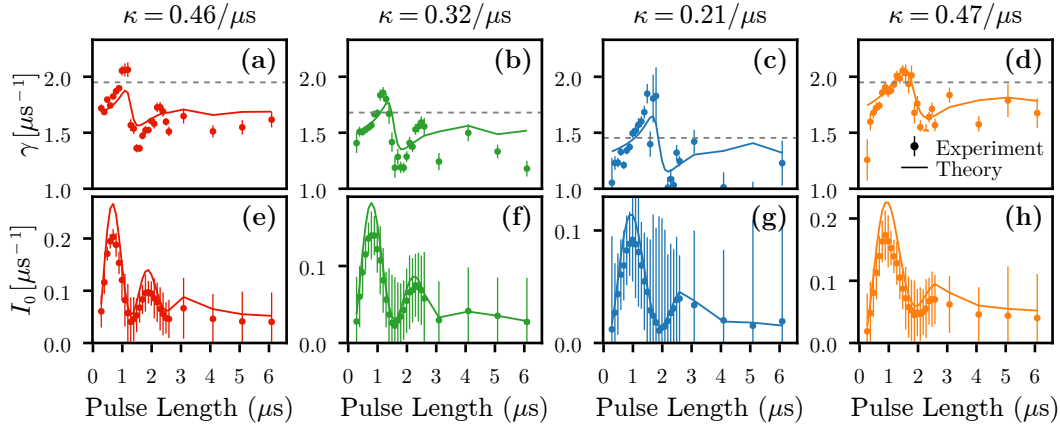


Figure 7.2

Decay rate γ (top row) and photon flux I_0 (bottom row) obtained from fitting $I_0 e^{-\gamma t}$ to intensity signal after the end of the probe pulse. Panels (a, c) are for $\Delta = 2\pi \times 100$ MHz, (b, f) for $\Delta = 2\pi \times 125$ MHz, and (e, g) $\Delta = 2\pi \times 150$ MHz at $R_{\text{in}} = 15 \mu\text{s}^{-1}$, while the two panels (d, h) are at $\Delta = 2\pi \times 100$ MHz and $R_{\text{in}} = 6.7 \mu\text{s}^{-1}$. The dots show the experimental results with error-bars indicating one standard deviation confidence intervals of the fits, while the curves show the theoretical results from the four-level model. Grey dashed lines are the constant decay rate estimated from the three-level superatom model.

(g). I_0 and γ oscillate at the same frequency for these two parameter sets, which underlines the connection between the Rabi frequency $2\sqrt{\kappa R_{\text{in}}}$ and the γ , I_0 oscillations.

In conclusion, our previous three-level model will likely be good enough to capture the behaviour of the photon flux I_0 , as it dominated by the Rabi dynamics of the superatom. However, the three-level model fails to provide a time-dependent decay rate. Since the decay rate oscillates, there must be a mechanism that can both decrease and increase the bright state population. Thus, we are led to the assumption that the bright state has to interact with subradiant states, from which periodic revivals of the bright state population

occur. The simplest model of such an interaction adds an fourth state $|C\rangle$ to our previously used superatom model, with a coherent coupling \varkappa between $|C\rangle$ and $|W\rangle$. We explain this enlarged model in the next section in detail.

7.1.3 Four-level model

We now introduce a fourth level $|C\rangle$ to our superatom model, as depicted in figure 7.3 to the right. $|C\rangle$ possesses a coherent coupling with rate \varkappa to the bright state $|W\rangle$, i.e., we introduce $H_{\text{exc}} = \varkappa(|W\rangle\langle C| + |C\rangle\langle W|)$ to the Hamiltonian. Like every other excited state, we assume that $|C\rangle$ is subject to Raman decay. We further assume that the same incoherent processes that bring $|W\rangle$ into $|D\rangle$ also drive $|C\rangle$ into $|D\rangle$. For simplicity, we model $|C\rangle$'s Raman decay and dephasing with the same

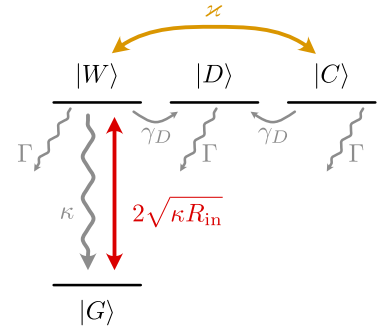


Figure 7.3

Four level model. Double-arrow lines indicate coherent coupling, single-arrow curves stand for incoherent processes.

Table 7.1

Fitted parameters for the three- and four-level model. In the fits we assumed that Γ scales as $\Gamma \propto 1/\Delta^2$. For the three-level model κ and γ_D were free fit parameters. For the four-level model we take κ and Γ from the three-level model, and manually fix $\gamma_D = 0.85 \mu\text{s}^{-1}$ for all datasets, as the fit tended to overestimate this. Thus \varkappa is the only free parameter, showing that the near constant \varkappa was not manually enforced.

R_{in} (μs^{-1})	$\Delta/2\pi$ (μs^{-1})	κ (μs^{-1})	Γ (μs^{-1})	γ_D (3L) (μs^{-1})	γ_D (4L) (μs^{-1})	\varkappa (μs^{-1})
15.0	100	0.46	0.15	1.34	0.85	0.31
15.0	125	0.32	0.10	1.26	0.85	0.32
15.0	150	0.21	0.064	1.18	0.85	0.31
6.7	100	0.47	0.15	1.33	0.85	0.34

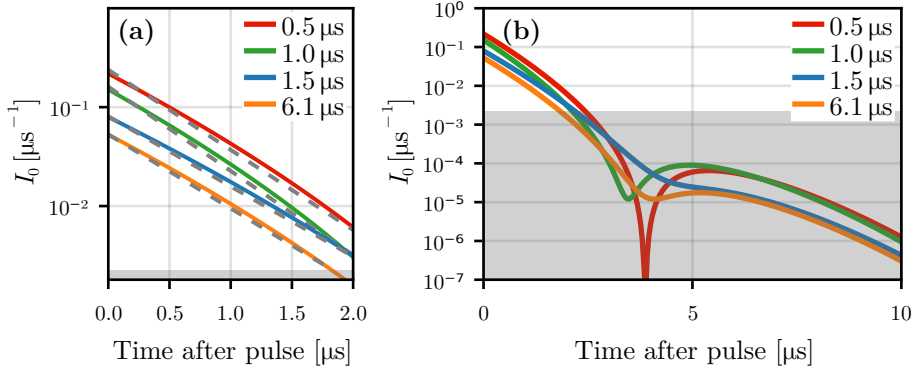


Figure 7.4

Emission signal after the driving pulse ended from the superatom model. (b) shows the same time-range as figure 7.1 (c) and both figures compare well, while (c) shows the same results for longer times. The grey dashed lines indicate fits of $I_0 e^{-\gamma t}$ to the initial time behaviour of the decay. Grey areas indicate the experimental cut-off region, where the mean standard error of I_0 becomes comparable to I_0 . Strong deviations from an exponential behaviour only occur in these regions. The four-level model parameters are the $R_{\text{in}} = 15 \mu\text{s}^{-1}$, $\Delta = 2\pi \times 100 \text{ MHz}$ fits, given in table 7.1.

rates Γ and γ_D as for the bright state. Together with the coherent drive $H_{\text{drive}} = 2\sqrt{\kappa R_{\text{in}}}(|W\rangle\langle G| + |G\rangle\langle W|)$, this results in the master equation

$$\begin{aligned} \partial_t \rho = & -i[H_{\text{exc}} + H_{\text{drive}}, \rho] + \kappa \mathcal{D}_{|G\rangle\langle W|}[\rho] \\ & + \Gamma \sum_{S \in \{W, D, C\}} \mathcal{D}_{|G\rangle\langle S|}[\rho] + \gamma_D \sum_{S \in \{W, C\}} \mathcal{D}_{|D\rangle\langle S|}[\rho]. \end{aligned} \quad (7.1)$$

This model is able to accurately capture the non-constant decay of the superatom, as can be seen in figure 7.2, where we also show the fits of the four-level model to the experimental results. From these fits we obtain a roughly constant coherent coupling rate κ , as we show in table 7.1. This further indicates that the observed effects in the superatom decay are due to internal interactions in the superatom, which are independent of the external parameters κ and R_{in} .

Figure 7.4 shows the intensity after the end of the driving pulse, obtained from the four-level model. Here we find a pulse-duration dependent exponential decay, similar as in the experiment. Panel (a) uses the same time-range as for the experimental results in figure 7.1 (c). However, the four-level model allows us to analyse the emission signal well beyond the experimentally accessible regime, as is shown in figure 7.4 (b). Instead of a purely exponential decay, we see that the emission shows a significant dip, at about $4 \mu\text{s}$, with a subsequent revival of the emission signal. For short pulse durations the dip becomes so strong that it results in almost perfect extinction of the photon emission signal. During the dip the superatom is mostly in the subradiant state and $|W\rangle$ has to be re-populated first, before we can observe further emission.

Lastly, it should be pointed out the results from the four-level model strongly resemble the results for a chiral waveguide of two atoms, as discussed in section 6.2.2. This becomes especially obvious when we compare figure 7.4 (b), showing the decay of the superatom after a coherent pump, to figure 6.2, which displays the decay of the collective bright state of the two chiral atoms. This is no surprise however, as the master equation of the two chiral atoms equals the master equation of the four-level model with $\Gamma = 0 = \gamma_D$ and $\kappa = i\kappa$.

Microscopic motivation for the four-level model

7.2

The four-level model followed from the observation that an oscillating decay rate is only possible due to additional coherent processes and it was further motivated by its ability to reproduce the experimental results with high accuracy. Yet, up to this point the four-level model is a heuristic description of the superatom, without any microscopic origin. In this section we will motivate the four-level model by a thorough comparison with a more complete superatom-model, where

we account for the interactions of all N emitters in the superatom.

More precisely we model the superatom by a chain of N chiral emitters, for which we discussed the decay of the collective bright state in the last chapter. We take this simplified model for the inter-atom interactions, instead of a full three-dimensional treatment of the dipole-dipole interactions, for the following reasons.

Firstly, in our study of the collective bright state decay, we already observed a decay behaviour that critically depends on the interactions of the bright state with the additional subradiant states. Secondly, as the superatom effectively interacts with the light field like a one-dimensional object, we presume that treating its internal structure as one-dimensional as well should be justified for an initial study. Furthermore, a full three-dimensional treatment requires a purely numerical approach, while for the one-dimensional model we are able to derive additional analytic results in support of the heuristic four-level model. Lastly, we treat the atom-atom interactions as being chiral instead of bidirectional. This is motivated by the discussion in the last chapter, which showed that there should be little quantitative difference in both approaches in the considered setup. Yet, the chiral interaction is considerably easier for exact calculations.

7.2.1 Chiral exchange-interaction in the subradiant basis

Given the arguments above, we describe the superatom as a N -emitter chiral waveguide, i.e., it evolves according to the master equation

$$\partial_t \rho = -i[H_{\text{drive}} + H_{\text{exc}}, \rho] + \kappa \mathcal{D}_{|G\rangle\langle W|}[\rho], \quad (7.2)$$

7 Collective decay of a single superatom

where $H_{\text{drive}} = 2\sqrt{\kappa R_{\text{in}}}(|W\rangle\langle G| + |G\rangle\langle W|)$ denotes the coherent drive of the collective bright state $|W\rangle = \sum_j |j\rangle/\sqrt{N}$ and

$$H_{\text{exc}} = \frac{i\kappa}{2N} \sum_{l>j} (|l\rangle\langle j| - |j\rangle\langle l|) \quad (7.3)$$

is the chiral exchange interaction. Here, the states $|G\rangle$ and $|j\rangle$ denote the ground state and the state with the j -th atom excited, respectively. The factor $1/N$ in the exchange interaction emerges since the atoms interact via the single-atom coupling rate κ_0 , while the coupling of the bright state to the light field is enhanced by a factor of N , $\kappa = N\kappa_0$, due to the collective interaction of all atoms with the photons. Additionally, $\mathcal{D}_{|G\rangle\langle W|}$ captures the spontaneous decay of the superradiant bright state. Notice that our formulation in this section differs slightly from the spin operator formulation used in the last chapter. This is because we now impose the Rydberg blockade on our superatom model and thus restrict the basis states to the ground state and the single-excitation states.

We notice that $|W\rangle$ is of singular importance in this model, as both the driving Hamiltonian and the dissipation only act on this single state. Yet, it is easy to see that $|W\rangle$ is not an eigenstate of the exchange Hamiltonian. However, due to the singular role of $|W\rangle$, we should express H_{exc} in a basis that more clearly shows the interaction between $|W\rangle$ with the subradiant states. For this, we define the subradiant states as the normalised states orthogonal to $|W\rangle$, which diagonalise the subradiant sector of H_{exc} .

More formally, we define $P = |W\rangle\langle W| + |G\rangle\langle G|$ the projection onto the bright and ground state manifold, and $Q = 1 - P$ the projection onto the orthogonal complement. We then diagonalise $QH_{\text{exc}}Q$ and define the resulting eigenstates as the subradiant states $|C_j\rangle$. Next, we express the full exchange Hamiltonian in the $\{|W\rangle, |C_j\rangle \mid j = 1 \dots N-1\}$ basis, which reveals the coupling rates between $|W\rangle$ and the individual subradiant states. While this approach sounds impractical at first, we show in the appendix 7.A that all these goals are readily achieved by a

simple Fourier-transform of the natural basis $\{|j\rangle\}$.

We obtain, by this basis change, the partially-diagonalised exchange Hamiltonian

$$H_{\text{exc}} = \sum_{j=1}^{N-1} (\kappa_j |W\rangle\langle C_j| + \kappa_j^* |W\rangle\langle C_j|) + \sum_{j=1}^{N-1} \epsilon_j |C_j\rangle\langle C_j|, \quad (7.4)$$

with the “eigenenergies” $\epsilon_j = \kappa \cot(\pi j/N)/2N$ of the subradiant states and the coupling rates $\kappa_j = -\kappa [i + \cot(\pi j/N)]/2N$ between the bright state and the subradiant states. For $j/N \approx 0$ or $(N-j)/N \approx 0$ we have $|\cot(\pi j/N)/2N| \approx 1/2\pi j$, while for $j \approx N/2$ we find $\cot(\pi j/N) \approx 0$. We can therefore approximatively group the subradiant states into two families. Firstly, the subradiant states with $j/N \approx 0$ or $(N-j)/N \approx 0$ have a finite coupling on the order of κ with $|W\rangle$. Secondly, we have the remaining subradiant states whose coupling to the bright state decays as $1/N$ (assuming fixed κ).

These two groups nicely capture the idea behind the four-level model. The $j \approx N/2$ states act like the effective dark state, as they may be populated by additional dephasing mechanisms, like thermal motion, yet their weak coupling κ_j generally prohibits any re-population of the bright state on the experimental time scales. On the other hand, the $j/N \approx 0$, $(N-j)/N \approx 0$ states are strongly coupled to $|W\rangle$ and therefore are the source of the internal coherent dynamics. It is surprising, that the four-level model only requires one additional subradiant state $|C\rangle$ to describe the observed superatom decay, while the N atom model revealed multiple subradiant states with a significant coupling to $|W\rangle$. We partially assume that this happens, since on the experimental time-scales only a few states can become relevant, which allows us to truncate the Hilbert space to the simple four-level model [74, 216, 217].

7.2.2 Comparison with the four-level model

While our analysis of the chiral waveguide model for the superatom motivates the four-level model, the chiral waveguide model could still result in quite different

7 Collective decay of a single superatom

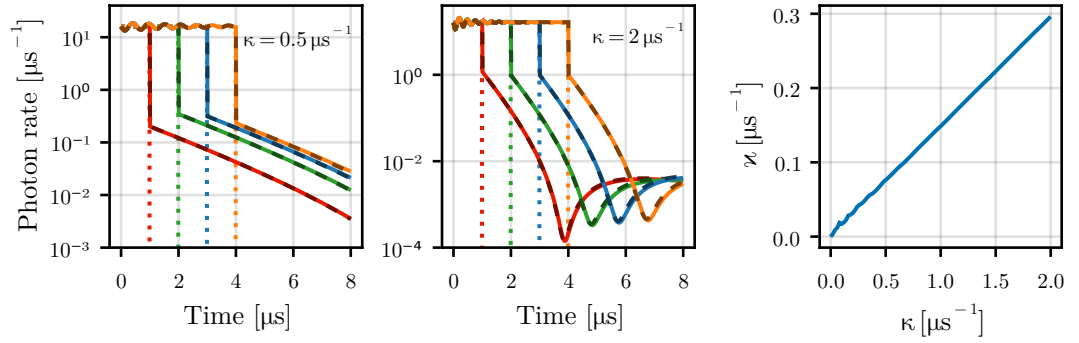


Figure 7.5

(a,b) Rate of emitted photons from the chiral waveguide model at $N = 1000$ atoms (solid lines) and from the four-level model (dashed lines). Dotted lines show the respective driving pulse with peak photon rate $R_{\text{in}} = 16 \mu\text{s}^{-1}$. The left panel display $\kappa = 0.5 \mu\text{s}^{-1}$, close to the experimental values, the right shows $\kappa = 2 \mu\text{s}^{-1}$, which results in \varkappa similar to the experimental fit. The four-level results are obtained by fitting \varkappa , with κ fixed to coupling rate of the chiral waveguide and $\gamma_D = 0 = \Gamma$. (c) Fitted values of \varkappa of a pulse of duration $4 \mu\text{s}$ and rate $R_{\text{in}} = 16 \mu\text{s}^{-1}$.

dynamics, due to the multitude of states. Therefore, we will now directly compare numerical solutions from both models and show that the four-level model is general enough to capture the dynamics of the chiral waveguide model.

Figure 7.5 shows the rate of emitted photons from both models for different κ and pulse duration, with a focus on times after the end of the driving pulse. Curves for the four-level model are obtained by fitting them to the results of the chiral waveguide model, for which we used $N = 1000$ atoms in the simulation. For the fit, we fix κ in the four-level model to the coupling rate of the chiral waveguide and set $\Gamma = 0 = \gamma_D$, as we do not consider any Raman decay in the chiral waveguide model, nor any incoherent processes, that drive the waveguide into the weakly coupled subradiant states. Thus \varkappa is the only free parameter for the fit. Nevertheless, we find excellent agreement between both models with slight deviations only occurring for large times, where the intensity is

already far below the experimentally accessible threshold. Crucially both models show the same drop and revival of the intensity signal after the driving pulse ended, indicating that this not an artefact of the four-level model but an actual, observable effect.

These results further indicate that the four-level model is sufficient to predicting even highly involved internal interaction mechanisms of multiple subradiant states. Yet, we should point out that the actual coherent interactions occurring in an actual superatom are different to the presented chiral waveguide model, so for a full microscopic derivation of the four-level model more work would be necessary. One discrepancy between the chiral waveguide model and the actual experiment is display in figure 7.5, where we see that \varkappa grows linearly with κ , when fitting the four-level model to the chiral waveguide. Opposed to this, we found nearly constant \varkappa for the experimental superatoms. Nevertheless, our main intent in this section was to demonstrate the predictive capabilities of the four-level model. These are clearly verified by our numerical analysis.

Appendix: Exchange Hamiltonian in the subradiant basis

7.A

In this appendix we perform a Fourier transformation of the natural basis states $\{|j\rangle\}$, by which the exchange Hamiltonian becomes diagonal in the subradiant basis. The original intend was to express H_{exc} in a basis, that contains $|W\rangle$ and further does not favour any particular atom state $|j\rangle$. The Fourier transform was a natural choice for this goal as it assigns the same absolute weight $1/\sqrt{N}$ to each state $|j\rangle$. The partial diagonalisation of H_{exc} in this basis was a welcome by-product and was not anticipated at first.

7 Collective decay of a single superatom

We define the new orthonormal basis states

$$|C_k\rangle = \frac{1}{\sqrt{N}} \sum_{j=1}^N e^{2\pi i j k / N} |j\rangle, \quad k \in \{0, \dots, N-1\}, \quad (7.5)$$

with $|C_0\rangle = |W\rangle$. In this basis the exchange Hamiltonian becomes

$$\begin{aligned} H_{\text{exc}} &= \frac{i\kappa}{2N} \sum_{l>j} (|l\rangle\langle j| - |j\rangle\langle l|) \\ &= \frac{i\kappa}{2N^2} \sum_{p,k} |C_k\rangle\langle C_p| \sum_{l>j} (e^{-2\pi i(kl-pj)/N} - e^{-2\pi i(kj-pl)/N}) \\ &= \frac{i\kappa}{2N^2} \sum_{p,k} |C_k\rangle\langle C_p| \sum_{l>j} (e^{-2\pi i(kl-pj)/N} - \overline{p \leftrightarrow k}), \end{aligned} \quad (7.6)$$

where $\overline{p \leftrightarrow k}$ denote the complex conjugate of the left summand with p and k exchanged. The l -summation of the first term results in

$$\sum_{l=j+1}^N e^{-2\pi i k l / N} = \begin{cases} N-j & k=0 \\ \frac{1-e^{2\pi i k j / N}}{1-e^{2\pi i k / N}} & k>0 \end{cases}, \quad (7.7)$$

by the geometric summation formula.

Let us assume $k \neq 0$, for the moment. Due to the self-adjointness of the exchange Hamiltonian it is sufficient to consider $p \geq k$, so we can neglect the special case $p = 0$ for the moment. For $p > k$ it is easy to see that the result vanishes as the individual terms from the geometric sums cancel

$$\sum_{j=1}^{N-1} \frac{1 - e^{2\pi i k j / N}}{1 - e^{2\pi i k / N}} e^{2\pi i p j / N} = 0. \quad (7.8)$$

On the other hand, we obtain for $p = k$

$$\sum_{j=1}^{N-1} \frac{1 - e^{2\pi i k j / N}}{1 - e^{2\pi i k / N}} e^{2\pi i k j / N} = -\frac{N}{1 - e^{2\pi i k / N}}. \quad (7.9)$$

Recall, that in the exchange Hamiltonian (7.6) there is also the $\overline{p \leftrightarrow k}$ term to consider, which here simplifies to just the complex conjugation. Thus the full $|C_k\rangle\langle C_k|$ matrix element becomes

$$\frac{i\kappa}{2N^2} \sum_{l>j} (e^{-2\pi i (kl-pj)/N} - \text{c.c.}) = \frac{\kappa}{2N} \cot(k\pi/N) \equiv \epsilon_k. \quad (7.10)$$

Now let us consider the $k = 0$ case. Here, we should again consider $p = 0 = k$ and $p > k = 0$ separately. For $p = 0$ we obtain the $|W\rangle\langle W|$ matrix element, which is

$$\sum_{j=1}^{N-1} (N - j - \overline{p \leftrightarrow k}) = 0. \quad (7.11)$$

This matrix element trivially vanishes, as $N - j$ is obviously real and independent of p and k . For $p > 0$ we have to determine each summand in (7.6) individually and obtain

$$\begin{aligned} \frac{i\kappa}{2N^2} \sum_{l>j} (e^{2\pi i p j / N} - e^{2\pi i p l / N}) &= \frac{i\kappa}{2N^2} \sum_{j=1}^{N-1} \left((N - j) e^{2\pi i p j / N} - \frac{1 - e^{2\pi i p j / N}}{1 - e^{-2\pi i p / N}} \right) \\ &= -\frac{\kappa}{2N} (i + \cot(p\pi/N)) \equiv \kappa_p. \end{aligned} \quad (7.12)$$

This is the $|W\rangle\langle C_p|$ matrix element.

We have now determined all matrix elements of H_{exc} in the $\{|C_j\rangle\}$ basis. In total, we find that there are only $|W\rangle\langle C_j|$ matrix elements, coupling the bright state to the subradiant states with rate κ_j , and the ‘‘eigenenergies’’ ϵ_j of the $|C_j\rangle$ states. Therefore, H_{exc} has exactly the form of equation (7.4) from the main text.

Ausführliche Zusammenfassung in deutscher Sprache

Kommentar des Autors: Diese Dissertation richtet sich, in erster Linie, an Physiker:innen aus der Quanten-Optik. Diese Zielgruppe ist natürlich wenig überraschend, da diese Dissertation wissenschaftliche Arbeit aus diesem Gebiet zusammenfasst. Im Rahmen dieser Dissertation verlangt die Prüfungsordnung der Universität Stuttgart aber auch eine ausführliche Zusammenfassung in deutscher Sprache, eben jene die Sie im Moment lesen. Das legt die Frage nahe: Welchen Zweck soll diese Zusammenfassung erfüllen?

Auf jeden Fall richtet sie sich nicht an meine erwähnten Kolleg:innen. Das liegt unter anderem daran, dass Englisch die **lingua franca** der Physik und jeder anderen Naturwissenschaft ist. Eine deutschsprachige Zusammenfassung ist nur für eine sehr kleine Teilgruppe meines Forschungsfeldes überhaupt verständlich und für diese finden sich alle hier genannten Ergebnisse bereits in der englischen Zusammenfassung, dem **Abstract**.

Deswegen richtet sich diese Zusammenfassung in erster Linie an alle, die

(noch) nicht wissenschaftlich arbeiten. Das sind Bachelor- und Master-Studierende, aber auch alle Physik-interessierten Personen, die einen Einblick in diese Arbeit erhalten möchten und sich fragen, wofür mein Herz die letzten fünf Jahre geschlagen hat.

Die hier aufgeführten Ergebnisse haben deswegen nicht weniger wissenschaftliche Rigorosität als die Diskussionen in den vorangegangenen Kapiteln, allerdings fällt die Argumentation bildlicher aus, um den Inhalt so zugänglich wie möglich zu gestalten. Des Weiteren sollen an dieser Stelle auch grundlegende physikalische Konzepte erklärt werden, zum Beispiel was Licht aus dem Blick der Quantenphysik ist, die in der eigentlichen Arbeit als bekannt vorausgesetzt wurden.

Diese Dissertation ist in der Quantenoptik angesiedelt. Diese untersucht die Wechselwirkung von quantenmechanischem Licht mit quantenmechanischen Teilchen. Bevor wir an dieser Stelle weiter ins Detail gehen, fangen wir erst einmal damit an, diese beiden Begriffe genauer zu erklären.

Für Quantenphysiker:innen besteht Licht aus Teilchen, sogenannten Photonen. Diese tragen Energie und Impuls mit sich und bewegen sich mit Lichtgeschwindigkeit durch den luftleeren Raum. Das Besondere an der Quantenmechanik ist, dass der Impuls und die Energie nur in festen Portionen aufgenommen oder abgegeben wird. Zum Beispiel erhält ein Atom bei einer Wechselwirkung mit einem Photon die Energie und den Impuls des Photons und das Photon verschwindet, was wir Absorption nennen; das Atom kann nicht „etwas Energie aufnehmen“ während „etwas Photon zurück bleibt“.

Quantenmechanische Teilchen sind, vereinfacht gesagt, alle Teilchen für die diverse quantenmechanische Effekte relevant sind. Zu diesen Effekten gehören beispielsweise die Heisenbergsche Unschärferelation, die die genaue Bestimmung mehrerer Messgrößen unmöglich macht, oder Verschränkung, bei dem

eine Messung an einem Teilchen den Zustand eines zweiten Teilchens direkt beeinflusst. Diese Effekte sind fast immer relevant für die kleinsten Bausteine unseres Universums: einzelne Atome oder kleine Moleküle. Aber auch große und komplexe Systeme wie Halbleiter und andere Metalle benötigen häufig eine quantenmechanische Beschreibung.

Widmen wir uns aber nun den Teilchen, um die es in dieser Arbeit vermehrt geht. Das sind die:

Rydberg-Superatome. Wie bereits angesprochen, wird ein Atom durch die Absorption eines Photons angeregt und die Photonen können nur in festen Paketen mit gegebener Energie absorbiert werden. Diese Energie muss genau zu einem der möglichen Übergänge des Atoms passen, anderenfalls kann das Photon nicht mit dem Atom wechselwirken. Johannes Rydberg [218] gelang es 1888 eine empirische Formel für die Wellenlänge von Photonen zu finden, welche mit Wasserstoffatomen wechselwirken können. Zwar gilt seine Formel nur für Wasserstoff, allerdings gibt es zahlreiche Atome mit ähnlichem Verhalten. Dazu gehören zum Beispiel Rubidium oder Caesium, sobald deren „äußerstes“ (das Valenz-) Elektron stark angeregt ist, also viel Energie besitzt. Aufgrund des wasserstoffähnlichen Verhaltens heißen solche Atome auch Rydberg-Atome.

Führen wir mehrere Rydberg-Atome auf engem Raum zusammen, dann erhalten wir ein Rydberg-Superatom. Für diese ist „das Ganze mehr als nur die Summe seiner Teile“ und sie besitzen Eigenschaften, die sie von den einzelnen Rydberg-Atomen, aus denen sie bestehen, abheben. Gehen wir diese der Reihe nach durch.

Insbesondere treten in Superatomen zwei Effekte auf, die ihnen praktische Eigenschaften verleihen. Der erste Effekt ist die *Rydberg-Blockade* [8], der zweite nennt sich *Superradianz* [53, 54].

Bei der Rydberg-Blockade unterbindet ein angeregtes Rydberg-Atom weitere Anregung in seiner Nähe. Dieser Effekt tritt aufgrund der starken Anregung

der Rydberg-Atome auf.

Klassisch lässt sich dieser Effekt erklären, wenn wir uns das Elektron des angeregten Atoms auf einer Kreisbahn um den Kern des Atoms vorstellen. Je stärker wir das Atom anregen, desto größer wird auch der Umfang dieser Bahn und entsprechend weiter entfernt sich das negative geladene Elektron vom positiven Rest. Befinden sich zwei entgegengesetzte elektrische Ladungen, hier das negativ geladene Elektron und der positive Atomkern, in etwas Abstand zueinander, dann kompensieren sich ihre elektrischen Felder nicht vollständig und ein *Dipol-Feld* entsteht. Das Rydberg-Atom bildet also durch die Anregung ein Dipol, der stärker wird, je weiter das Elektron vom Kern entfernt ist.

In einer quantenmechanischen Betrachtung können wir dem Elektron keinen genauen Ort und damit auch keinen festen Abstand zum Atomkern zuschreiben. Stattdessen besitzt das Elektron eine zufällige Verteilung um den Kern, die von der Anregungsenergie abhängt. Wir brauchen uns deswegen aber keine Sorgen zu machen, der quantenmechanische Beweis folgt der gleichen Logik wie unser klassisches Argument. Die angeregten Rydberg-Atome erzeugen ein Dipol-Feld und dieses Dipol-Feld beeinflusst nun alle weiteren Atome in seiner Nähe.

Dazu erinnern wir uns, dass jedes Atom Energie-Level besitzt, die festlegen mit welchen Photonen die Atome wechselwirken können. Durch das, vom angeregten Rydberg-Atom erzeugte, Dipol-Feld werden aber die Energie-Level der Übergänge verändert und die restlichen, nicht angeregten Atome sind nicht weiter in der Lage, Photonen mit der ursprünglichen Energie zu absorbieren. Die Rydberg-Blockade garantiert also, dass das Superatom immer nur eine Anregung gleichzeitig besitzen kann.

Der zweite Effekt, Superradianz, beschreibt die kollektive Wechselwirkung aller Atome mit den Photonen. Zwar haben wir eben gesehen, dass in einem Superatom immer nur ein einzelnes Atom angeregt sein kann, doch zu dieser ersten Anregung tragen alle Atome gleichermaßen bei.

Typischerweise ist die Chance, dass ein einzelnes Photon mit einem einzelnen

Atom wechselwirkt fast vernachlässigbar. Je mehr Atome sich in dem Superatom befinden, umso größer wird auch die Wahrscheinlichkeit, dass es überhaupt zu einer Wechselwirkung kommt. So können wir uns die Superradianz für die Absorption eines Photons vorstellen. Sobald ein Atom angeregt ist, steigt aber auch die Chance für den Zerfall in gleichem Maße wie die verbesserte Absorptionswahrscheinlichkeit. Denn, quantenmechanisch gesehen, befindet sich das Superatom in einem Zustand, in dem jedes Atom mit gleicher Wahrscheinlichkeit das Photon absorbiert hat, was wir in der Quantenmechanik Überlagerungs- oder Superpositionszustand nennen. Da jedes Atom die Anregung tragen kann, kann jedes Atom zum Zerfall beitragen und deswegen wird der Zerfall umso schneller, je mehr Atome das Superatom besitzt.

Für Superatome im Speziellen ergibt sich zudem, dass das zerfallende Superatom nahezu immer das zuvor absorbierte Photon wieder in seine ursprüngliche Richtung emittiert. Von außen gesehen, sieht die Licht-Superatom-Wechselwirkung also so aus, als fände sie nur auf einer geraden Linie statt. Dieses Phänomen wird auch *Chiralität* genannt; griechisch für "Händigkeit". Denn, das Superatom hat auch für die beiden Optionen der Zerfallsrichtungen auf dieser gedachten Linie eine klare Präferenz: Die Photonen bewegen sich nur nach vorne, Rückstreuung tritt quasi nicht auf.

Da die Licht-Superatom Wechselwirkung die Richtung der Photonen nicht verändert, ergibt sich eine praktische Konsequenz. Erzeugen wir mehrere Superatome in einer Reihe, dann kann ein einzelnes Photon mit mehreren Superatomen hintereinander wechselwirken. Somit kann der Einfluss der Superatome auf das Lichtfeld, zumindest konzeptionell, sehr einfach verstärkt werden.

Zusammengefasst verhalten sich Superatome wie Atome, da sie auch nur ein einziges Photon absorbieren können. Die Wechselwirkung zwischen dem Superatom und den Photonen ist allerdings deutlich stärker, als nur für ein einzelnes Atom. Damit sind Superatome ein interessantes System, um die Wechselwirkung von Licht mit Atomen zu untersuchen. Zudem bewegen sich die

Photonen unter dieser Wechselwirkung immer nur in einer Richtung weiter. Dies erlaubt mehrere Superatome aneinander zu reihen, was zu interessanten kollektiven Effekten zwischen den Superatomen führt.

Die einzelnen Kapitel dieser Dissertation beinhaltet die theoretische Arbeit des Autors zu der Licht-Superatom-Wechselwirkung. Gehen wir die Kapitel an dieser Stelle der Reihe nach durch.

- Das erste Kapitel widmet sich den Rydberg-Superatomen und ihrer Wechselwirkung mit Licht. Hier werden Rydberg-Blockade und Superradianz im Detail eingeführt. Darüber hinaus wird erklärt, wie Superatome über einen Zwei-Photonen-Prozess in ihre hohen Anregungszustände gebracht werden, da sichtbares Licht nicht genug Energie trägt, um diese Zustände mit nur einem Photon zu erreichen.

In der Diskussion der Superradianz werden die bereits besprochenen Effekte hergeleitet: Superatome haben eine verstärkte Wechselwirkung mit dem Licht und die Photonen werden fast perfekt in eine Richtung gestreut. Darüber hinaus zeigen wir, dass eine genaue Beschreibung des Superatoms bereits mit einer handvoll Zuständen möglich ist.

Alle beschriebenen Effekte werden dann in einem effektiven Superatom-Modell zusammengefasst, welches die Ausgangsbasis für fast alle Rechnungen in dieser Dissertation ist. Zuletzt diskutieren wir die experimentelle Realisierung von Superatomen in der Gruppe von Professor S. Hofferberth [90–92]. Während dieser Dissertation gab es eine enge Kollaboration mit der Gruppe von S. Hofferberth und alle hier präsentierten experimentellen Ergebnisse stammen von dieser.

- In Kapitel 2 geht es um die mathematische Beschreibung der Wechselwirkung zwischen Licht und Superatomen. Für diese Dissertation waren die drei folgenden Formalismen besonderes relevant.

Die erste Methode ist der Bethe-Ansatz [93]. Dieser historisch bedeutsame Ansatz erlaubt in vielen eindimensionalen Systemen alle Eigenzustände zu finden; das sind die Zustände, die sich nicht mit der Zeit ändern und durch die jeder andere Zustand vollständig beschrieben werden kann. Mit dem Bethe-Ansatz wurde, zum Beispiel, zum ersten Mal eindimensionaler Anti-Ferromagnetismus exakt beschrieben¹.

Während der Bethe-Ansatz zwar alle Informationen über die Wechselwirkung von Licht mit Superatomen liefert, scheitert die Anwendung allerdings an der Komplexität dieser Methode. In diesem Formalismus können nur eine Handvoll von Photonen berücksichtigt werden und der Bethe-Ansatz kann somit wichtige Lichtzustände, wie etwa das kohärente Licht eines Lasers, nicht beschreiben.

Einige dieser Probleme können wir in dem zweiten Formalismus umgehen. Denn die Photonen können komplett aus der Beschreibung der Dynamik der Superatome eliminiert werden, was zur quantenoptischen Lindblad-Gleichung führt [101, 102]. Diese Eliminierung gelingt nur für kohärentes Laserlicht, aber damit ist dieser Formalismus eine hervorragende komplementäre Beschreibung gegenüber dem Bethe-Ansatz. Zwar tauchen die Photonen in der Lindblad-Gleichung nicht mehr auf, wir besitzen aber weiterhin Informationen über ihre zeitliche Verteilung aus den sogenannten *Input-Output-Relationen* [98]. Diese erlauben uns die Berechnung der Wahrscheinlichkeit, mit der wir mehrere Photonen zu unterschiedlichen Zeiten messen, sobald wir die Lösung der Lindblad-Gleichung kennen.

Dennoch verlieren wir in der Beschreibung mit der Lindblad-Gleichung wichtige Informationen über die Photonen, beispielsweise wie viele Photonen sich in bestimmten Zuständen befinden. In der Gruppe von Professor K. Mølmer wurde dazu eine praktische Lösung entwickelt [106, 107], die der letzte verwendete Formalismus ist. Dazu wird die Lindblad-Gleichung um eine (gedachte) Kavität

¹Etwas genauer: Mit dem Bethe-Ansatz wurde das eindimensionale Heisenberg Modell gelöst, ein wichtiges Modell zur Beschreibung von Magnetismus in Isolatoren.

erweitert, gewissermaßen ein Speichermedium für Photonen. Indem wir die Kopplung der Kavität an die Superatome sorgfältig wählen, können nur Photonen in einem ganz bestimmten Zustand die Kavität betreten. Bestimmen wir im Anschluss die Besetzung der Kavität, dann erhalten wir alle Informationen über die Photonen-Besetzung des entsprechenden Zustands.

Dieser dritte Formalismus ist eine direkte Erweiterung der zuvor diskutierten Lindblad-Gleichung. Damit kann er auf der einen Seite mehr Problemstellungen lösen, entsprechend steigt aber auch der Aufwand. Dieser Kompromiss taucht, genau umgekehrt, auch im Vergleich zu dem Bethe-Ansatz auf. Der Bethe-Ansatz beinhaltet alle Informationen über das Licht und die Superatome, aber ist deutlich am schwersten zu berechnen. In der Anwendung müssen wir immer wieder die Komplexität gegenüber den gesuchten Informationen abwägen.

Mit diesen drei Formalismen sind wir nun gerüstet, um effizient die Licht-Superatom-Wechselwirkung zu beschreiben, Ergebnisse aus Experimenten zu verifizieren und neue Vorhersagen zu treffen.

- Quantenmechanische Systeme ermöglichen Wechselwirkungen, die in klassischen Systemen nicht möglich sind. Photonen-Korrelationen, also die relative Wahrscheinlichkeit, zwei oder mehrere Photonen zu unterschiedlichen Zeiten zu finden, sind eine Signatur der quantenmechanischen Wechselwirkungen in unserem System. Zum Beispiel, erhöht die Anwesenheit von Photonen die Wahrscheinlichkeit, dass ein angeregtes Superatom zerfällt und ein Photon emittiert. Dieser quantenmechanische Prozess heißt stimulierte Emission und resultiert in einer erhöhten Wahrscheinlichkeit, zwei Photonen nahe beieinander zu finden [219]. Kapitel 3 untersucht die Korrelationen der Photonen nach Streuung von kohärentem Licht an einem Superatom.

Die Gruppe von S. Hofferberth [90] hat in ihren Experimenten die Korrelationen zwischen bis zu drei Photonen gemessen. Normalerweise ist die Wechselwirkung von Licht mit freien Atomen zu schwach, als dass die Korrela-

tionen zwischen drei Photonen messbar wäre, aber hier macht die superradiante Wechselwirkung mit dem Superatom diese Effekte sichtbar.

Die gemessenen Korrelationen können hervorragend durch den Bethe-Ansatz erklärt werden. Dieser beinhaltet Zustände, in denen zwei oder mehrere Photonen immer nahe aneinander liegen, weswegen wir die Zustände auch *gebundene Zustände* nennen. Durch die Wechselwirkung mit dem Superatom teilt sich die Wellenfunktion des Lichts gewissermaßen in die freien und gebundenen Zustände auf. Die so erhaltenen Korrelationen passen qualitativ gut zu den experimentellen. Im Experiment treten aber zusätzliche Verlusteffekte auf, die nicht im Bethe-Ansatz berücksichtigt werden können. Diese können aber in die Lindblad-Gleichung eingebaut werden und die Analyse der Lindblad-Gleichung von J. Kumlin² führt zu einer guten Übereinstimmung mit dem Experiment.

- Die Korrelations-Ergebnisse zeigen, dass die Superatome die Photonen stark beeinflussen. In Kapitel 4 untersuchen wir, wie die Superatome die Besetzung einzelner Photonen-Zustände beeinflussen.

Hierfür betrachteten wir zunächst nur ein einzelnes Superatom im Feld eines Lasers. Sobald das Lasersignal abrupt startet, fängt die Superatom-Photonen-Wechselwirkung an, wodurch sich der quantenmechanische Zustand der Photonen ändert. Aus dem Bethe-Ansatz wissen wir, dass grundsätzlich sehr viele unterschiedliche Photonen-Zustände auftreten können, in dem letzten unserer theoretischen Formalismen können wir aber immer nur einen Zustand gleichzeitig untersuchen. Als Anhaltspunkt für die Stärke der Wechselwirkung beschränken wir uns auf Zeitfenster nach dem Start der Wechselwirkung und betrachten wie in diesem, die Photonen den Originalzustand des Lasers besetzen.

Wie sehr die Besetzung nach der Wechselwirkung von der ursprünglichen abweicht, hängt besonders von dem gewählten Zeitfenster ab. Betrachten wir zum Beispiel das Licht, welches zum Zeitpunkt der stärksten Anregung des

²Co-Autor des Artikel [90].

Superatoms erzeugt wird, dann hat das Superatom eine hohe Wahrscheinlichkeit, zu zerfallen und ein einzelnes Photon zu emittieren. Ein einzelnes Photon ist hochgradig „nicht-klassisch“, das Licht des Lasers hingegen kann vollkommen klassisch verstanden werden. Zu einem Zeitpunkt starker Superatomanregungen ist die Abweichung vom Ursprungszustand des Lasers folglich am größten.

Sobald allerdings mehrere Superatome beteiligt sind, muss auch die Wechselwirkung zwischen den Superatomen berücksichtigt werden, da sie auch die emittierten Photonen beeinflusst. Es ist sogar möglich, dass ein zweites Superatom genau die Wirkung des vorherigen Superatoms auflöst und sich der Zustand der Photonen nicht ändert. Es wird also nicht einfach ein Photon pro Superatom emittiert. Dieser Effekt kann mithilfe des Bethe-Ansatzes erklärt werden und basiert mathematisch auf einem doppelten Vorzeichenwechsel nach der Wechselwirkung an dem zweiten Superatom.

Dieser Effekt tritt nur lange nach dem Start des Lasers auf. Zu früheren Zeitpunkten ist die paarweise Auslöschung nicht perfekt, aber beeinflusst dennoch maßgebend die Wirkung der Superatome auf die Photonen.

In vielen Fällen sind also die Photonen, welche unter der Wechselwirkung eines Lasers mit Superatomen erzeugt werden, anders verteilt als das ursprüngliche Laserlicht. Die neue Verteilung macht das Licht unter anderem interessant für potenzielle Anwendungen.

Ein konkretes Beispiel ist eine Längen-Messung in einem Interferometer, beispielsweise wie bei der Detektion von Gravitationswellen [220]. Die Quantenmechanik schränkt allerdings ein, wie genau diese Länge bestimmt werden kann [116]. Bestimmte Lichtzustände können die Sensitivität der Messung maßgeblich erhöhen [174]. Für das, von dem Superatom erzeugte, Licht finden wir eine Verbesserung in der Messgenauigkeit von fast 20 % im Vergleich zu reinem Laserlicht.

- Wie alle größeren physikalischen Systeme unterliegen auch Superatome Stör-

effekten. Ein explizites Beispiel ist, dass Superradianz, also die starke Licht-Superatom-Koppelung, nur für einen perfekt abgestimmten Superatom-Zustand auftritt. Störungen an dieser fein justierten Konfiguration, zum Beispiel durch thermische Bewegung der einzelnen Atome, treiben das Superatom in Zustände, die nicht länger superradiant sind und somit keine Photonen emittieren können, zumindest nicht innerhalb der Dauer eines Experiments. Das Superatom bleibt dabei aber natürlich angeregt und die Rydberg-Blockade verhindert eine erneute Photon-Absorption. Effektiv kann das Superatom also nicht länger mit Photonen wechselwirken und wird durchsichtig. Gleichzeitig bleibt das Photon, welches das ursprüngliche Superatom angeregt hat, in diesem gespeichert.

Dieser Effekt kann also genutzt werden, um kontrolliert Photonen aus dem einfallenden Licht zu entfernen. Kapitel 5 zeigt, dass Superatome genau solche *Photonen-Subtrahierer* sind und die Gruppe von S. Hofferberth hat so einen 3-Photonen Subtrahierer realisiert [92]. Hier verwenden wir unser Superatom-Modell, um die perfekten Bedingungen für Photonen-Subtraktion vorher zu sagen.

Die Erwartung legt nahe, dass mit zunehmender Stärke der oben genannten Störeffekte auch die Chance für die Subtraktion eines Photons zunimmt. Allerdings unterbinden diese auch die Wechselwirkung zwischen den Superatomen und dem Licht. Deshalb ist ein Kompromiss nötig, zwischen der Geschwindigkeit, mit dem das Superatom angeregt wird, und der Geschwindigkeit, mit der das angeregte Superatom in einen gestörten Zustand übergeht. Konkret ergibt sich, dass diese beiden konkurrierenden Effekte von der Stärke des einfallenden Lasers abhängen, und, sollten weitere Photonen-Verlust-Effekte vorhanden sein, auch von der Dauer des Experimentes.

- Die Superradianz eines Superatoms ist ein kollektiver Effekt aller Atome in dem Superatom. Genau so können aber auch kollektive Effekte auftreten, sobald **mehrere** Superatome miteinander wechselwirken. Ein Beispiel hierfür war die

Auslöschung der Lichtwechselwirkung für Superatom-Paare, wie in Kapitel 4 besprochen.

Im sechsten Kapitel dieser Dissertation wird ein weiterer dieser Wechselwirkungseffekte genauer untersucht. Dazu betrachten wir den Zerfall einer Superatom-Kette, angeregt in ihrem superradianten Zustand.

Wie zunächst erwartet, findet auch hier der Zerfall zunächst superradiant statt, wird also umso schneller, je mehr Superatome sich in der Kette befinden. Allerdings bremst die Wechselwirkung zwischen den Superatomen den Zerfall nahezu sofort aus und die Kette geht in *subradiante* Zustände über, also Zustände die nicht oder kaum zerfallen.

Besteht die Kette nur aus wenigen Atomen, wird der Zerfall irgendwann von dem unkorrelierten Zerfall der einzelnen Superatome dominiert. Für hinreichend viele Atome ändert die Superatom-Wechselwirkung aber sogar dieses Zerfallsverhalten. Dabei geht die Superatom-Kette in einen Zustand, bei dem die verbleibende Anregung äußerst langsam zerfällt und sich auch im zeitlichen Ablauf von dem Zerfall eines einzelnen Superatoms unterscheidet, ein sogenannter *algebraischer* Zerfall.

Wir haben zuvor besprochen, dass Superatome chiral sind, dass sie also Photonen nur in eine Richtung streuen. Interessanterweise tritt das exakt gleiche Zerfallsverhalten auch auf, falls wir auf Chiralität verzichten und wir Streuung in beide Richtungen erlauben; zumindest sofern die Superatome über ein hinreichend großes Gebiet verteilt sind. Damit gehen diese Zerfalls-Ergebnisse über Superatom-Systeme hinaus und finden auch Anwendung in anderen eindimensionalen Systemen.

- Alle bis zu diesem Punkt präsentierten Ergebnisse basieren auf dem Superatom-Modell, welches das Superatom nur durch seinen superradianten Zustand und etwaige Störeffekte beschreibt. Effektiv wurde die interne Wechselwirkung der einzelnen Atome im Superatom ignoriert. Mit dieser Beschreibung wurden

sämtliche experimentelle Ergebnisse in den vorangegangenen Kapiteln präzise reproduziert und erklärt.

In Kapitel 6 haben wir aber ein Beispiele gesehen, in der die Wechselwirkung zwischen Superatomen dominiert. Diese ähnelt in vielerlei Hinsicht der internen Wechselwirkung der Atome in einem Superatom. Entsprechend gibt es Regime, in welchen diese interne Wechselwirkung ebenfalls relevant wird. Das letzte Kapitel behandelt genau so einen Fall.

Dazu präparierte die Gruppe von S. Hofferberth zunächst ein einzelnes Superatom in einem angeregten Zustand, indem sie das Superatom für eine feste Zeit mit einem Laser bestrahlen [91]. Der anschließende Zerfall des Superatoms hängt von der vorherigen Laser-Dauer und -Intensität ab, was im wechselwirkungsfreien Superatom-Modell nicht möglich ist.

Erweitern wir unser Superatom-Modell um einen weiteren wechselwirkenden Zustand, reicht dies bereits aus, um wieder Ergebnisse im Einklang mit dem Experiment zu liefern. Das allein bedeutet aber noch nicht, dass unser neues Modell die korrekte Physik beschreibt, also die Wechselwirkung im Superatom die Ursache hinter dem modifizierten Zerfallsverhalten ist. Besser ist es, wenn wir eine Motivation des neuen Modells in einer fundamentaleren Beschreibung des Superatoms finden.

Wir erinnern uns, dass die Wechselwirkung im Superatom große Ähnlichkeiten mit der Wechselwirkung in einer Superatom-Kette hat. Betrachten wir die subradianten Zustände der Kette, also Zustände, die nicht direkt ein Photon emittieren können, dann sehen wir, dass diese mit unterschiedlicher Stärke an den superradianten Zustand gekoppelt sind. Die schwach gekoppelten Zustände entsprechen den langlebigen Störungszuständen der Superatome, die für die kontrollierte Photon-Absorption in Kapitel 5 relevant waren. Alle weiteren, stark gekoppelten Zustände, lassen sich, wie der Vergleich mit dem vereinfachten Modell zeigt, in einem einzigen Zustand zusammenfassen.

Zusammenfassend lässt sich sagen: Superatome sind vielseitige Systeme, die stark wechselwirkend an das Lichtfeld gekoppelt sind. Sie ermöglichen es, Photonen in stark korrelierte Zustände zu bringen oder ihnen auch nicht-klassische Eigenschaften zu vermitteln. Mit Superatomen können wir effektiv Photonen aus dem einlaufenden Lichtfeld entfernen. Gleichzeitig liefern sie Systeme mit hochgradig interessanten Wechselwirkungen, bei denen sich zum Beispiel die Wirkung zweier Superatome auf das Lichtfeld gegenseitig aufheben können oder in denen mehrere Superatome in schwach zerfallende, subradiante Zustände übergehen.

Acknowledgements

*“Now, on your diplomas, there will be only one name on it
and this is yours. But I hope that that doesn’t confuse
and that you think that you maybe made it this far by yourself.
No you didn’t. It took a lot of help.”*

Arnold Schwarzenegger, graduation speech at the University of Houston, 2017

This thesis was not created in a vacuum¹. Instead, my research was coined by the influence of so many people. I want to dedicate this section to everyone who accompanied me during the last years and helped me in my journey through my PhD studies.

First and foremost, I thank Hans Peter Büchler from all of my heart. Over the last few years, I learned how invaluable your feedback is. Our hour-long discussions were probably one of the most crucial learning experiences during my PhD studies. Thanks for all the freedom we PhD students enjoy in your group, and for all the opportunities you provided me to present my work at conferences and in front of my colleagues abroad.

I further thank Jörg Main for examining this thesis and for the significant part you had in my undergraduate studies. And I thank Tilman Pfau for presiding over the examining board and his work as the coordinator of the GiRyd priority

¹which strangely contradicts one of the most important assumption we typically make.

Acknowledgements

program. The yearly status workshops were one of my annual highlights during the last year.

But what is a PhD without your fellow students and colleagues? I thank everyone from the third institute of theoretical physics. You greatly influenced my PhD thesis due to our lunchtime banter and our annual volleyball tournaments² And you always had open ears for my nasty physics questions; the insight you get by hopping from office to office and hearing multiple ideas is priceless. Much gratitude goes to Jan Kumlin, Nicolai Lang, Sebastian Weber, and Tobias Ilg. You four accompanied me since the start of my PhD, and I learned so much from every one of you.

I am further very grateful to have worked with Oliver Nagel. I am pretty sure this thesis, and probably everything else at the ITP3, would have failed horribly without you. Your work keeps the institute running³.

Every piece of work in this thesis emerged as the product of one of the most fantastic collaborations I could have wished for. Thanks for the many great years of shared research and ideas to everyone in the group of Sebastian Hofferberth. I especially want to thank Hannes Busche and Nina Stiesdal. Hannes, you are an incredible experienced person and I learned a lot from you about scientific writing. Nina, I remember phases in the first COVID lockdown when I had more contact with you from the home office than with anyone from the Stuttgart⁴. Needless to say, I enjoyed every single minute of our work.

Another great physicist, who made me enjoy my work, is Klaus Mølmer. I was wholly inspired by what a great teacher and scientist you are. Thank you for all your valuable input and for joining up in my final project of this PhD thesis.

A big part of my PhD studies was my teaching duties. Teaching consists, in large amounts, about two things: thinking about what confused you once and getting asked nasty questions that should have confused you. I learned a lot

²I am really sad, that this thesis made me miss the final one.

³And you protect every PhD student from the monster that is the administrative madness.

⁴In my mind you are an honorary member of the ITP3.

from my teaching activities, and I want to thank every student who was a part of that, especially my bachelor's and master's students.

As dissertations tend to do, this one also had its tiring days. Yet, I never had to confront the struggles of a PhD life alone. Instead, I always had my friends and family by my side, to whom I owe a lot of gratitude for their support.

Firstly, I want to thank all my borderline-insane CrossFit friends and all the athletes of CrossFit Four Horsemen. Our sport kept me sane when work or other things tried their best to do the opposite. Some of the greatest moments I remember from the last years happened in the gym, whether it was coaching someone their first Pull Up, being there for stupidly heavy PRs or cheering your vocal cords out in crazy competitions. I think there is nothing else that can compare to our community spirit, and I am so happy to belong to this weird group that does Burpees for fun. Thanks to all of you for suffering alongside me, and a big, sweaty hug to my fellow coaches and competitors.

A lot of gratitude goes to my best friend and “brother from another mother“, Oliver Ramoli. You are one of the kindest and humblest person I know. Thanks that I could always rely on you.

Lastly, my most important thanks go to my family. I am pretty sure that I have the best brother, the most supportive parents and the kindest grandparents. I could always count on your kindness and help. Never would I have been able to do this without you. Thank you for everything you ever gave me.

Bibliography

- [1] H. J. Metcalf, “Highly excited atoms”, *Nature* **284**, 127 (1980).
- [2] T. F. Gallagher, “Rydberg atoms”, *Reports on Progress in Physics* **51**, 143 (1988).
- [3] N. Šibalić and C. S. Adams, “Rydberg physics”, 2399-2891, IOP Publishing (2018).
- [4] K. Singer, M. Reetz-Lamour, T. Amthor, L. G. Marcassa, and M. Weidemüller, “Suppression of excitation and spectral broadening induced by interactions in a cold gas of rydberg atoms”, *Phys. Rev. Lett.* **93**, 163001 (2004).
- [5] E. Brion, A. Mouritzen, and K. Mølmer, “Conditional dynamics induced by new configurations for rydberg dipole-dipole interactions”, *Physical Review A* **76**, 022334 (2007).
- [6] T. F. Gallagher and P. Pillet, “Dipole–dipole interactions of rydberg atoms”, *Advances in Atomic, Molecular, and Optical Physics* **56**, 161 (2008).
- [7] R. Löw, H. Weimer, J. Nipper, J. B. Balewski, B. Butscher, H. P. Büchler, and T. Pfau, “An experimental and theoretical guide to strongly interact-

Bibliography

- ing rydberg gases”, *Journal of Physics B: Atomic, Molecular and Optical Physics* **45**, 113001 (2012).
- [8] M. D. Lukin, M. Fleischhauer, R. Cote, L. M. Duan, D. Jaksch, J. I. Cirac, and P. Zoller, “Dipole blockade and quantum information processing in mesoscopic atomic ensembles”, *Phys. Rev. Lett.* **87**, 037901 (2001).
- [9] D. Tong, S. M. Farooqi, J. Stanojevic, S. Krishnan, Y. P. Zhang, R. Côté, E. E. Eyler, and P. L. Gould, “Local blockade of rydberg excitation in an ultracold gas”, *Phys. Rev. Lett.* **93**, 063001 (2004).
- [10] T. Vogt, M. Viteau, J. Zhao, A. Chotia, D. Comparat, and P. Pillet, “Dipole blockade at förster resonances in high resolution laser excitation of rydberg states of cesium atoms”, *Phys. Rev. Lett.* **97**, 083003 (2006).
- [11] R. Heidemann, U. Raitzsch, V. Bendkowsky, B. Butscher, R. Löw, L. Santos, and T. Pfau, “Evidence for coherent collective rydberg excitation in the strong blockade regime”, *Phys. Rev. Lett.* **99**, 163601 (2007).
- [12] E. Urban, T. A. Johnson, T. Henage, L. Isenhower, D. D. Yavuz, T. G. Walker, and M. Saffman, “Observation of rydberg blockade between two atoms”, *Nature Physics* **5**, 110 (2009).
- [13] A. V. Gorshkov, J. Otterbach, M. Fleischhauer, T. Pohl, and M. D. Lukin, “Photon-photon interactions via rydberg blockade”, *Phys. Rev. Lett.* **107**, 133602 (2011).
- [14] Y. O. Dudin and A. Kuzmich, “Strongly interacting rydberg excitations of a cold atomic gas”, *Science* **336**, 887 (2012).
- [15] J. Lim, H.-g. Lee, and J. Ahn, “Review of cold rydberg atoms and their applications”, *Journal of the Korean Physical Society* **63**, 867 (2013).

- [16] C. S. Adams, J. D. Pritchard, and J. P. Shaffer, “Rydberg atom quantum technologies”, *Journal of Physics B: Atomic, Molecular and Optical Physics* **53**, 012002 (2019).
- [17] M. Saffman, T. G. Walker, and K. Mølmer, “Quantum information with rydberg atoms”, *Reviews of modern physics* **82**, 2313 (2010).
- [18] D. Jaksch, J. I. Cirac, P. Zoller, S. L. Rolston, R. Côté, and M. D. Lukin, “Fast quantum gates for neutral atoms”, *Physical Review Letters* **85**, 2208 (2000).
- [19] M. Saffman and T. Walker, “Analysis of a quantum logic device based on dipole-dipole interactions of optically trapped rydberg atoms”, *Physical Review A* **72**, 022347 (2005).
- [20] H. Levine et al., “Parallel implementation of high-fidelity multiqubit gates with neutral atoms”, *Phys. Rev. Lett.* **123**, 170503 (2019).
- [21] D. Tiarks, S. Schmidt-Eberle, T. Stolz, G. Rempe, and S. Dürr, “A photon–photon quantum gate based on rydberg interactions”, *Nature Physics* **15**, 124 (2019).
- [22] G. K. Brennen, C. M. Caves, P. S. Jessen, and I. H. Deutsch, “Quantum logic gates in optical lattices”, *Physical Review Letters* **82**, 1060 (1999).
- [23] I. H. Deutsch, G. K. Brennen, and P. S. Jessen, “Quantum computing with neutral atoms in an optical lattice”, *Fortschritte der Physik: Progress of Physics* **48**, 925 (2000).
- [24] H. Weimer, M. Müller, I. Lesanovsky, P. Zoller, and H. P. Büchler, “A rydberg quantum simulator”, *Nature Physics* **6**, 382 (2010).
- [25] P. Schauß et al., “Observation of spatially ordered structures in a two-dimensional rydberg gas”, *Nature* **491**, 87 (2012).

Bibliography

- [26] H. Labuhn, D. Barredo, S. Ravets, S. de Léséleuc, T. Macrì, T. Lahaye, and A. Browaeys, “Tunable two-dimensional arrays of single rydberg atoms for realizing quantum ising models”, *Nature* **534**, 667 (2016).
- [27] H. Bernien et al., “Probing many-body dynamics on a 51-atom quantum simulator”, *Nature* **551**, 579 (2017).
- [28] H. Kim, Y. Park, K. Kim, H.-S. Sim, and J. Ahn, “Detailed balance of thermalization dynamics in rydberg-atom quantum simulators”, *Phys. Rev. Lett.* **120**, 180502 (2018).
- [29] S. de Léséleuc, V. Lienhard, P. Scholl, D. Barredo, S. Weber, N. Lang, H. P. Büchler, T. Lahaye, and A. Browaeys, “Observation of a symmetry-protected topological phase of interacting bosons with rydberg atoms”, *Science* **365**, 775 (2019).
- [30] V. Lienhard et al., “Realization of a density-dependent peierls phase in a synthetic, spin-orbit coupled rydberg system”, *Physical Review X* **10**, 021031 (2020).
- [31] S. Ebadi et al., “Quantum phases of matter on a 256-atom programmable quantum simulator”, *Nature* **595**, 227 (2021).
- [32] G. Semeghini et al., “Probing topological spin liquids on a programmable quantum simulator”, *Science* **374**, 1242 (2021).
- [33] A. Mokhberi, M. Hennrich, and F. Schmidt-Kaler, “Chapter four - trapped rydberg ions: A new platform for quantum information processing”, in L. F. Dimauuro, H. Perrin, and S. F. Yelin, eds., “Advances In Atomic, Molecular, and Optical Physics”, volume 69 of *Advances In Atomic, Molecular, and Optical Physics*, pp. 233–306, Academic Press (2020).

- [34] L. Henriët, L. Beguin, A. Signoles, T. Lahaye, A. Browaeys, G.-O. Raymond, and C. Jurczak, “Quantum computing with neutral atoms”, *Quantum* **4**, 327 (2020).
- [35] Y. Alexeev et al., “Quantum computer systems for scientific discovery”, *PRX Quantum* **2**, 017001 (2021).
- [36] S. R. Cohen and J. D. Thompson, “Quantum computing with circular rydberg atoms”, *PRX Quantum* **2**, 030322 (2021).
- [37] M. Morgado and S. Whitlock, “Quantum simulation and computing with rydberg-interacting qubits”, *AVS Quantum Science* **3**, 023501 (2021).
- [38] The Paris based start-up **Pasqal** currently develops a Rydberg atom based quantum processor. Related articles are listed on their website.
- [39] Several, by Germany’s federal ministry of education and research sponsored, projects currently develop Rydberg atom based quantum processors and related technologies. These include Munich based MUNIQC, Darmstadt based DaNaQTP. Kaiserslautern and Hamburg based Rymax One and the Stuttgart based projects CiiRQus and GiRydDemo.
- [40] M. Fleischhauer, A. Imamoglu, and J. P. Marangos, “Electromagnetically induced transparency: Optics in coherent media”, *Rev. Mod. Phys.* **77**, 633 (2005).
- [41] J. D. Pritchard, “Cooperative optical non-linearity in a blockaded rydberg ensemble”, Springer Science & Business Media (2012).
- [42] J. D. Pritchard, K. J. Weatherill, and C. S. Adams, “Nonlinear optics using cold rydberg atoms”, pp. 301–350, World Scientific (2013).

Bibliography

- [43] O. Firstenberg, C. S. Adams, and S. Hofferberth, “Nonlinear quantum optics mediated by rydberg interactions”, *Journal of Physics B: Atomic, Molecular and Optical Physics* **49**, 152003 (2016).
- [44] O. Firstenberg, T. Peyronel, Q.-Y. Liang, A. V. Gorshkov, M. D. Lukin, and V. Vuletić, “Attractive photons in a quantum nonlinear medium”, *Nature* **502**, 71 (2013).
- [45] M. Moreno-Cardoner, D. Goncalves, and D. E. Chang, “Quantum nonlinear optics based on two-dimensional rydberg atom arrays”, *Phys. Rev. Lett.* **127**, 263602 (2021).
- [46] L. Zhang, V. Walther, K. Mølmer, and T. Pohl, “Photon-photon interactions in rydberg-atom arrays”, *Quantum* **6**, 674 (2022).
- [47] K. Srakaew, P. Weckesser, S. Hollerith, D. Wei, D. Adler, I. Bloch, and J. Zeiher, “A subwavelength atomic array switched by a single rydberg atom”, *arXiv preprint arXiv:2207.09383* (2022).
- [48] R. J. Bettles, S. A. Gardiner, and C. S. Adams, “Enhanced optical cross section via collective coupling of atomic dipoles in a 2d array”, *Phys. Rev. Lett.* **116**, 103602 (2016).
- [49] R. Bekenstein, I. Pikovski, H. Pichler, E. Shahmoon, S. F. Yelin, and M. D. Lukin, “Quantum metasurfaces with atom arrays”, *Nature Physics* **16**, 676 (2020).
- [50] T. Secker, R. Gerritsma, A. W. Glaetzle, and A. Negretti, “Controlled long-range interactions between rydberg atoms and ions”, *Phys. Rev. A* **94**, 013420 (2016).
- [51] N. V. Ewald, T. Feldker, H. Hirzler, H. A. FÜRst, and R. Gerritsma, “Observation of interactions between trapped ions and ultracold rydberg atoms”, *Phys. Rev. Lett.* **122**, 253401 (2019).

- [52] A. Pifrader, O. Allard, G. Auböck, C. Callegari, W. E. Ernst, R. Huber, and F. Ancilotto, “One- and two-photon spectroscopy of highly excited states of alkali-metal atoms on helium nanodroplets”, *The Journal of Chemical Physics* **133**, 164502 (2010).
- [53] R. H. Dicke, “Coherence in spontaneous radiation processes”, *Physical Review* **93**, 99 (1954).
- [54] M. Gross and S. Haroche, “Superradiance: An essay on the theory of collective spontaneous emission”, *Physics Reports* **93**, 301 (1982).
- [55] I. E. Mazets and G. Kurizki, “Multiatom cooperative emission following single-photon absorption: Dicke-state dynamics”, *Journal of Physics B: Atomic, Molecular and Optical Physics* **40**, F105 (2007).
- [56] J. T. Manassah, “The single photon superradiance from the eigenmode analysis”, *Laser physics* **19**, 2102 (2009).
- [57] J. D. Pritchard, D. Maxwell, A. Gauguet, K. J. Weatherill, M. P. A. Jones, and C. S. Adams, “Cooperative atom-light interaction in a blockaded rydberg ensemble”, *Phys. Rev. Lett.* **105**, 193603 (2010).
- [58] Y. O. Dudin, L. Li, F. Bariani, and A. Kuzmich, “Observation of coherent many-body rabi oscillations”, *Nature Physics* **8**, 790 (2012).
- [59] J. Zeiher, P. Schauß, S. Hild, T. Macrì, I. Bloch, and C. Gross, “Microscopic characterization of scalable coherent rydberg superatoms”, *Phys. Rev. X* **5**, 031015 (2015).
- [60] J. Vaneecloo, S. Garcia, and A. Ourjoumtsev, “Cavity QED with a Rydberg superatom: coherent control, single-shot detection, and conditional optical phase flips”, in E. Diamanti, S. Ducci, N. Treps, and S. Whitlock, eds., “Quantum Technologies 2022”, volume 12133, p. 121330A, International Society for Optics and Photonics, SPIE (2022).

Bibliography

- [61] M. Fleischhauer and M. D. Lukin, “Dark-state polaritons in electromagnetically induced transparency”, *Phys. Rev. Lett.* **84**, 5094 (2000).
- [62] P. Grangier, “Room for just one photon”, *Science* **336**, 812 (2012).
- [63] P. Bienias, S. Choi, O. Firstenberg, M. F. Maghrebi, M. Gullans, M. D. Lukin, A. V. Gorshkov, and H. P. Büchler, “Scattering resonances and bound states for strongly interacting rydberg polaritons”, *Phys. Rev. A* **90**, 053804 (2014).
- [64] F. Ripka, Y.-H. Chen, R. Löw, and T. Pfau, “Rydberg polaritons in a thermal vapor”, *Phys. Rev. A* **93**, 053429 (2016).
- [65] J. Otterbach, M. Moos, D. Muth, and M. Fleischhauer, “Wigner crystallization of single photons in cold rydberg ensembles”, *Phys. Rev. Lett.* **111**, 113001 (2013).
- [66] K. Jachymski, P. Bienias, and H. P. Büchler, “Three-body interaction of rydberg slow-light polaritons”, *Phys. Rev. Lett.* **117**, 053601 (2016).
- [67] T. Peyronel, O. Firstenberg, Q.-Y. Liang, S. Hofferberth, A. V. Gorshkov, T. Pohl, M. D. Lukin, and V. Vuletić, “Quantum nonlinear optics with single photons enabled by strongly interacting atoms”, *Nature* **488**, 57 (2012).
- [68] J. Moore, C. Stanitski, and P. Jurs, “Principles of chemistry: the molecular science”, Cengage Learning (2009).
- [69] R. H. Lehmborg, “Radiation from an n -atom system. i. general formalism”, *Phys. Rev. A* **2**, 883 (1970).
- [70] R. H. Lehmborg, “Radiation from an n -atom system. ii. spontaneous emission from a pair of atoms”, *Phys. Rev. A* **2**, 889 (1970).

- [71] M. O. Scully, “Collective lamb shift in single photon dicke superradiance”, *Phys. Rev. Lett.* **102**, 143601 (2009).
- [72] A. A. Svidzinsky, J.-T. Chang, and M. O. Scully, “Cooperative spontaneous emission of n atoms: Many-body eigenstates, the effect of virtual lamb shift processes, and analogy with radiation of n classical oscillators”, *Phys. Rev. A* **81**, 053821 (2010).
- [73] W. E. Lamb and R. C. Retherford, “Fine structure of the hydrogen atom by a microwave method”, *Phys. Rev.* **72**, 241 (1947).
- [74] G. McCauley, B. Cruikshank, D. I. Bondar, and K. Jacobs, “Accurate lindblad-form master equation for weakly damped quantum systems across all regimes”, *npj Quantum Information* **6**, 1 (2020).
- [75] M. O. Scully, E. S. Fry, C. H. R. Ooi, and K. Wódkiewicz, “Directed spontaneous emission from an extended ensemble of n atoms: Timing is everything”, *Phys. Rev. Lett.* **96**, 010501 (2006).
- [76] M. O. Scully, “Correlated spontaneous emission on the volga”, *Laser Physics* **17**, 635 (2007).
- [77] A. A. Svidzinsky, J.-T. Chang, and M. O. Scully, “Dynamical evolution of correlated spontaneous emission of a single photon from a uniformly excited cloud of n atoms”, *Phys. Rev. Lett.* **100**, 160504 (2008).
- [78] R. Friedberg and J. T. Manassah, “Effects of including the counterrotating term and virtual photons on the eigenfunctions and eigenvalues of a scalar photon collective emission theory”, *Physics Letters A* **372**, 2514 (2008).
- [79] R. Friedberg and J. Manassah, “The eikonal-sveas analytic closed forms for single-photon superradiance”, *Laser Physics* **20**, 250 (2010).

Bibliography

- [80] R. Friedberg and J. T. Manassah, “Initial cooperative decay rate and cooperative lamb shift of resonant atoms in an infinite cylindrical geometry”, *Physical Review A* **84**, 023839 (2011).
- [81] R. Friedberg and J. T. Manassah, “Non-dicke decay in a small spherical sample with radially varying density”, *Physical Review A* **85**, 013834 (2012).
- [82] J. T. Manassah, “Emission from a slab of resonant two-level atoms induced by a delta-pulse excitation”, *Laser Physics* **22**, 559 (2012).
- [83] G. S. Agarwal, “Quantum statistical theories of spontaneous emission and their relation to other approaches”, pp. 1–128, Springer Berlin Heidelberg, Berlin, Heidelberg (1974).
- [84] M. Arcari et al., “Near-unity coupling efficiency of a quantum emitter to a photonic crystal waveguide”, *Phys. Rev. Lett.* **113**, 093603 (2014).
- [85] R. Mitsch, C. Sayrin, B. Albrecht, P. Schneeweiss, and A. Rauschenbeutel, “Quantum state-controlled directional spontaneous emission of photons into a nanophotonic waveguide”, *Nature Communications* **5**, 5713 (2014).
- [86] I. Söllner et al., “Deterministic photon–emitter coupling in chiral photonic circuits”, *Nature nanotechnology* **10**, 775 (2015).
- [87] M. Scheucher, A. Hilico, E. Will, J. Volz, and A. Rauschenbeutel, “Quantum optical circulator controlled by a single chirally coupled atom”, *Science* **354**, 1577 (2016).
- [88] P. Solano, P. Barberis-Blostein, F. K. Fatemi, L. A. Orozco, and S. L. Rolston, “Super-radiance reveals infinite-range dipole interactions through a nanofiber”, *Nature Communications* **8**, 1857 (2017).

- [89] S. Xiao et al., “Position-dependent chiral coupling between single quantum dots and cross waveguides”, *Applied Physics Letters* **118**, 091106 (2021).
- [90] N. Stiesdal, J. Kumlin, K. Kleinbeck, P. Lunt, C. Braun, A. Paris-Mandoki, C. Tresp, H. P. Büchler, and S. Hofferberth, “Observation of three-body correlations for photons coupled to a Rydberg superatom”, *Physical Review Letters* **121**, 103601 (2018).
- [91] N. Stiesdal, H. Busche, J. Kumlin, K. Kleinbeck, H. P. Büchler, and S. Hofferberth, “Observation of collective decay dynamics of a single rydberg superatom”, *Phys. Rev. Research* **2**, 043339 (2020).
- [92] N. Stiesdal, H. Busche, K. Kleinbeck, J. Kumlin, M. G. Hansen, H. P. Büchler, and S. Hofferberth, “Controlled multi-photon subtraction with cascaded rydberg superatoms as single-photon absorbers”, *Nature Communications* **12**, 4328 (2021).
- [93] H. Bethe, “Zur theorie der metalle”, *Zeitschrift für Physik* **71**, 205 (1931).
- [94] V. Yudson, “Dynamics of integrable quantum systems”, *Zh. Eksp. Teor. Fiz* **88**, 1757 (1985).
- [95] V. Yudson, “Dynamics of the integrable one-dimensional system “photons+ two-level atoms””, *Physics Letters A* **129**, 17 (1988).
- [96] V. Yudson and P. Reineker, “Multiphoton scattering in a one-dimensional waveguide with resonant atoms”, *Physical Review A* **78**, 052713 (2008).
- [97] P. Lodahl, S. Mahmoodian, S. Stobbe, A. Rauschenbeutel, P. Schneeweiss, J. Volz, H. Pichler, and P. Zoller, “Chiral quantum optics”, *Nature* **541**, 473 (2017).

Bibliography

- [98] C. W. Gardiner and M. J. Collett, “Input and output in damped quantum systems: Quantum stochastic differential equations and the master equation”, *Phys. Rev. A* **31**, 3761 (1985).
- [99] H.-P. Breuer and F. Petruccione, “The theory of open quantum systems”, Oxford University Press on Demand (2002).
- [100] T. Caneva, M. T. Manzoni, T. Shi, J. S. Douglas, J. I. Cirac, and D. E. Chang, “Quantum dynamics of propagating photons with strong interactions: a generalized input–output formalism”, *New Journal of Physics* **17**, 113001 (2015).
- [101] T. Shi, D. E. Chang, and J. I. Cirac, “Multiphoton-scattering theory and generalized master equations”, *Physical Review A* **92**, 053834 (2015).
- [102] H. Pichler, T. Ramos, A. J. Daley, and P. Zoller, “Quantum optics of chiral spin networks”, *Physical Review A* **91**, 042116 (2015).
- [103] A. Paris-Mandoki, C. Braun, J. Kumlin, C. Tresp, I. Mirgorodskiy, F. Christaller, H. P. Büchler, and S. Hofferberth, “Free-space quantum electrodynamics with a single rydberg superatom”, *Phys. Rev. X* **7**, 041010 (2017).
- [104] J. Gough and M. R. James, “The series product and its application to quantum feedforward and feedback networks”, *IEEE Transactions on Automatic Control* **54**, 2530 (2009).
- [105] J. Combes, J. Kerckhoff, and M. Sarovar, “The slh framework for modeling quantum input-output networks”, *Advances in Physics: X* **2**, 784 (2017).
- [106] A. H. Küllerich and K. Mølmer, “Input-output theory with quantum pulses”, *Physical review letters* **123**, 123604 (2019).

- [107] A. H. Kiilerich and K. Mølmer, “Quantum interactions with pulses of radiation”, *Physical Review A* **102**, 023717 (2020).
- [108] K. Kleinbeck, “Quantum light interaction with superatoms”, Master’s thesis, University of Stuttgart (2017).
- [109] K. Mølmer, Y. Castin, and J. Dalibard, “Monte carlo wave-function method in quantum optics”, *J. Opt. Soc. Am. B* **10**, 524 (1993).
- [110] H. Carmichael, “An open systems approach to quantum optics: lectures presented at the université libre de bruxelles, october 28 to november 4, 1991”, volume 18, Springer Science & Business Media (2009).
- [111] C. Gardiner and P. Zoller, “Quantum noise: a handbook of markovian and non-markovian quantum stochastic methods with applications to quantum optics”, volume 56, Springer Science & Business Media (2004).
- [112] S. Swain, “Master equation derivation of quantum regression theorem”, *Journal of Physics A: Mathematical and General* **14**, 2577 (1981).
- [113] H. Gibbs, “Optical bistability: controlling light with light”, Elsevier (2012).
- [114] D. E. Chang, V. Vuletić, and M. D. Lukin, “Quantum nonlinear optics—photon by photon”, *Nature Photonics* **8**, 685 (2014).
- [115] H. J. Kimble, “The quantum internet”, *Nature* **453**, 1023 (2008).
- [116] H. M. Wiseman and G. J. Milburn, “Quantum measurement and control”, Cambridge university press (2009).
- [117] V. Giovannetti, S. Lloyd, and L. Maccone, “Advances in quantum metrology”, *Nature photonics* **5**, 222 (2011).

Bibliography

- [118] J.-P. Li et al., “Heralded nondestructive quantum entangling gate with single-photon sources”, *Phys. Rev. Lett.* **126**, 140501 (2021).
- [119] T. Stolz, H. Hegels, M. Winter, B. Röhr, Y.-F. Hsiao, L. Husel, G. Rempe, and S. Dürr, “Quantum-logic gate between two optical photons with an average efficiency above 40%”, *Phys. Rev. X* **12**, 021035 (2022).
- [120] E. Knill, R. Laflamme, and G. J. Milburn, “A scheme for efficient quantum computation with linear optics”, *nature* **409**, 46 (2001).
- [121] C. Śliwa and K. Banaszek, “Conditional preparation of maximal polarization entanglement”, *Physical Review A* **67**, 030101 (2003).
- [122] J. M. Raimond, M. Brune, and S. Haroche, “Manipulating quantum entanglement with atoms and photons in a cavity”, *Rev. Mod. Phys.* **73**, 565 (2001).
- [123] I. Shomroni, S. Rosenblum, Y. Lovsky, O. Bechler, G. Guendelman, and B. Dayan, “All-optical routing of single photons by a one-atom switch controlled by a single photon”, *Science* **345**, 903 (2014).
- [124] T. G. Tiecke, J. D. Thompson, N. P. de Leon, L. R. Liu, V. Vuletić, and M. D. Lukin, “Nanophotonic quantum phase switch with a single atom”, *Nature* **508**, 241 (2014).
- [125] B. Hacker, S. Welte, G. Rempe, and S. Ritter, “A photon–photon quantum gate based on a single atom in an optical resonator”, *Nature* **536**, 193 (2016).
- [126] A. F. van Loo, A. Fedorov, K. Lalumière, B. C. Sanders, A. Blais, and A. Wallraff, “Photon-mediated interactions between distant artificial atoms”, *Science* **342**, 1494 (2013).

- [127] S. Faez, P. Türschmann, H. R. Haakh, S. Götzinger, and V. Sandoghdar, “Coherent interaction of light and single molecules in a dielectric nanoguide”, *Phys. Rev. Lett.* **113**, 213601 (2014).
- [128] J. Petersen, J. Volz, and A. Rauschenbeutel, “Chiral nanophotonic waveguide interface based on spin-orbit interaction of light”, *Science* **346**, 67 (2014).
- [129] A. Goban, C.-L. Hung, J. D. Hood, S.-P. Yu, J. A. Muniz, O. Painter, and H. J. Kimble, “Superradiance for atoms trapped along a photonic crystal waveguide”, *Phys. Rev. Lett.* **115**, 063601 (2015).
- [130] P. Lodahl, S. Mahmoodian, and S. Stobbe, “Interfacing single photons and single quantum dots with photonic nanostructures”, *Rev. Mod. Phys.* **87**, 347 (2015).
- [131] A. Sipahigil et al., “An integrated diamond nanophotonics platform for quantum-optical networks”, *Science* **354**, 847 (2016).
- [132] Q.-Y. Liang et al., “Observation of three-photon bound states in a quantum nonlinear medium”, *Science* **359**, 783 (2018).
- [133] I. Afek, O. Ambar, and Y. Silberberg, “High-noon states by mixing quantum and classical light”, *Science* **328**, 879 (2010).
- [134] J. Abadie et al., “A gravitational wave observatory operating beyond the quantum shot-noise limit”, *Nature Physics* **7**, 962 (2011).
- [135] J. Aasi et al., “Enhanced sensitivity of the ligo gravitational wave detector by using squeezed states of light”, *Nature Photonics* **7**, 613 (2013).
- [136] G. Weihs, T. Jennewein, C. Simon, H. Weinfurter, and A. Zeilinger, “Violation of bell’s inequality under strict einstein locality conditions”, *Physical Review Letters* **81**, 5039 (1998).

Bibliography

- [137] B. G. Christensen et al., “Detection-loophole-free test of quantum nonlocality, and applications”, *Phys. Rev. Lett.* **111**, 130406 (2013).
- [138] M. Giustina et al., “Significant-loophole-free test of bell’s theorem with entangled photons”, *Physical review letters* **115**, 250401 (2015).
- [139] D. Stucki, N. Gisin, O. Guinnard, G. Ribordy, and H. Zbinden, “Quantum key distribution over 67 km with a plug&play system”, *New Journal of Physics* **4**, 41 (2002).
- [140] C. Gobby, a. Yuan, and A. Shields, “Quantum key distribution over 122 km of standard telecom fiber”, *Applied Physics Letters* **84**, 3762 (2004).
- [141] M. Peev et al., “The SECOQC quantum key distribution network in vienna”, *New Journal of Physics* **11**, 075001 (2009).
- [142] T. Lunghi, J. Kaniewski, F. Bussieres, R. Houlmann, M. Tomamichel, A. Kent, N. Gisin, S. Wehner, and H. Zbinden, “Experimental bit commitment based on quantum communication and special relativity”, *Physical review letters* **111**, 180504 (2013).
- [143] M. Bentivegna et al., “Experimental scattershot boson sampling”, *Science Advances* **1**, e1400255 (2015).
- [144] M. V. Larsen, X. Guo, C. R. Breum, J. S. Neergaard-Nielsen, and U. L. Andersen, “Deterministic generation of a two-dimensional cluster state”, *Science* **366**, 369 (2019).
- [145] D. F. Walls, “Squeezed states of light”, *Nature* **306**, 141 (1983).
- [146] C. Kim and P. Kumar, “Quadrature-squeezed light detection using a self-generated matched local oscillator”, *Physical review letters* **73**, 1605 (1994).

- [147] M. e. Tse et al., “Quantum-enhanced advanced LIGO detectors in the era of gravitational-wave astronomy”, *Physical Review Letters* **123**, 231107 (2019).
- [148] H. Lee, P. Kok, and J. P. Dowling, “A quantum rosetta stone for interferometry”, *Journal of Modern Optics* **49**, 2325 (2002).
- [149] M. Hua, M.-J. Tao, and F.-G. Deng, “Efficient generation of noon states on two microwave-photon resonators”, *Chinese science bulletin* **59**, 2829 (2014).
- [150] A. Zavatta, S. Viciani, and M. Bellini, “Quantum-to-Classical Transition with Single-Photon-Added Coherent States of Light”, *Science* **306**, 660 (2004).
- [151] H. Kim, H. S. Park, and S.-K. Choi, “Three-photon n00n states generated by photon subtraction from double photon pairs”, *Opt. Express* **17**, 19720 (2009).
- [152] U. Titulaer and R. Glauber, “Correlation functions for coherent fields”, *Physical Review* **140**, B676 (1965).
- [153] M. Hillery, “Classical pure states are coherent states”, *Physics Letters A* **111**, 409 (1985).
- [154] A. Bach and U. Lüxmann-Ellinghaus, “The simplex structure of the classical states of the quantum harmonic oscillator”, *Communications in Mathematical Physics* **107**, 553 (1986).
- [155] M. Hillery, “Nonclassical distance in quantum optics”, *Physical Review A* **35**, 725 (1987).
- [156] M. O. Scully and M. S. Zubairy, “Quantum optics”, (1999).

Bibliography

- [157] J. K. Asbóth, J. Calsamiglia, and H. Ritsch, “Computable measure of nonclassicality for light”, *Physical review letters* **94**, 173602 (2005).
- [158] E. Sudarshan, “Equivalence of semiclassical and quantum mechanical descriptions of statistical light beams”, *Physical Review Letters* **10**, 277 (1963).
- [159] R. J. Glauber, “Coherent and incoherent states of the radiation field”, *Physical Review* **131**, 2766 (1963).
- [160] W. P. Schleich, “Quantum optics in phase space”, John Wiley & Sons (2011).
- [161] D. Gottesman, “The heisenberg representation of quantum computers”, *arXiv preprint quant-ph/9807006* (1998).
- [162] S. Aaronson and D. Gottesman, “Improved simulation of stabilizer circuits”, *Phys. Rev. A* **70**, 052328 (2004).
- [163] A. Mari and J. Eisert, “Positive wigner functions render classical simulation of quantum computation efficient”, *Phys. Rev. Lett.* **109**, 230503 (2012).
- [164] S. Krämer, D. Plankensteiner, L. Ostermann, and H. Ritsch, “QuantumOptics.jl: A Julia framework for simulating open quantum systems”, *Computer Physics Communications* **227**, 109 (2018).
- [165] S. Mahmoodian, G. Calajó, D. E. Chang, K. Hammerer, and A. S. Sørensen, “Dynamics of many-body photon bound states in chiral waveguide qed”, *Phys. Rev. X* **10**, 031011 (2020).
- [166] M. Stobińska, G. Alber, and G. Leuchs, “Perfect excitation of a matter qubit by a single photon in free space”, *EPL (Europhysics Letters)* **86**, 14007 (2009).

- [167] Y. Wang, J. c. v. Minář, L. Sheridan, and V. Scarani, “Efficient excitation of a two-level atom by a single photon in a propagating mode”, *Phys. Rev. A* **83**, 063842 (2011).
- [168] S. Zhang, C. Liu, S. Zhou, C.-S. Chuu, M. M. Loy, and S. Du, “Coherent control of single-photon absorption and reemission in a two-level atomic ensemble”, *Physical review letters* **109**, 263601 (2012).
- [169] G. M. D’Ariano, M. G. Paris, and M. F. Sacchi, “Quantum tomography”, *Advances in Imaging and Electron Physics* **128**, 206 (2003).
- [170] C. W. Helstrom, “Quantum detection and estimation theory”, *Journal of Statistical Physics* **1**, 231 (1969).
- [171] A. S. Holevo, “Probabilistic and statistical aspects of quantum theory”, volume 1, Springer Science & Business Media (2011).
- [172] S. L. Braunstein and C. M. Caves, “Statistical distance and the geometry of quantum states”, *Physical Review Letters* **72**, 3439 (1994).
- [173] S. L. Braunstein, C. M. Caves, and G. J. Milburn, “Generalized uncertainty relations: theory, examples, and lorentz invariance”, *annals of physics* **247**, 135 (1996).
- [174] R. Demkowicz-Dobrzański, M. Jarzyna, and J. Kołodyński, “Quantum limits in optical interferometry”, *Progress in Optics* **60**, 345 (2015).
- [175] M. Holland and K. Burnett, “Interferometric detection of optical phase shifts at the heisenberg limit”, *Physical review letters* **71**, 1355 (1993).
- [176] L. Pezzé and A. Smerzi, “Entanglement, nonlinear dynamics, and the heisenberg limit”, *Physical review letters* **102**, 100401 (2009).

Bibliography

- [177] R. Demkowicz-Dobrzański, J. Kołodyński, and M. Guţă, “The elusive heisenberg limit in quantum-enhanced metrology”, *Nature communications* **3**, 1 (2012).
- [178] C. M. Caves, “Quantum-mechanical radiation-pressure fluctuations in an interferometer”, *Physical Review Letters* **45**, 75 (1980).
- [179] C. M. Caves, “Quantum-mechanical noise in an interferometer”, *Physical Review D* **23**, 1693 (1981).
- [180] M. D. Lang and C. M. Caves, “Optimal quantum-enhanced interferometry using a laser power source”, *Physical review letters* **111**, 173601 (2013).
- [181] K. Goda et al., “A quantum-enhanced prototype gravitational-wave detector”, *Nature Physics* **4**, 472 (2008).
- [182] S. S. Y. Chua, M. S. Stefszky, C. M. Mow-Lowry, B. C. Buchler, S. Dwyer, D. A. Shaddock, P. K. Lam, and D. E. McClelland, “Backscatter tolerant squeezed light source for advanced gravitational-wave detectors”, *Opt. Lett.* **36**, 4680 (2011).
- [183] P. Jordan, “Der zusammenhang der symmetrischen und linearen gruppen und das mehrkörperproblem”, *Zeitschrift für Physik* **94**, 531 (1935).
- [184] J. Schwinger, “On angular momentum us atomic energy commission”, (1952).
- [185] I. N. Bronshtein and K. A. Semendyayev, “Handbook of mathematics”, Springer Science & Business Media (2013).
- [186] J. Fiurášek, R. García-Patrón, and N. J. Cerf, “Conditional generation of arbitrary single-mode quantum states of light by repeated photon subtractions”, *Phys. Rev. A* **72**, 033822 (2005).

- [187] J. S. Neergaard-Nielsen, B. M. Nielsen, C. Hettich, K. Mølmer, and E. S. Polzik, “Generation of a superposition of odd photon number states for quantum information networks”, *Phys. Rev. Lett.* **97**, 083604 (2006).
- [188] H. Takahashi, J. S. Neergaard-Nielsen, M. Takeuchi, M. Takeoka, K. Hayasaka, A. Furusawa, and M. Sasaki, “Entanglement distillation from gaussian input states”, *Nature Photonics* **4**, 178 (2010).
- [189] D. Braun, P. Jian, O. Pinel, and N. Treps, “Precision measurements with photon-subtracted or photon-added gaussian states”, *Phys. Rev. A* **90**, 013821 (2014).
- [190] V. Parigi, A. Zavatta, M. Kim, and M. Bellini, “Probing quantum commutation rules by addition and subtraction of single photons to/from a light field”, *Science* **317**, 1890 (2007).
- [191] J. Calsamiglia, S. M. Barnett, N. Lütkenhaus, and K.-A. Suominen, “Removal of a single photon by adaptive absorption”, *Phys. Rev. A* **64**, 043814 (2001).
- [192] T. Gerrits et al., “Generation of optical coherent-state superpositions by number-resolved photon subtraction from the squeezed vacuum”, *Phys. Rev. A* **82**, 031802 (2010).
- [193] A. Ourjoumtsev, R. Tualle-Brouri, J. Laurat, and P. Grangier, “Generating optical schrödinger kittens for quantum information processing”, *Science* **312**, 83 (2006).
- [194] L. Susskind and J. Glogower, “Quantum mechanical phase and time operator”, *Physics Physique Fizika* **1**, 49 (1964).
- [195] R. Friedberg and J. T. Manassah, “Analytic expressions for the initial cooperative decay rate and cooperative lamb shift for a spherical sample of two-level atoms”, *Physics Letters A* **374**, 1648 (2010).

Bibliography

- [196] R. Röhlsberger, K. Schlage, B. Sahoo, S. Couet, and R. Ruffer, “Collective lamb shift in single-photon superradiance”, *Science* **328**, 1248 (2010).
- [197] J. Pellegrino, R. Bourgain, S. Jennewein, Y. R. P. Sortais, A. Browaeys, S. D. Jenkins, and J. Ruostekoski, “Observation of suppression of light scattering induced by dipole-dipole interactions in a cold-atom ensemble”, *Phys. Rev. Lett.* **113**, 133602 (2014).
- [198] W. Guerin, M. O. Araújo, and R. Kaiser, “Subradiance in a large cloud of cold atoms”, *Phys. Rev. Lett.* **116**, 083601 (2016).
- [199] S. Jennewein, M. Besbes, N. J. Schilder, S. D. Jenkins, C. Sauvan, J. Ruostekoski, J.-J. Greffet, Y. R. P. Sortais, and A. Browaeys, “Coherent scattering of near-resonant light by a dense microscopic cold atomic cloud”, *Phys. Rev. Lett.* **116**, 233601 (2016).
- [200] A. Glicenstein, G. Ferioli, N. Šibalić, L. Brossard, I. Ferrier-Barbut, and A. Browaeys, “Collective shift in resonant light scattering by a one-dimensional atomic chain”, *Phys. Rev. Lett.* **124**, 253602 (2020).
- [201] M. Scheibner, T. Schmidt, L. Worschech, A. Forchel, G. Bacher, T. Passow, and D. Hommel, “Superradiance of quantum dots”, *Nature Physics* **3**, 106 (2007).
- [202] P. Tighineanu, R. S. Daveau, T. B. Lehmann, H. E. Beere, D. A. Ritchie, P. Lodahl, and S. Stobbe, “Single-photon superradiance from a quantum dot”, *Phys. Rev. Lett.* **116**, 163604 (2016).
- [203] R. Friedberg, S. Hartmann, and J. Manassah, “Frequency shifts in emission and absorption by resonant systems of two-level atoms”, *Physics Reports* **7**, 101 (1973).

- [204] M. O. Scully and A. A. Svidzinsky, “The lamb shift yesterday, today, and tomorrow”, *Science* **328**, 1239 (2010).
- [205] J. Keaveney, A. Sargsyan, U. Krohn, I. G. Hughes, D. Sarkisyan, and C. S. Adams, “Cooperative lamb shift in an atomic vapor layer of nanometer thickness”, *Phys. Rev. Lett.* **108**, 173601 (2012).
- [206] Z. Meir, O. Schwartz, E. Shahmoon, D. Oron, and R. Ozeri, “Cooperative lamb shift in a mesoscopic atomic array”, *Phys. Rev. Lett.* **113**, 193002 (2014).
- [207] S. J. Roof, K. J. Kemp, M. D. Havey, and I. M. Sokolov, “Observation of single-photon superradiance and the cooperative lamb shift in an extended sample of cold atoms”, *Phys. Rev. Lett.* **117**, 073003 (2016).
- [208] R. Friedberg and J. T. Manassah, “Time-dependent directionality of cooperative emission after short pulse excitation”, *Optics communications* **281**, 4391 (2008).
- [209] R. J. Bettles, T. Ilieva, H. Busche, P. Huillery, S. W. Ball, N. L. Spong, and C. S. Adams, “Collective mode interferences in light–matter interactions”, *arXiv preprint arXiv:1808.08415* (2018).
- [210] J. Kumlin, K. Kleinbeck, N. Stiesdal, H. Busche, S. Hofferberth, and H. P. Büchler, “Nonexponential decay of a collective excitation in an atomic ensemble coupled to a one-dimensional waveguide”, *Physical Review A* **102**, 063703 (2020).
- [211] “*NIST Digital Library of Mathematical Functions*”, <http://dlmf.nist.gov/18.11.ii>, Release 1.1.6 of 2022-06-30, f. W. J. Olver, A. B. Olde Daalhuis, D. W. Lozier, B. I. Schneider, R. F. Boisvert, C. W. Clark, B. R. Miller, B. V. Saunders, H. S. Cohl, and M. A. McClain, eds.

Bibliography

- [212] “*NIST Digital Library of Mathematical Functions*”, <http://dlmf.nist.gov/10.17.i>, Release 1.1.6 of 2022-06-30, f. W. J. Olver, A. B. Olde Daalhuis, D. W. Lozier, B. I. Schneider, R. F. Boisvert, C. W. Clark, B. R. Miller, B. V. Saunders, H. S. Cohl, and M. A. McClain, eds.
- [213] R. G. DeVoe and R. G. Brewer, “Observation of superradiant and sub-radiant spontaneous emission of two trapped ions”, *Phys. Rev. Lett.* **76**, 2049 (1996).
- [214] C. Hettich, C. Schmitt, J. Zitzmann, S. Kühn, I. Gerhardt, and V. Sandoghdar, “Nanometer resolution and coherent optical dipole coupling of two individual molecules”, *Science* **298**, 385 (2002).
- [215] S. D. Jenkins, J. Ruostekoski, N. Papanikolaou, S. Savo, and N. I. Zheludev, “Many-body subradiant excitations in metamaterial arrays: Experiment and theory”, *Phys. Rev. Lett.* **119**, 053901 (2017).
- [216] T. Katayama *et al.*, “Subspace methods for system identification”, volume 1, Springer (2005).
- [217] P. Van Overschee and B. De Moor, “Subspace identification for linear systems: Theory—implementation—applications”, Springer Science & Business Media (2012).
- [218] J. Rydberg, “On the structure of the line-spectra of the chemical elements”, *The London, Edinburgh, and Dublin philosophical magazine and journal of science* **29**, 331 (1890).
- [219] D. B. Scarl and S. R. Smith, “Time correlations in stimulated emission”, *Phys. Rev. A* **10**, 709 (1974).

- [220] B. P. Abbott et al., “Observation of gravitational waves from a binary black hole merger”, *Phys. Rev. Lett.* **116**, 061102 (2016).

**Schriftliche Bestätigung der eigenständig erbrachten Leistung gemäß
§6 Absatz 2 der Promotionsordnung der Universität Stuttgart**

Die eingereichte Dissertation zum Thema „Photon correlations and collective phenomena with Rydberg superatoms“ stellt meine eigenständig erbrachte Leistung dar.

Ich habe ausschließlich die angegebenen Quellen und Hilfsmittel benutzt. Wörtlich oder inhaltlich aus anderen Werken übernommene Angaben habe ich als solche kenntlich gemacht.

Die Richtigkeit der hier getätigten Angaben bestätige ich und versichere, nach bestem Wissen die Wahrheit erklärt zu haben.

Stuttgart, den 26. August 2022.

Kevin Kleinbeck

Erklärung zur Übereinstimmung der digitalen Version mit der vorgelegten Printversion der Dissertation

Hiermit erkläre ich, Kleinbeck, Kevin, geboren am 27.07.1992, dass das von mir eingereichte pdf-Dokument zur Dissertation mit dem Thema „Photon correlations and collective phenomena with Rydberg superatoms“ in Inhalt und Wortlaut der ebenfalls eingereichten Printversion meiner Dissertationsschrift entspricht.

Stuttgart, den 26. August 2022.

Kevin Kleinbeck